



UNIVERSITÀ DEGLI STUDI DI PADOVA
LEIBNIZ UNIVERSITÄT HANNOVER

DIPARTIMENTO DI INGEGNERIA INDUSTRIALE
CORSO DI LAUREA MAGISTRALE IN INGEGNERIA DELL'ENERGIA ELETTRICA

**Numerical and practical
investigation of an inhomogeneous
heating process for forging parts**

Author:

Marco Baldan [1067317]

Supervisors:

Pf. Dr.-Ing. Egbert Baake

Ing. Michele Forzan

Dipl.-Ing. Thomas Steinberg

Academic Year 2015/2016

To whoever believes in me

Introduction

In this thesis an innovative induction heating process for forging is analysed. The main idea is to heat up a carbon steel cylinder in a non-homogeneous way, in order to obtain two “hot” zones, which reach a temperature round 1050 – 1100 °C, with in the middle a “cold” zone with a temperature that varies between 800 and 950 °C. The main advantage is the possibility to simplify the pre-forming process and to save energy. The first part of the analysis was carried out using a FEM software, with which several models were designed with different inductor’s geometry. In simulations the dependency of permeability on magnetic field is kept into account. In order to guarantee more simplicity, the inductor is unique. More turns are used in the “hot” areas instead than in the “cold” one. In order to obtain a uniform thermal profile, in each zone, the pitch between turns at the edges is reduced and at the centre increased. The aim is to guarantee a more constant magnetic field trend. There are other topics source of investigation. First inductor ends’ influence, in terms of magnetic flux density, inside the coil. Results show that the module variation is higher than 2% only at the edges, when connections and coil are very close. It was then verified that the cooling system is capable of removing the heat generated in the inductor, estimating a water temperature difference between output and input of 4.8 °C. As last, the search for a material to be placed between cylinder and inductor. It must be a good electrical insulator and it can reach high temperatures. Alumina 94, a ceramic material, was chosen. Once manufactured the inductor, it came the experimental part. Chosen the power supply that best meets our requirements in terms of frequency, three heating were performed. They differ in the power provided: 20, 30 and 40 kW. In addition to thermal measurements, obtained with Ni – NiCr thermocouples, electrical measurements concern current, voltage and active power. In order to know absorbed active power, in absence of a wattmeter, three approaches were adopted. The best is based on current and voltage waveforms’ measurements: integrating their product active power is calculated. Thermal results are satisfying, in particular with 40 kW with a difference of 200 °C between “hot” and “cold” zones. The comparison between numerical models and measurements is very good for the “cold” areas. In the “hot” zones temperature estimates are 20 – 80 °C below than values measured, with relative error between 2 and 7%. The reasons are to be found in the incorrect knowledge of material properties and in the fact that the model is axisymmetric and not 3-D. In the last part is simulated with PSPICE® the circuit behaviour of the entire system: power supply, capacitor bank and inductor-load. There is a good arrangement between measures and numerical results.

Sommario

In questa tesi viene analizzato un sistema innovativo di riscaldamento a induzione da impiegare nei processi di forgiatura. Viene studiato il riscaldamento non uniforme di un cilindro di acciaio magnetico, con lo scopo di ottenere due zone “calde”, che raggiungono una temperatura di circa 1050 – 1100 °C, separate da un “fredda” che raggiunge una temperatura variabile tra gli 800 e i 950 °C. Il principale vantaggio è la possibilità di semplificare il processo di pre-forgiatura e al tempo stesso risparmiare energia rispetto a un riscaldamento tradizionale. La prima parte dello studio è stata svolta usando un programma FEM, realizzando vari modelli ognuno con una diversa geometria dell’induttore. Nei modelli si tiene conto della dipendenza della permeabilità rispetto al campo magnetico. Per garantire maggiore semplicità, si è pensato di realizzare un unico induttore con spire che si addensano nelle zone “calde”. Allo scopo di ottenere un profilo termico più uniforme possibile, in ogni zona, il passo tra le spire si riduce ai bordi e aumenta al centro. Lo scopo è garantire un andamento quanto più costante del campo magnetico. Altri sono poi stati gli argomenti fonte d’indagine. In primis l’influenza, in termini di campo d’induzione, che i terminali dell’induttore esercitano sull’induttore stesso. La variazione del modulo è superiore al 2% solo ai bordi, quando terminali e induttore sono molto vicini. E’ stato poi accertato che il sistema di raffreddamento fosse capace di asportare il calore generato nell’induttore. Si è stimata una differenza di temperatura dell’acqua tra uscita e ingresso di 4.8 °C. Da ultimo, la ricerca di un materiale da interporre tra cilindro e induttore che fosse capace di garantire l’isolamento elettrico e sopportasse alte temperature. La scelta è ricaduta su un materiale ceramico, l’allumina 94. Una volta pronto l’induttore, è stata svolta la parte sperimentale. Scelto un convertitore statico in grado di operare nell’intervallo di frequenze desiderato, i riscaldamenti sono stati svolti fissando la potenza assorbita dall’inverter: 20, 30 o 40 kW. Oltre alle misure termiche, ottenute con termocoppie di tipo Ni – NiCr, e quelle di tensione e corrente, è stata misurata la potenza elettrica assorbita dal sistema induttore-carico. Per effettuare questa misura, in assenza di un wattmetro, tre diversi metodi sono stati impiegati. Il migliore si basa sulla misura delle forme d’onda di tensione e corrente per mezzo di un oscilloscopio. Il prodotto tra queste due grandezze, se integrato in un numero finito di periodi, fornisce la potenza attiva. I risultati dei riscaldamenti sono soddisfacenti, soprattutto nel caso di potenza applicata pari a 40 kW dove la differenza tra zone “calde” e “fredde” si stima intorno ai 200 °C. Il confronto tra risultati dei modelli numerici e le misure è in buon accordo nelle zone “fredde”, di meno in quelle “calde”. Qui la temperatura prevista è inferiore di circa 20 – 80 °C di quella misurata, il che corrisponde a un errore relativo del 2 – 7%. I motivi sono da ricercare nella non corretta conoscenza dei parametri del materiale e nel fatto che il modello sia assialsimmetrico e non 3D. Nell’ultima parte viene simulato con PSPICE® il comportamento circuitale dell’intero sistema: convertitore statico, banco di condensatori e induttore-carico. C’è ottimo accordo tra misure e risultati numerici.

Acknowledgment

I would like to thank my supervisors Pf. Dr. – Ing. Egbert Baake and Dipl. – Ing. Thomas Steinberg. Pf. Baake for the possibility of carrying out my master thesis at Institut für Elektroprozessstechnik and for his moral and scientific support. Ing. Steinberg for his constant presence and his daily help in the genesis and implementation of my project.

This thesis would not been possible without the help of the whole staff of the ETP, either morally or in technical matters. Especially I would like to thank Mr Köppen for having manufactured my inductor. A special thanks also to Dr. – Ing. Nikaronov for his valuable explanations and Ing. Schülbe for his support in the practical part. Additionally I would like to thank Ing. Mikulski, Ing. Ebel, Dr. Phys. Spitans, Mr Görsch.

Not last, a particular thanks to Ing. Forzan for having organized my period abroad and for his precious support.

The greatest thanks goes to my family, Giorgio, Rossella and Giacomo, which always supports me morally and economically. To finish, a great thanks to all my friends who were always present.

Contents

| | |
|--|----|
| 1. Introduction | |
| 1.1 <i>About forging processes</i> | 13 |
| 1.2 <i>Aim of study</i> | 14 |
| 1.3 <i>Approach to the analysis</i> | 14 |
| | |
| 2. Theory of induction heating | |
| 2.1 <i>About induction heating</i> | 17 |
| 2.1.1 Principles | 17 |
| 2.1.2 Induction heating processes and system | 20 |
| 2.2 <i>Heating of a cylindrical work-piece</i> | 22 |
| 2.2.1 Maxwell equations solution | 22 |
| 2.2.2 Power induced and equivalent impedance | 28 |
| 2.2.3 Equations for an indefinite half plane | 30 |
| 2.2.4 Heating of hollow cylindrical body | 31 |
| 2.2.5 Coil's own resistance and inductance | 34 |
| 2.2.6 Electrical efficiency | 35 |
| 2.2.7 Merit and power factor | 36 |
| 2.2.8 Thermal transient in a cylindrical body | 37 |
| 2.2.9 Variations in the characteristic of material | 42 |
| | |
| 3. Numerical models | |
| 3.1 <i>Finite element analysis</i> | 49 |
| 3.1.1 Electromagnetic and thermal analysis | 49 |
| 3.1.2 PDE's solution | 52 |
| 3.2 <i>Ansys Mechanical Apdl</i> | 54 |
| 3.2.1 Pre-processing: geometry, material, mesh | 57 |
| 3.2.2 Magnetic permeability dependency on H | 61 |
| 3.3 <i>Goal of investigation</i> | 63 |
| 3.4 <i>Inductor's design</i> | 65 |
| 3.4.1 Frequency | 65 |
| 3.4.2 Inductor – work-piece air gap | 66 |
| 3.4.3 Inductor's thickness | 66 |
| 3.5 <i>Cases of study</i> | 67 |
| 3.5.1 First model | 68 |
| 3.5.2 Second model | 70 |
| 3.5.3 Third model | 72 |
| 3.5.4 Fourth model | 74 |
| 3.6 <i>Final model</i> | 77 |
| 3.6.1 Input | 78 |

| | | |
|-----------|--------------------------------------|-----|
| 3.6.2 | Results | 78 |
| 3.7 | <i>Homogeneous vs. Inhomogeneous</i> | 82 |
| 4. | Practical activities | |
| 4.1 | <i>Power supply</i> | 86 |
| 4.1.1 | Converter topologies | 86 |
| 4.1.2 | Converter choice | 89 |
| 4.2 | <i>Inductor manufacturing</i> | 91 |
| 4.2.1 | Diameter and thickness | 91 |
| 4.2.2 | Inductor ends | 91 |
| 4.2.3 | Insulation and support | 94 |
| 4.2.4 | Inductor cooling | 94 |
| 4.3 | <i>Laboratorial activity</i> | 97 |
| 4.3.1 | Experimental setup | 97 |
| 4.3.2 | Electrical results | 99 |
| 4.3.3 | Electrical power measurement | 100 |
| 4.3.4 | Thermal results and comparison | 106 |
| 4.4 | <i>Simulating EMA TEC</i> | 108 |
| 5. | Summary | 113 |
| | Bibliography | 115 |
| | List of figures | 117 |

1. Introduction

1.1 About forging processes

Forging is a manufacturing process involving the shaping of metal using localized compressive forces, which are delivered with a hammer or a die. Forging is often classified according to the temperature at which is performed: cold, warm and hot. In hot forging, in the case of steel, is reached a temperature between 1050 and 1200°C, sufficiently high to provoke the recrystallization of the material. At elevate temperatures, metals soften and become more ductile providing convenience in the manufacturing of complex work-pieces. But there are also some disadvantages. The dimensional tolerances are hard to control due to the contraction of the piece after the cooling. Besides, on the one hand, surface quality is not as good as in the cold forging, on the other, a superior energy consumption is inevitable. Cold forging is conducted under recrystallization temperature. The main advantages are high strengths of the products and less waste of material. On the other side, high forming loads are required and formability is limited at low temperatures. When the final temperature is close to the crystallization point (700 – 950 °C in the case of steel), forming is called “warm”. It’s preferred thus, to achieve a good compromise between ductility, formability and geometry accuracy. This process has become more feasible with the advancements of forging technology, since the control of temperature and its distribution can be precisely followed.

There are a large number of forging processes that can be summarized as follows: closed die forging with or without flash, forward extrusion, backward extrusion, open die forging, orbital forging. Hereafter reference will made mainly to *open die forging*, a process in which metal is shaped by hammering or pressing between flat or simple countered dies. Open die forging gets its name from the fact that dies do not encase the workpiece, allowing it to flow. The general aim is to achieve a desired distribution mass before the successive operations.

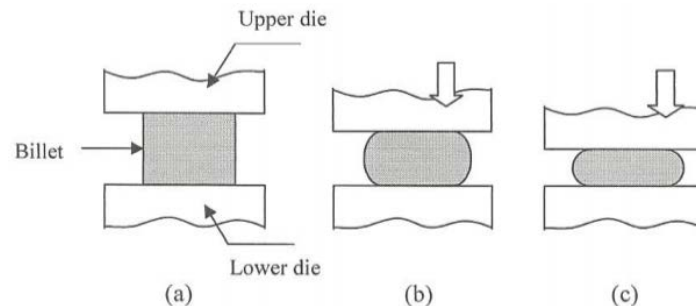


Figure 1.1 Open die forging. a) Start of process b) partial deformation c) final shape

1.2 Aim of study

Usually in forging processes blanks are heated and forged into a preform, then heated once again and forged into the end – form. In order to achieve this process special machines, like rollers, are needed to forge the blanks into a preform. Especially companies of small and medium size cannot integrate rollers cost efficiently into their production processes due to their small amount of production batches. From the technical point of view the preform helps to save material in the forging process.

The aim is to gain a good mass distribution in the form without using special machines. This solution can be reached adopting an “*inhomogeneous heating*” of the batch. The parts of the forging billet which are supposed to have a high material flux inside the form are heated until 1100 -1200 °C. The parts of the forging workpiece that are supposed not to have such a high material flux inside the form reach instead “colder” temperature between 800 and 900 °C. Once that the workpiece has been heated up, compressive forces are applied with consequent different behaviours that depend on temperature.

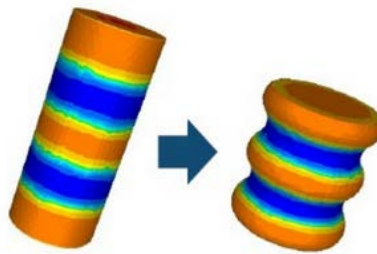


Figure 2.2 Open die forging in the case of “inhomogeneous” heating

An example is shown of Fig. 1.2 where the heated batch has been subjected to an open die forging process. Although this typology of heating has been so far only subject of research, its industrial applications are remarkable, and involve mainly forging processes of complex geometry such as crankshaft and camshaft.

A further advantage of this approach is related to the decrease of the amount of energy used, due to the fact that some parts are not heated as strong as in the case of homogeneous heating.

1.3 Approach to the analysis

The study pertains to the electrical and thermal analysis, i.e. to design an inductor capable of satisfying a defined temperature profile. In the design of an inductor, there are a large number of variables and parameters on which one can act. First the frequency at which the heating is carried out, but also the power and the current applied. If these quantities influence mainly the radial temperature distribution, the geometry of the inductor is a key element to differentiate the temperature in the axial direction. Moreover, the design feels the effects of both material’s typology and shape.

In this case, the billet is a cylinder of 42CrMo4 (carbon steel), 474 mm long with a diameter of 30 mm. The main goal is to design the inductor, in order to obtain a rectangular distribution of the axial temperature profile. It must be as squared as possible. Inevitably

between a “cold” and “hot” zone there is a transition. In a “hot” zone is reached a temperature between 1050 – 1100 °C, in a “cold” zone between 800 and 950 °C. These choices come from hot forging and warm forging temperature carbon steel. In a real application goal temperature is also affected by other aspects, like the workpiece transport time required from the place where the heating is run and where it is formed.

In Fig. 1.3 is shown a possible approach of how to get an inhomogeneous axial heating. It would be preferable to spend more turns to obtain a “hot” zone, and to increase the air gap in a “cold” area.

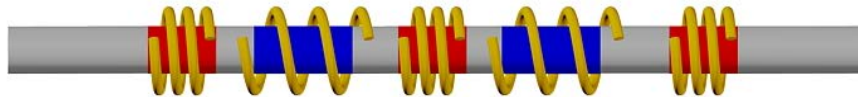


Figure 1.3 Explanatory sketch of how to get a differentiated heating in the axial direction

The idea of using one unique coil, where in every turn circulates the same current in terms of value and frequency, is perhaps the simplest solution, well suited to the demands of simplicity, cheapness and robustness of the industrial world. It permits to reduce the current necessary to produce a certain magnetic field too. This does not preclude a more detailed analysis, with the use of independent inductors, powered with different currents and frequencies. The possibility of obtaining a more satisfactory thermal profile is followed by an increase of complexity and cost.

In the following investigation, the numerical analysis is conducted using the commercial FEM simulation software ANSYS©. The simple geometry of the workpiece suggests to use a 2D axisymmetric model to reduce the computational cost. Once built up a model that responds to our needs, the next step is the manufacturing of the coil. Thus other issues appear to be critically analysed. First the feasibility of the inductor, the shape of the inductor ends, the cooling system’s ability to remove the heat, but also the thermal and electrical insulation between inductor and workpiece.

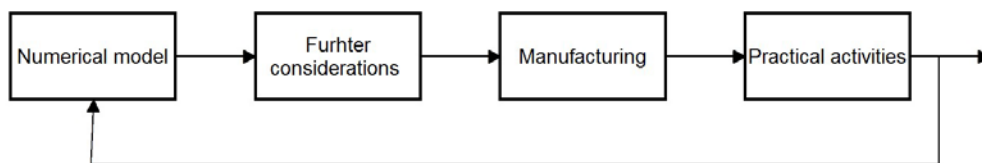


Figure 1.4 Macro scheme that shows how the investigation has been carried out

In the experimental part, in addition to thermal measurements, it has paid also attention to the electrical quantities, with the main purpose of measuring the active power induced inside the workpiece. It follows not only the comparison between measurements and numerical solutions, but also the possibility (from the active power knowledge) to determine the equivalent circuit parameters of the workpiece-inductor system. With these data it is simulated, using PSPICE®, the electrical behaviour of the overall system (power supply, capacitor bank, inductor and work-piece) in sinusoidal conditions.

2. Theory of induction heating

In this chapter are presented the main strengths of induction heating processes. The principle quantities are analysed with a theoretical approach but in order to obtain these results simplifying hypothesis are adopted.

2.1 About induction heating

Michael Faraday discovered in 1831 the basic principle involved in induction. In the very beginning, the theory of induction heating was studied in order to maximize the efficiency of transformers, motors and generators. By the early 20th century engineers started to look for ways to use properties of induction for the purpose of melting steel.

Nowadays induction heating is one of the most diffused processes for heating of electrically conductive elements, in many cases metallic materials. This technology is common in manufacturing industry because of the many factors of success. Among all, the development of the heat directly inside the material. This implies a rational use of electrical energy, high power density and good efficiency.

2.1.1 Principles

The general definition of induction heating is the production of a current inside a material due to a change in time of the concatenated flux. The variation of flux can occur in two ways: magnetic field constant with time and workpiece in motion or, magnetic flux that changes in time with fixed conductive material. In the following analysis let's consider the second case. An alternating voltage applied to an induction coil will result in an alternating current in the coil circuit. This current will produce in its surroundings a time – variable magnetic field that has the same frequency as the coil current. This magnetic field induces eddy currents in the workpiece located inside the coil. The currents produce heat by the Joule effect. In this way, the transfer of energy between the coil and the workpiece occurs without direct contact between elements.

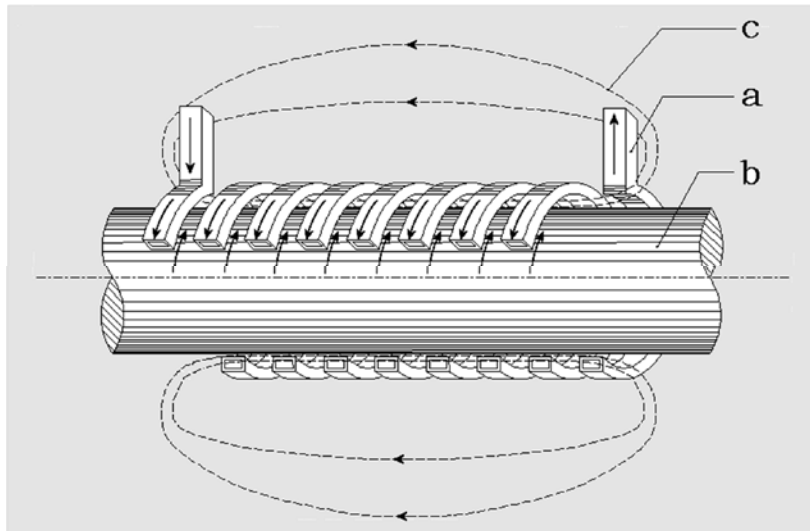


Figure 2.1. Typical layout with inductor (a), workpiece (b) and trend of magnetic field lines (c)

Because of several electromagnetic phenomena, including skin, ring and proximity effect, the current's distribution is not uniform, both in the piece and that in the coil.

Skin effect

When a DC current flows inside a conductor, its distribution is uniform in space. If instead an alternate current circulates, the current density is largest at the surface and decreases with greater depths in the conductor. In the case of a cylindrical conductor the decrease from the surface to core can be described with a decreasing exponential function. The current flows mainly in the “skin” of the conductor.

This happens because an alternating current produces an alternating magnetic field. The variation on time of magnetic field induces currents, as shown in Figure 2.2, which are additive in the outer layer and opposite close to the centre.

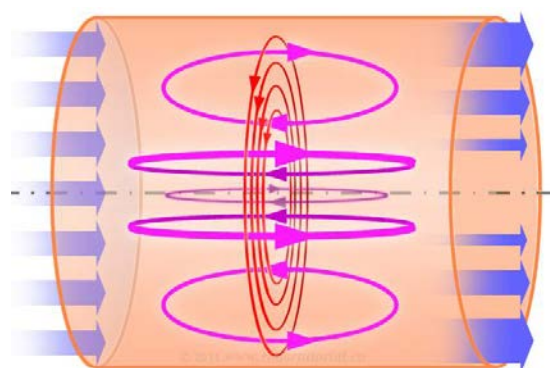


Figure 2.2. Skin effect in a conductor

The skin effect causes the increase of resistance in a conductor because the effective cross section is reduced. This phenomenon is maximized with the increase of frequency.

Proximity effect

When we discussed the skin effect in a conductor, we assumed that a conductor stands alone and that there are no other current carrying conductors in the surrounding area. In

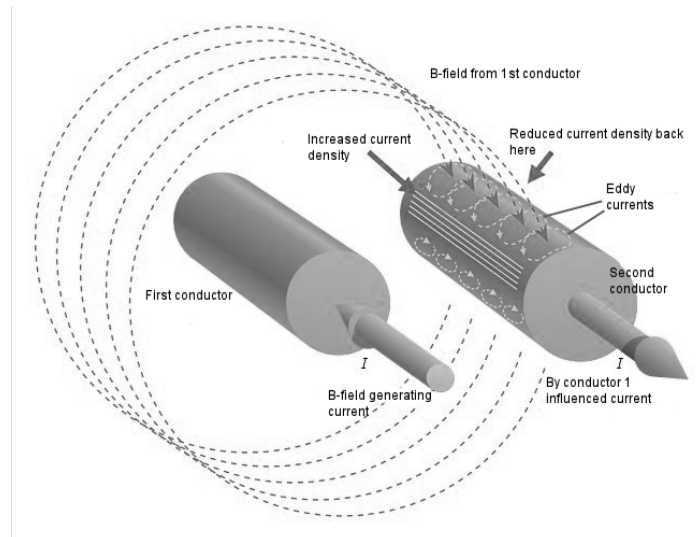


Figure 2.3 The proximity effect

most practical applications this is not verified. The proximity of two or more conductors provokes a redistribution of the current inside the conductors. Figure 2.3 shows an example where the currents are opposite.

The opposite direction of the currents causes an increase of the magnetic field in gap between the two conductors. The magnetic field lines produced by the first conductor penetrate the top of the second conductor and exit from the bottom, which induce eddy currents. The effect is to concentrate more current on the inside – facing surfaces of the conductors and less on the outward – facing sides. If the direction of the currents is the same, a weak magnetic field will exist between the bars. The external magnetic field is in this case stronger and the currents are gathering on the more distance surfaces. The skin and proximity effects are two manifestations of the same principle: magnetic flux lines cannot penetrate a good conductor. In fact it penetrates the good conducting material, but only with a certain penetration depth. In case of ideal insulating material the magnetic field penetrates the material or more clearly it passes without any consequence for the insulating material especially without inducing eddy currents or joule heat. The difference between skin and proximity effect is in the origin of the time variant magnetic flux. In the skin effect, the field is produced by the current flowing through it, instead in the proximity one, the field comes from another source.

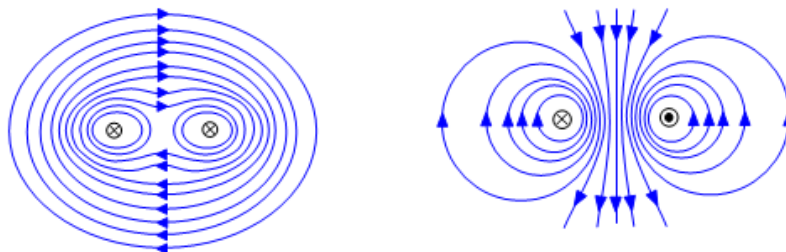


Figure 2.4 Magnetic flux lines with same or opposed currents direction

Ring effect

Up to now we have discussed current distribution in straight conductors. When a bar is bent to a shape it into a ring, magnetic field lines will be more concentrated inside the ring. As a result, most of the current flows within the thin inside surface layer of the ring.

2.1.2 Induction heating processes and system

Heating processes can be used to achieve the most different temperature profiles. Exist cases where a mere superficial warming up is pursued, as in the case of hardening. Vice versa in other situations a mass heating is desired. We are referring to forging, forming, extrusion and rolling.

There are four basic heating modes: static (also called single shot), progressive, pulse, oscillating. When referring to *static heating*, neither the workpiece nor the inductor moves linearly. This mode is efficiently used for selective hardening when only one part needs to be heated. Often rotation (also in the case of through heating) is added, if the part is cylindrical or rotational symmetric. The *progressive* mode can be used for heating tube and pipes with small external diameter. Example of long parts that require hardness include long tool holders used in deep oilwell drilling or in the mining industry. Usually three different steps of heating are adopted, which can be supplied with equal or different powers and frequencies. To protect the coils, guide rails can be added. If in hardening processes the coil is formed with a unique turn, in forging the inductor has several turns. When the phrase *pulse heating* is used it is usually referring to the method of using short bursts of heat to control or maintain a desired temperature profile. It is often used in induction hardening of gears, critical components and high carbon steel that have pronounced tendency to crack. This pulsing mode can be used in combination with dual frequency heating, like in the case of gears. As last, in an *oscillating heating* a component moves back and forth inside a single or multi coil with a space saving design approach. It's only used in mass heating processes.

The choice of the inductor allows freedom to the designer in obtaining a given heating profile (see Fig. 2.5).

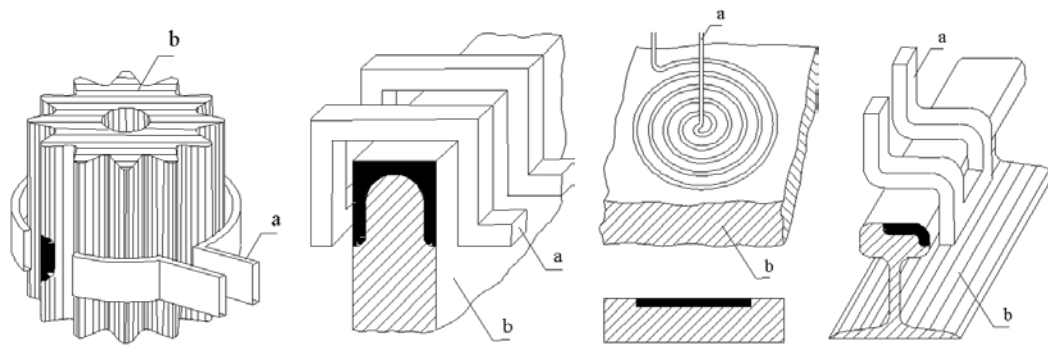


Figure 2.5 Examples of configurations inductor (a) load (b).

Depending on the requirements in different applications, the inductor is powered with a frequency that goes from 50 Hz to some MHz. It follows that different solid state components are used, as a function of the switching frequency and of the voltage and current they must carry.

If for relatively low frequencies, thyristors are used, for gradually increasing frequency IGBT are preferred. Other kinds, like “rotary iron” converters for frequencies between 1 and 10 kHz, are nowadays abandoned for reasons of cost, efficiency and reliability.

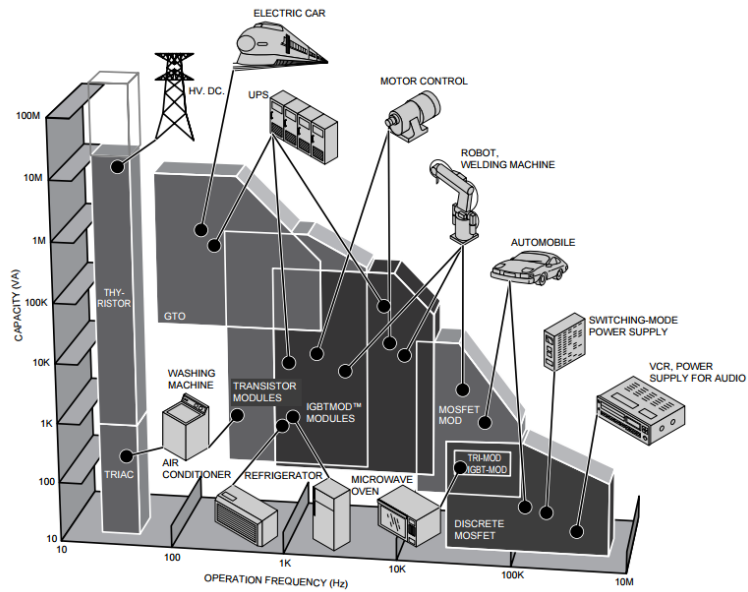


Figure 2.6 Solid state components as a function of frequency [Hz] and capacity [VA].

An induction heating system is made up of a converter that picks up the power from the grid (industrial frequency) and converts it at the frequency desired. Usually it occurs with two steps: in the first, through a diodes rectifier, there is the AC/DC conversion, in the second the DC/AC conversion. It is highlighted in Figure 2.7 the capacitor bank, always necessary for the power factor compensation, in most of the cases very low.

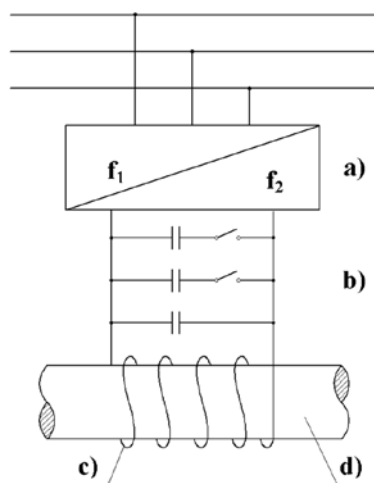


Figure 2.7 Principal components of an induction heating installation [a)power supply b)capacitor bank c)induction coil d)workpiece to heat]

2.2. Heating of a cylindrical work-piece

Let us consider, referring to Fig. 2.8, a solid cylinder with constant resistivity and permeability, placed inside a coil crossed by a sinusoidal current.

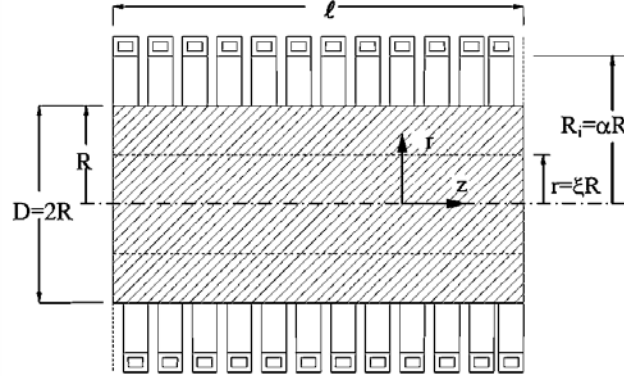


Figure 2.8. Sketch of inductor and cylindrical workpiece

A cylindrical coordinate system has been chosen (r, φ, z) , where:

| | |
|--------------------|---|
| R, R_i | Workpiece's external radius and internal radius of the coil [m] |
| $\xi = r / R$ | Non dimensional radius ($0 \leq \xi \leq 1$) |
| $\alpha = R_i / R$ | $\alpha > 1$ |
| l | Coil's and workpiece's axial length [m] |
| N | Number of turns |
| I | Root mean square of the coil's current [A] |
| f | Frequency [Hz] |
| $\omega = 2\pi f$ | Current's pulsation [rad/s] |
| μ_0 | Vacuum magnetic permeability ($4\pi \cdot 10^{-7}$ [H/m]) |
| ρ, μ | Cylinder's electrical resistivity [$\Omega \cdot m$] and relative magnetic permeability |

2.2.1 Maxwell equations solution

We assume that the inductor is part of a cylindrical configuration of infinite length. This means that the magnetic field, in the air gap between piece and coil, has direction only along z and value equal to:

$$\overline{H}_0 = \frac{NI}{l} \quad (2.1)$$

Where a generic sinusoidal quantity $a(t) = \sqrt{2} A \sin(\omega t + \alpha)$ is represented using Steinmetz's transformation: $\overline{A} = A e^{j\alpha}$.

From Maxwell's Laws:

$$\nabla \cdot \mathbf{D} = \rho_c \quad (2.2)$$

$$\nabla \cdot \mathbf{B} = 0 \quad (2.3)$$

$$\nabla \times \mathbf{E} = - \frac{\partial \mathbf{B}}{\partial t} \quad (2.4)$$

$$\nabla \times \mathbf{H} = - \frac{\partial \mathbf{D}}{\partial t} + \mathbf{G} \quad (2.5)$$

With: ρ_c , volumetric charge density [C/m³], \mathbf{D} electrical induction [C/m²], \mathbf{E} electric field [V/m], \mathbf{H} magnetic field [A/m], \mathbf{B} magnetic induction [T], \mathbf{G} current density [A/m²].

And constitutive equations:

$$\mathbf{D} = \varepsilon \varepsilon_0 \mathbf{E} \quad (2.6)$$

$$\mathbf{B} = \mu \mu_0 \mathbf{H} \quad (2.7)$$

$$\mathbf{E} = \rho \mathbf{G} \quad (2.8)$$

We assume the current sinusoidal, a linear behaviour of the materials and neglect the term that takes into account displacement currents $-\text{dD}/\text{dt}$ in (2.5). This last assumption is verified as much is lower is the frequency.

$$\text{rot} \bar{\mathbf{H}} = \frac{\bar{\mathbf{E}}}{\rho} \quad (2.9)$$

$$\text{rot} \bar{\mathbf{E}} = -j\omega\mu\mu_0 \bar{\mathbf{H}} \quad (2.10)$$

From the hypothesis done, the only non-null components are:

$$\bar{\mathbf{G}}(\mathbf{r}) = (0, \bar{G}_\varphi, 0)$$

$$\bar{\mathbf{H}}(\mathbf{r}) = (0, 0, \bar{H}_z)$$

In a cylindrical coordinate system, the value of rotor of a generic vector \mathbf{A} , is calculable as:

$$\text{rot} \mathbf{A} = \left[\frac{1}{r} \frac{\partial A_z}{\partial \varphi} - \frac{\partial A_\varphi}{\partial z} \right] \underline{\mathbf{u}}_r + \left[\frac{\partial A_r}{\partial z} - \frac{\partial A_z}{\partial r} \right] \underline{\mathbf{u}}_\varphi + \left[\frac{1}{r} \frac{\partial(rA_\varphi)}{\partial r} - \frac{\partial A_r}{\partial \varphi} \right] \underline{\mathbf{u}}_z \quad (2.11)$$

Follows:

$$[\text{rot} \bar{\mathbf{H}}]_\varphi = -\frac{\partial \bar{H}_z}{\partial r} = \frac{\bar{E}_\varphi}{\rho} \quad (2.12)$$

$$[\text{rot} \bar{\mathbf{E}}]_z = -\frac{\partial \bar{E}_\varphi}{\partial r} + \frac{\bar{E}_\varphi}{r} = -j\omega\mu\mu_0 \bar{H}_z \quad (2.13)$$

Hence we're omitting subscript. Using (2.12) in (2.13):

$$\frac{d^2 \bar{H}}{dr^2} + \frac{1}{r} \frac{d\bar{H}}{dr} - j \frac{\omega\mu\mu_0 \bar{H}}{\rho} = 0 \quad (2.14)$$

If we define:

$$\delta = \sqrt{\frac{2\rho}{\omega\mu\mu_0}} \quad \text{Penetration depth [m]}$$

$$m = \frac{\sqrt{2}R}{\delta} \quad \beta^2 = -j \frac{\omega\mu\mu_0}{\rho} R^2 = -jm^2$$

We obtain:

$$\frac{d^2 \bar{H}}{d\xi^2} + \frac{1}{\xi} \frac{d\bar{H}}{d\xi} + \beta^2 \bar{H} = 0 \quad (2.15)$$

The solution is known and is of the type: $\bar{H}=C_1J_0(\beta\xi)+C_2Y_0(\beta\xi)$ (2.16)

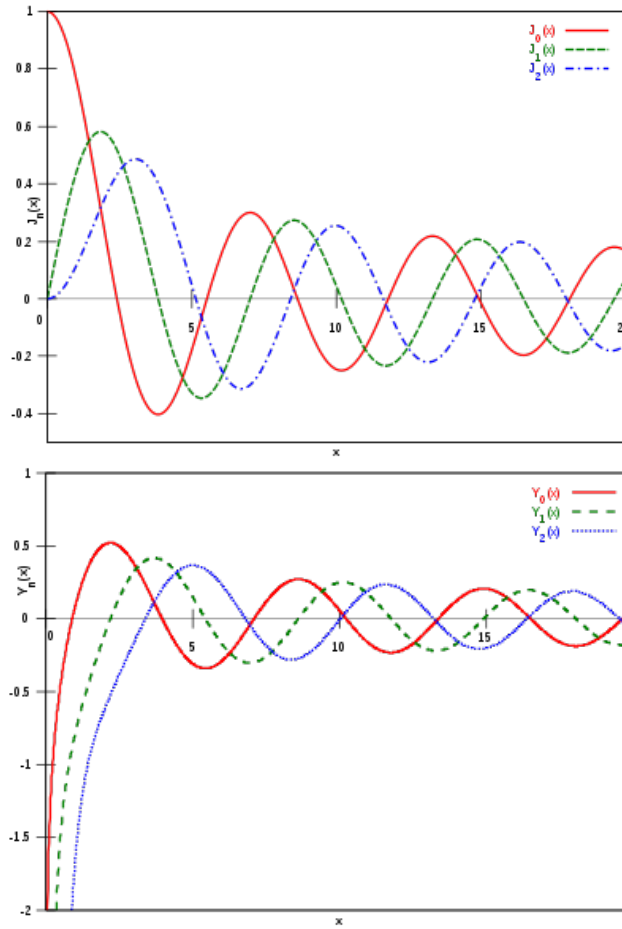


Figure 2.9. First and second type Bessel functions

Where J_0 and Y_0 are order zero, first and second type Bessel function (see Fig. 2.9). Constants C_1 and C_2 can be evaluated from the boundary conditions:

$$|\bar{H}| \neq \infty \quad \text{if } \xi=0$$

$$\bar{H} = \bar{H}_0 \quad \text{if } \xi=1$$

Since $Y_0(0) = -\infty$, as shown in figure, follows that $C_2=0$. From the second is obtained $C_1 = \frac{\bar{H}_0}{J_0(\beta)}$. Replacing C_1 and C_2 in (2.16):

$$\bar{H} = \bar{H}_0 \frac{J_0(\beta \xi)}{J_0(\beta)} = \bar{H}_0 \frac{J_0(\sqrt{-jm} \xi)}{J_0(\sqrt{-jm})} \quad (2.17)$$

It is more practical to separate real and imaginary part of $J_0(\sqrt{-ju})$ as:

$$J_0\left(\sqrt{-ju}\right) = \text{ber}(u) + j\text{bei}(u) \quad (2.18)$$

So that (2.17) becomes: $\bar{H} = \bar{H}_0 \frac{\text{ber}(m \xi) + j\text{bei}(m \xi)}{\text{ber}(m) + j\text{bei}(m)}$

(2.17) can be also written with eulerian formulation and its module calculated:

$$\bar{H} = \bar{H}_0 \frac{M(m \xi) e^{j\theta(m \xi)}}{M(m) e^{j\theta(m)}} \quad (2.17')$$

$$\left| \frac{\bar{H}}{\bar{H}_0} \right| = \sqrt{\frac{\text{ber}^2(m\xi) + \text{bei}^2(m\xi)}{\text{ber}^2(m) + \text{bei}^2(m)}} \quad (2.17'')$$

The relations (2.17') and (2.17'') emphasize that by varying the radius not only changes the amplitude of magnetic field, but also its phase angle.

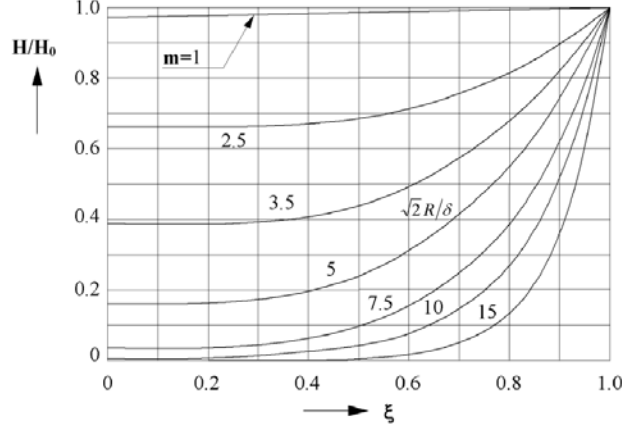


Figure 2.10. Magnetic field module trend inside the workpiece

Due to the induced currents, magnetic field lines thicken mainly in the superficial layers. This is effect is clean cut with high values of m .

The intensity of electric field and the trend of eddy currents are deductible from (2.12) and (2.17), reminding that $J'_0(u) = -J_1(u)$:

$$\bar{E} = \sqrt{-j} \bar{H}_0 \frac{\rho}{\delta} \sqrt{2} \frac{J_1(\sqrt{-jm} \xi)}{J_0(\sqrt{-jm})} \quad (2.19)$$

$$\bar{G} = \frac{\bar{E}}{\rho} = \sqrt{-j} \bar{H}_0 \frac{\sqrt{2}}{\delta} \frac{J_1(\sqrt{-jm} \xi)}{J_0(\sqrt{-jm})} \quad (2.20)$$

If we call \bar{E}_0, \bar{G}_0 the values at cylinder's surface ($\xi=1$),

$$\bar{E}_0 = \sqrt{-j} \bar{H}_0 \frac{\rho}{\delta} \sqrt{2} \frac{J_1(\sqrt{-jm})}{J_0(\sqrt{-jm})}$$

$$\bar{E} = \bar{E}_0 \frac{J_1(\sqrt{-jm} \xi)}{J_1(\sqrt{-jm})} \quad (2.21)$$

$$\bar{G} = \bar{G}_0 \frac{J_1(\sqrt{-jm} \xi)}{J_1(\sqrt{-jm})} \quad (2.22)$$

From (2.19) and (2.20), dividing real and imaginary part:

$$\bar{G} = \frac{\bar{E}}{\rho} = -\frac{\bar{H}_0}{R} m \frac{\text{ber}'(m\xi) + j\text{bei}'(m\xi)}{\text{ber}(m) + j\text{bei}(m)} \quad (2.20')$$

$$\frac{\bar{E}}{\bar{E}_0} = \frac{\bar{G}}{\bar{G}_0} = \frac{\text{ber}'(m\xi) + j\text{bei}'(m\xi)}{\text{ber}'(m) + j\text{bei}'(m)} \quad (2.23)$$

$$\left| \frac{\bar{E}}{\bar{E}_0} \right| = \left| \frac{\bar{G}}{\bar{G}_0} \right| = \sqrt{\frac{\text{ber}^2(m\xi) + \text{bei}^2(m\xi)}{\text{ber}^2(m) + \text{bei}^2(m)}} \quad (2.23')$$

Current density is null in the axis, in fact current has no way to close. Quantities inside the piece are phase shifted and are reduced in amplitude compare to those in the surface.

$$\bar{G}_0 = \frac{\bar{E}_0}{\rho} = \sqrt{-j} \bar{H}_0 \frac{\sqrt{2}}{\delta} \frac{J_1(\sqrt{-j}m)}{J_0(\sqrt{-j}m)} = -\frac{\bar{H}_0}{R} m(P+jQ) \quad (2.24)$$

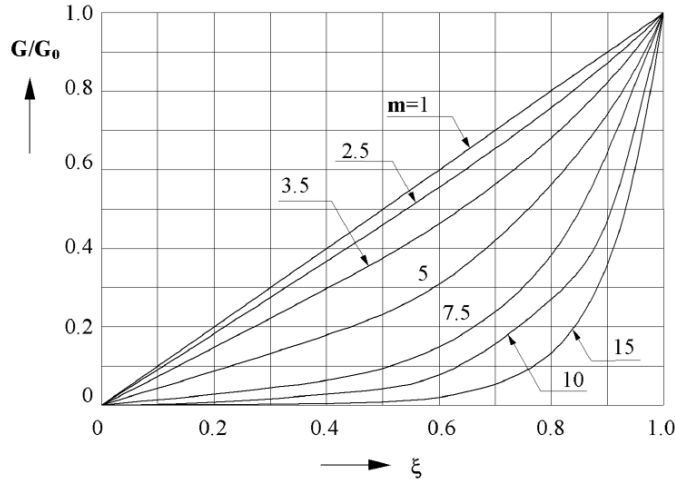


Figure 2.11. Current density function of ξ and m

Having defined: $P+jQ = -\sqrt{-j} \frac{J_1(\sqrt{-j}m)}{J_0(\sqrt{-j}m)} = \frac{\text{ber}'(m) + j\text{bei}'(m)}{\text{ber}(m) + j\text{bei}(m)}$

P and Q are numbers, only function of “m” and, as explained later, they play an important role in determining the power transferred to the workpiece. P and Q tend to $\frac{1}{\sqrt{2}}$ for m that tends to infinite.

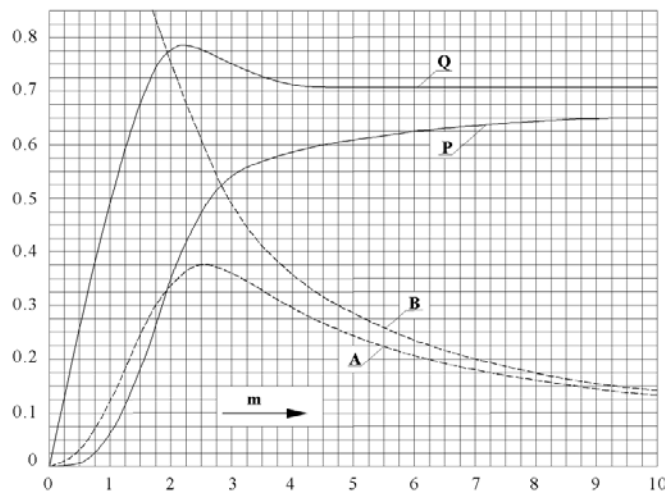


Figure 2.12. Values of P and Q, as a function of m

From (2.24), if we consider the module:

$$G_0 = \frac{H_0}{R} m \sqrt{P^2 + Q^2} \quad (2.24')$$

We deduct that with the same workpiece, the same H_0 , changing the frequency, G_0 changes. In other word, increasing the frequency means increasing the superficial current. An example is shown on Figure 2.13.

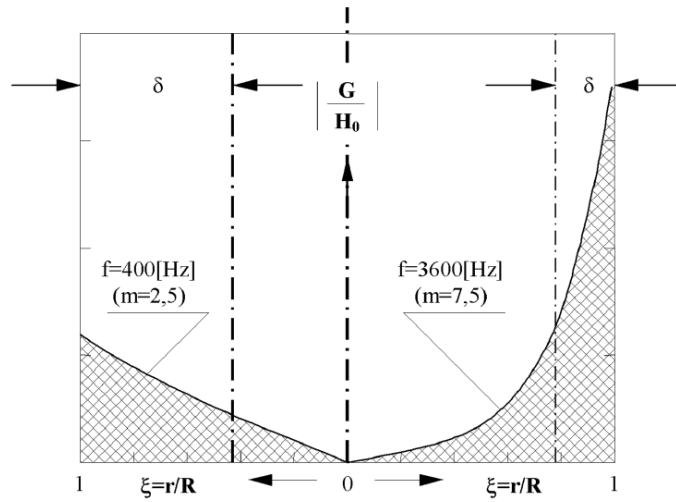


Figure 2.13. How current density changes with $f = 400$ Hz or $f = 3600$ Hz

At this point is easy to get, from the current density, the distribution of the induce power per unit volume. In fact $w = \rho G^2$ is the specific power in correspondence of a generic radius, and w_0 the specific induced power in the surface of the cylinder.

$$\left| \frac{w}{w_0} \right| = \left| \frac{J_1(\sqrt{-jm}\xi)}{J_1(\sqrt{-jm})} \right|^2 = \frac{\text{ber}^2(m\xi) + \text{bei}^2(m\xi)}{\text{ber}^2(m) + \text{bei}^2(m)} \quad (2.25)$$

$$w_0 = \rho \frac{H_0^2}{R^2} m^2 (P^2 + Q^2) \quad (2.26)$$

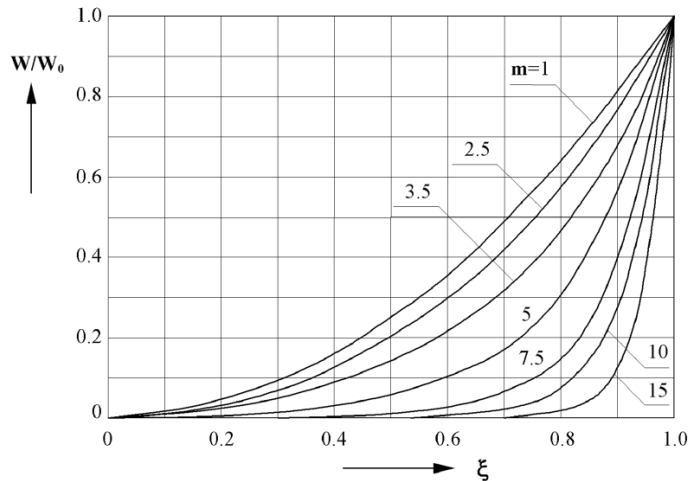


Fig. 2.14 Power induced inside the workpiece

From (2.26) is evident that, with other parameters equal, an increase of the frequency leads to heat up much more the surface instead of the axis. The distribution of induced power is much more non-uniform compared to the current density.

The following approximations are allowed in order to simplify the analysis:

$$\text{If } m \leq 1, \quad \frac{H}{H_0} \approx 1, \quad \frac{G}{G_0} \approx \xi \text{ and } \frac{w}{w_0} \approx \xi^2$$

$$\text{If } m \text{ enough high} \quad \frac{H}{H_0} \approx \frac{G}{G_0} \approx \frac{e^{-x/\delta}}{\sqrt{1-(\frac{x}{R})}} \text{ and } \frac{w}{w_0} \approx \frac{e^{-2x/\delta}}{1-(\frac{x}{R})} \quad \text{with } x = R - r$$

2.2.2 Power induced and equivalent impedance

Active and reactive power transmitted to the cylinder through the electromagnetic field can be calculated as real and imaginary part of the Poynting vector flow coming out from the cylinder surface.

$$\bar{\mathbf{p}} = \bar{\mathbf{E}} \times \bar{\mathbf{H}}^* \quad (2.27)$$

Taking into account the perpendicularity between $\bar{\mathbf{E}}$ and $\bar{\mathbf{H}}$, and that their value \bar{E}_0 and \bar{H}_0 at the surface, if P_C, Q_C are active and reactive power involved inside the cylinder:

$$P_C + j Q_C = \int_S \bar{\mathbf{p}} \cdot \bar{\mathbf{n}} dS = -2\pi R l \bar{E}_0 \bar{H}_0$$

If we substitute (2.24) $\bar{E}_0 = -\frac{\bar{H}_0}{R} m \rho (P + jQ)$, and we consider the definition of “ δ ”:

$$P_C + j Q_C = (2\pi R l) H_0^2 \frac{m}{R} \rho (P + jQ) = (2\pi R l) H_0^2 \sqrt{2} \frac{\rho}{\delta} (P + jQ) \quad (2.27')$$

Defining:

$$A + jB = \frac{2}{m} (P + jQ) \quad \text{where its trend is shown in Fig. 2.12}$$

$$x_{i0} = \omega N^2 \frac{\mu_0 \pi R^2 a^2}{l} \quad \text{reactance of the coil without load } [\Omega]$$

$$P_C + j Q_C = \frac{N^2 I^2}{l^2} \sqrt{2} \frac{\rho}{\delta} (P + jQ) (2\pi R l) \frac{m}{m} = \frac{x_{i0}}{a^2} \mu (A + jB) I^2 \quad (2.27'')$$

In order to size the inductor is fundamental the calculus of the inductor - load equivalent impedance. A series equivalent circuit is preferred instead of a parallel one, since the current is known. At the moment the inductor's resistance is neglected.

The reactive power involved in the air gap between the workpiece and the coil can be computed using magnetic energy density [W/m^3] formula:

$$w_m = \frac{1}{2} \mathbf{H} \cdot \mathbf{B} \quad (2.28)$$

Integrating in the air volume:

$$W_m = w_m \pi (R_i^2 - R^2) l = \frac{1}{2} \mu_0 H_0^2 \pi (R_i^2 - R^2) l \quad (2.28')$$

The magnetic energy expression can also be written as $W_m = \frac{1}{2} L_a I^2$ instead the reactive power exchanged by and inductance is $Q_a = X I^2$. From (2.28') is easy to obtain:

$$Q_a = 2\omega W_m = \frac{x_{i0}}{\alpha^2} (\alpha^2 - 1) I^2 \quad (2.29)$$

It is better to have low α in order to minimize the reactive power absorbed, but at the same time α shouldn't be too small, because of the radiation from the workpiece to the inductor. Generally it assumes values between 1,1 and 1,4.

Adding (2.27'') and (2.29) we obtain the overall active and reactive power reported to the terminals of the inductor.

$$\dot{S} = P_C + j(Q_a + Q_C) = \frac{x_{i0}}{\alpha^2} \{ \mu A + j[\alpha^2 - (1 - \mu B)] \} I^2 \quad (2.30)$$

The equivalent impedance z'_{e0} seen from inductor's terminal is:

$$z'_{e0} = \frac{\dot{S}}{I^2} = r'_c + j(x_a + x'_c) = r'_c + j(x_{i0} - \Delta x) \quad (2.31)$$

We have:

$$\begin{aligned} r'_c &= \frac{x_{i0}}{\alpha^2} \mu A = N^2 \rho \frac{2\pi R}{l_0} \sqrt{2P} && \text{load resistance reported to inductor's terminals} \\ x'_c &= \frac{x_{i0}}{\alpha^2} \mu B && \text{load reactance reported to inductor's terminals} \\ x_a &= \frac{x_{i0}}{\alpha^2} (\alpha^2 - 1) && \text{reactance corresponding to the reactive power} \\ &&& \text{involved in the air gap between inductor and load.} \\ \Delta x &= \frac{x_{i0}}{\alpha^2} (1 - \mu B) && \text{variation between without and with workpiece.} \end{aligned}$$

It is good to underline that positive values of Δx lead to decrease of the overall inductance. For a non magnetic material, since B is smaller than one with $m > 2$, the total reactance always decreases in the case with the workpiece compared to the case with "empty" inductor. Instead, in a ferromagnetic material, since $\mu \gg 1$, there is the possibility that Δx is negative and a rise of the impedance occurs. It depends most of all on the frequency because $B = \frac{2}{m} Q$. Typically with low frequencies $\Delta x < 0$, but with high values of "m" the effect of demagnetization currents is so strong that $\Delta x > 0$ and a decrease of the overall inductance occurs.

The value of the equivalent impedance can be also computed starting from the total concatenated flux with the coil. Always neglecting the resistance of the inductor, we define:

| | |
|----------|--|
| V_0 | Inductor's voltage [V] |
| Z_{e0} | Equivalent inductor – load impedance [Ω] |
| Φ | Total concatenated flux with the inducer coil [Wb] |
| Φ_c | Total flux inside the workpiece [Wb] |
| Φ_a | Flux among workpiece and coil [Wb] |

From (2.17) we have:

$$\overline{\Phi}_c = \mu_0 \mu \int_0^R 2\pi r \bar{H} dr = \frac{\mu_0 \mu \bar{H}_0 2\pi R^2}{J_0(\sqrt{-jm})} \int_0^1 \xi J_0(\sqrt{-jm} \xi) d\xi \quad (2.32)$$

Since $\int_0^1 \xi J_0(\beta \xi) d\xi = \frac{J_1(\beta)}{\beta}$, (2.32) becomes: (2.32')

$$\overline{\Phi}_c = \mu_0 \mu \bar{H}_0 2\pi R^2 \frac{J_1(\sqrt{-jm})}{J_0(\sqrt{-jm}) \sqrt{-jm}} = \mu_0 \mu \bar{H}_0 2\pi R^2 (P+jQ) \frac{1}{jm} =$$

$$= \mu_0 \mu \bar{H}_0 \pi \delta^2 m(Q-jP)$$

$$\overline{\Phi}_a = \int_R^{R_1} \mu_0 \bar{H}_0 2\pi r dr = \mu_0 \bar{H}_0 \pi (R_1^2 - R^2) = \mu_0 \bar{H}_0 \pi R^2 (\alpha^2 - 1) \quad (2.33)$$

The value of the equivalent impedance is so computable from (2.32') and (2.33).

$$z_{e0} = \frac{\overline{V}_0}{\bar{I}} = \frac{j\omega N \overline{\Phi}}{\bar{I}} = \frac{j\omega N (\overline{\Phi}_a + \overline{\Phi}_c)}{\bar{I}} = \frac{x_{i0}}{\alpha^2} \{ \mu A + j[\alpha^2 - (1 - \mu B)] \}$$

2.2.3 Equations for an indefinite half plane

For very high value of “m” the magnetic field affects only the superficial layers of the cylinder, that is that zones where ξ is close to 1. In these conditions relations seen above can be still simplified as:

$$\frac{H}{H_0} = \frac{G}{G_0} \approx e^{-x/\delta} \quad (2.34)$$

$$\frac{w}{w_0} \approx e^{-2x/\delta}$$

Becoming like those valid for the penetration of an electromagnetic wave in a indefinite semi plane with intensity of the field H_0 applied to its surface. In a cylinder this is verified when “m” is so elevated that the curvature is negligible.

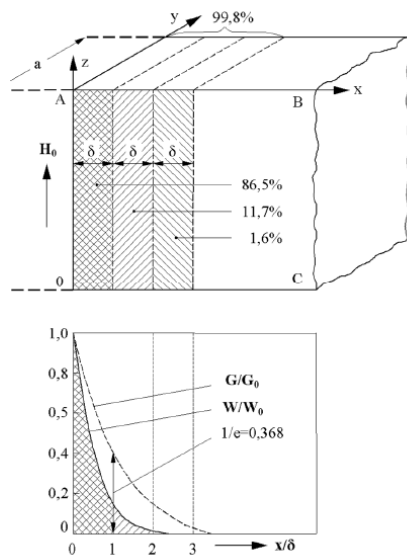


Figure 2.15. Current density and induced power inside an infinite semi plane

In Fig. 2.15 is easy to see that for distances bigger than $(2 \div 3) \delta$ current density is few percent compare to superficial value, instead the power density is almost zero. In fact δ and 2δ are the decay spatial constants in the first and second case. As shown in figure, powers turned into heat in the three layers thick δ are in each 86.5%, 11.7% and 1.6%. Adding these values we obtain more than 99% of the overall power.

From (2.24'), since $m \rightarrow \infty$ ($Q, P \rightarrow \frac{1}{\sqrt{2}}$), $G_0 = \frac{H_0}{R} m \left(\sqrt{P^2 + Q^2} \right) = \frac{H_0 \sqrt{2} R}{R \delta} = \frac{\sqrt{2} H_0}{\delta}$

And so, $w_0 = \rho G_0^2 = H_0^2 \frac{2\rho}{\delta^2}$

We apply Ampere's Law in order to calculate the total induced current I' in a element with length " l ". The current must be perpendicular to the magnetic field and it has direction only along y axis.

$$I' = \oint_{OABC} \mathbf{H} \cdot \mathbf{t} \, ds = H_0 l = \delta \frac{G_0}{\sqrt{2}} \quad (2.35)$$

It is equivalent to think at the induced current I' as uniformly distributed in a thickness δ with density $\frac{G_0}{\sqrt{2}}$.

The active power P_x involves between the surface and a thickness x , length l (among z) and deep a (among y) is:

$$P_x = l a \int_0^x w \, dx = l a w_0 \int_0^x e^{-2x/\delta} \, dx = l a H_0^2 \frac{\rho}{\delta} (1 - e^{-\frac{2x}{\delta}}) \quad (2.36)$$

At limit with $x \rightarrow \infty$ we get the total power induced $P_c = \lim_{x \rightarrow \infty} P_x = l a H_0^2 \frac{\rho}{\delta}$

The total active and reactive power in one element with length l and deep a is calculated with the same approach adopted with the cylinder:

$$P_c + jQ_c = -\overline{E_0} \overline{H_0} l a = -\rho \overline{G_0} \overline{H_0} l a = H_0^2 \frac{\rho}{\delta} l a (1+j) = N^2 \frac{\rho a}{\delta l} (1+j) I^2$$

Follows the expression of the equivalent impedance:

$$z_{cc} = N^2 \frac{\rho a}{\delta l} (1+j) \quad (2.37)$$

2.2.4 Heating of hollow cylindrical bodies

Let's consider a hollow cylindrical body with infinite length shown in Figure 2.16, with imposed longitudinal magnetic field that assumes values of \dot{H}_e and \dot{H}_i in the external and internal surface respectively.

The calculation of electromagnetic parameters is analogous to the case of massif cylinder.

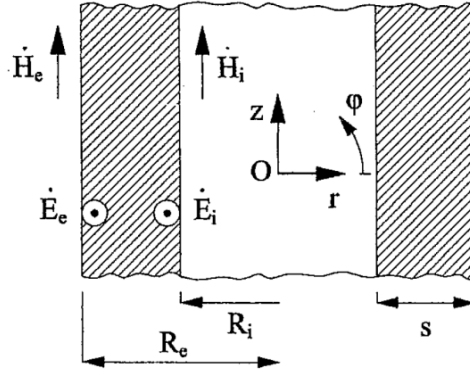


Figure 2.16. Configuration for the calculation of the electromagnetic parameters, of an hollow cylinder with a longitudinal magnetic field

Defining, in addition to those already indicated:

| | |
|-----------------|---|
| r, R_e, R_i | Generic, external and internal radius [m] |
| $s = R_e - R_i$ | Tube's thickness [m] |

$$m_r = \frac{\sqrt{2}r}{\delta} \quad m_e = \frac{\sqrt{2}R_e}{\delta} \quad m_i = \frac{\sqrt{2}R_i}{\delta} \quad \Delta m = \frac{\sqrt{2}s}{\delta}$$

Are still valid relations (2.15) and (2.16), that can be written as:

$$\frac{d^2 \bar{H}}{dr^2} + \frac{1}{r} \frac{d\bar{H}}{dr} - j \left(\frac{2}{\delta} \right)^2 \bar{H} = 0 \quad (2.15')$$

$$\bar{H} = C_1 J_0 \left(\sqrt{-j} m_r \right) + C_2 Y_0 \left(\sqrt{-j} m_r \right) \quad (2.16')$$

Imposing the boundary conditions relating to the magnetic field, follows:

$$\bar{H}_e = C_1 J_0 \left(\sqrt{-j} m_e \right) + C_2 Y_0 \left(\sqrt{-j} m_e \right)$$

$$\bar{H}_i = C_1 J_0 \left(\sqrt{-j} m_i \right) + C_2 Y_0 \left(\sqrt{-j} m_i \right)$$

Solving with Cramer's formulas:

$$C_1 = \frac{\begin{vmatrix} \bar{H}_e & Y_0 \left(\sqrt{-j} m_e \right) \\ \bar{H}_i & Y_0 \left(\sqrt{-j} m_i \right) \end{vmatrix}}{F_{00}(m_i, m_e)} = \frac{\bar{H}_e Y_0 \left(\sqrt{-j} m_i \right) - \bar{H}_i Y_0 \left(\sqrt{-j} m_e \right)}{F_{00}(m_i, m_e)}$$

$$C_2 = \frac{\begin{vmatrix} J_0 \left(\sqrt{-j} m_e \right) & \bar{H}_e \\ J_0 \left(\sqrt{-j} m_i \right) & \bar{H}_i \end{vmatrix}}{F_{00}(m_i, m_e)} = \frac{\bar{H}_e J_0 \left(\sqrt{-j} m_i \right) - \bar{H}_i J_0 \left(\sqrt{-j} m_e \right)}{F_{00}(m_i, m_e)}$$

With:

$$F_{00}(m_i, m_e) = \begin{vmatrix} J_0(\sqrt{-j}m_e) & Y_0(\sqrt{-j}m_e) \\ J_0(\sqrt{-j}m_i) & Y_0(\sqrt{-j}m_i) \end{vmatrix} = \\ = J_0(\sqrt{-j}m_e) Y_0(\sqrt{-j}m_i) - Y_0(\sqrt{-j}m_e) J_0(\sqrt{-j}m_i)$$

Using C_1 and C_2 we get:

$$\bar{H} = \bar{H}_e \frac{F_{00}(m_i, m_r)}{F_{00}(m_i, m_e)} - \bar{H}_i \frac{F_{00}(m_e, m_r)}{F_{00}(m_i, m_e)} \quad (2.38)$$

From (2.12) and (2.38), the electric field value is computed:

$$\bar{E} = -\rho \frac{d\bar{H}}{dr} = \sqrt{-2j} \frac{\rho}{\delta} \left[\bar{H}_e \frac{F_{01}(m_i, m_r)}{F_{00}(m_i, m_e)} - \bar{H}_i \frac{F_{01}(m_e, m_r)}{F_{00}(m_i, m_e)} \right] \quad (2.39)$$

We consider now a particular case of the more general one before analysed, or rather when $\bar{H}_e = 0$. This is true for each thickness of the wall, being endlessly long.

Relations (2.38) and (2.39) are abbreviated in:

$$\frac{\bar{H}}{\bar{H}_i} = -\frac{F_{00}(m_e, m_r)}{F_{00}(m_i, m_e)} = \frac{F_{00}(m_r, m_e)}{F_{00}(m_i, m_e)} = \frac{J_0(\sqrt{-j}m_e) Y_0(\sqrt{-j}m_r) - Y_0(\sqrt{-j}m_e) J_0(\sqrt{-j}m_r)}{J_0(\sqrt{-j}m_e) Y_0(\sqrt{-j}m_i) - Y_0(\sqrt{-j}m_e) J_0(\sqrt{-j}m_i)} \\ \frac{\bar{E}}{\bar{H}_i} = \sqrt{-2j} \frac{\rho}{\delta} \left[\frac{F_{01}(m_e, m_r)}{F_{00}(m_i, m_e)} \right] = \frac{J_1(\sqrt{-j}m_r) Y_0(\sqrt{-j}m_e) - Y_1(\sqrt{-j}m_r) J_0(\sqrt{-j}m_e)}{J_0(\sqrt{-j}m_e) Y_0(\sqrt{-j}m_i) - Y_0(\sqrt{-j}m_e) J_0(\sqrt{-j}m_i)} \quad (2.40)$$

Similarly to what seen in the paragraph 2.2.2, active and reactive power transmitted to the cylinder can be calculated from the coming out vector Poynting flux from surface with radius R_i .

Considering the orthogonality between \bar{E}_i and \bar{H}_i :

$$P_c + jQ_c = 2\pi R_i l \bar{E}_i \bar{H}_i = H_i^2 \frac{\rho}{\delta} \sqrt{2} (P + jQ) 2\pi R_i l \quad (2.41)$$

In Figure 2.17 are shown trends of $A_i = \sqrt{2}P$ and $B_i = \sqrt{2}Q$ depending on Δm . Curves that describe P are affected also by m_i , but only with values relatively low which do not arise in real applications. It is important to underline that being equal in Δm , increasing m_i , less active power is transferred.

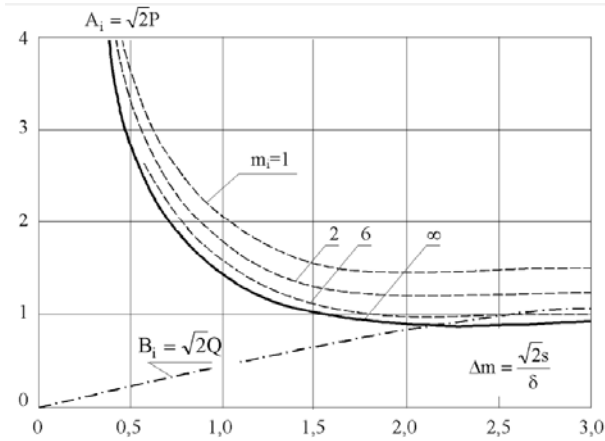


Figure 2.17. Coefficients for the calculation of the active and reactive power in a tube heated up from the inside

2.2.5 Coil's own resistance and reactance

We assume that the inducer coil, portion of an infinitely long configuration, behaves like a hollow cylinder, divided in N turns with rectangular section juxtaposed among them.

The configuration is the same one analysed in Paragraph 2.2.4, so are still valid equations (2.40) with this new meaning of the symbols:

| | |
|-------------------|---|
| $H_0 = N I / l_i$ | Intensity of applied magnetic field [A/m] |
| s | Radial thickness of the conductor constituting the coil [m] |
| R_i | Internal radius of the coil [m] ($R_e = R_i + s$) |
| ρ_i | Electrical resistivity of the material which the coil is done [Ω m] |
| δ_i | Inductor's penetration depth [m] |

$$m_r = \frac{\sqrt{2}r}{\delta_i} \quad m_i = \frac{\sqrt{2}R_i}{\delta_i} \quad m_e = \frac{\sqrt{2}R_e}{\delta_i} \quad \Delta m = m_e - m_i$$

In particular, the active and reactive power P_i and Q_i involved in the volume occupied by the inductor can be written as:

$$P_i + jQ_i = \bar{E}_i \bar{H}_0 2\pi R_i l_i = H_0^2 \frac{\rho_i}{\delta_i} (A_i + jB_i) 2\pi R_i l_i \quad (2.42)$$

Therefore, indicating:

- r_i, x_i' own resistance and internal reactance of the inducer coil [Ω]
- k_i coefficient (bigger than one) that keeps into account the air gap between turn and turn ($k_i = \frac{4l_i}{N\pi d}$ with circular section)

Considering always a series equivalent circuit, since is easier to know the current:

$$r_i = \frac{P_i}{I^2} = N^2 \rho_i \frac{2\pi R_i}{l_i \delta_i} A_i k_i = x_{i0} \frac{\delta_i}{R_i} A_i k_i \quad (2.43)$$

$$x_i = \frac{Q_i}{I^2} = N^2 \rho_i \frac{2\pi R_i}{l_i \delta_i} B_i = x_{i0} \frac{\delta_i}{R_i} B_i$$

The value of resistance is proportional to k_i , as predictable. In fact k_i is the closer to one, as much material (copper in most of the cases) is used.

A qualitative trend of A_i and B_i can be read from the Figure 2.18, from which we can deduce:

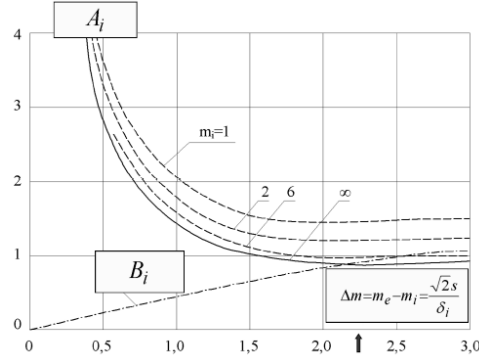


Figure 2.18. Parameters that represent active and reactive power in the coil

- with other equal conditions, looking at the trend of A_i , the losses are at minimum if $\frac{s}{\delta_i} = \frac{\pi}{2} \approx 1,57$, and they trend to a constant value, slightly higher, for bigger ratios. In every case, it is not good to go under 1 mm for reasons of mechanical seal, since inside the inductor circulates water under pressure.
- In order to reduce losses, the thickness of the coil must be chosen so that $\frac{s}{\delta_i} \geq 1,57$. It is also better to have k_i as close as possible to one;

2.2.6 Electrical efficiency

The electrical efficiency η_e can be computed as the ratio between the power turned into heat, and the active power absorbed by the inductor:

$$\eta_e = \frac{r_c' I^2}{(r_c' + r_i) I^2} = \frac{1}{1 + r_i / r_c'} = \frac{1}{1 + \frac{N^2 \rho_i \frac{2\pi R_i}{l_i \delta_i} A_i k_i}{N^2 \frac{\pi R}{\delta} \frac{\sqrt{2} \rho}{l} 2P}} = \frac{1}{1 + \frac{R_i l \delta A_i k_i}{R l_i \delta_i \sqrt{2} P}}$$

$$\eta_e = \frac{1}{1 + \alpha \frac{1}{l_i} \sqrt{\frac{\rho_i}{\rho \mu}} \frac{A_i k_i}{\sqrt{2} P}} \quad (2.44)$$

It depends on:

- Ratio α between internal diameter of the inductor and the diameter of the workpiece, and ratio among their axial lengths. The air gap should be minimum to guarantee good efficiency;

- Resistivity ρ_i of the inductor, one of the reason why copper is almost always chosen;
- Resistivity ρ and relative magnetic permeability μ of the material to heat;
- Product $A_i k_i$ typical of the inducer coil;
- Coefficient P , function of the ratio (m) between the dimension of the body to heat and the induced current.

With “well designed” inductors ($l=l_i, k_i \rightarrow 1$) and $m \rightarrow \infty$ ($P \rightarrow \frac{1}{\sqrt{2}}, A_i \rightarrow 1$), the maximum electrical efficiency that can be achieved is:

$$\eta_{eMAX} = \frac{1}{1 + \alpha \sqrt{\frac{\rho_i}{\rho \mu}}} \quad (2.45)$$

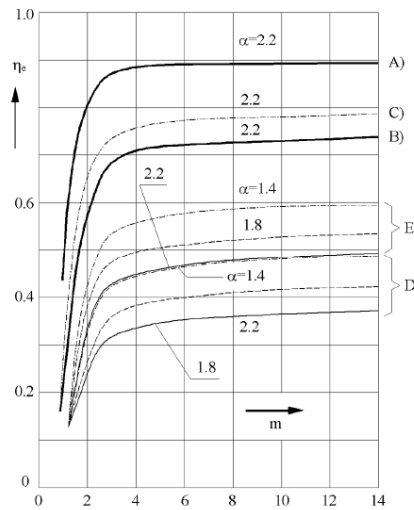


Figure 2.19. Electrical efficiency.

A) Magnetic steel heated until 800°C B) Steel from 800° to 1200° C) Steel from 0° to 1200° D) Aluminium heated to 500° and copper to 800° E) Brass heated to 800°

Curves show that with $m > 2.5$, the efficiency is almost independent on frequency, instead under 2.5, it falls to very low values. For this, never in practise m is smaller than 2.5. The efficiency is also strongly influenced by the ratio α , in particular with non magnetic material or with magnetic material beyond Curie’s point. Because of this, it is not recommended to use the same inductor to heat work pieces with such a different radius.

The efficiency reaches interesting values with carbon steel or material with high resistivity. This fact allow to use the same coil for heating workpiece with different radii. If the resistivity is low, the efficiency is always small. That’s why in the heating of aluminium two solutions are commonly adopted. The first, using alloys instead of pure material to increase resistivity; the second is to use induction heating with the piece already hot, just to adjust the temperature profile.

2.2.7 Merit and power factor

The so called “merit factor” is defined as the ratio between reactive and active power absorbed by the inductor (x'_i is neglected):

$$Q_0 = \frac{x_{i0} - \Delta x}{r_c + r_i} = \frac{x_{i0} - \Delta x}{r_c} \eta_e = \frac{x_{i0} - x_{i0} \frac{1 - \mu B}{\alpha^2}}{r_c} \eta_e = \frac{\alpha^2 - (1 - \mu B)}{\mu A} \eta_e = Q_0' \eta_e$$

Where Q_0' is the merit factor in the case of ideal inductor. Typical values are shown on Figure 2.20 in the case of non magnetic workpiece.

In a similar way, the power factor is calculated:

$$\cos \varphi = \frac{r_c + r_i}{\sqrt{(r_c + r_i)^2 + (x_{i0} - \Delta x)^2}} = \frac{1}{\sqrt{1 + (Q_0' \eta_e)^2}} = \frac{1}{\sqrt{1 + \left(\frac{\alpha^2 - (1 - \mu B)}{\mu A} \eta_e\right)^2}} \quad (2.46)$$

In Fig. 2.20 are shown $\cos \varphi$ trends with ideal inductor and non magnetic load. The power factor is always very, typically between 0.1 and 0.3; this one makes necessary the compensation with capacitors.

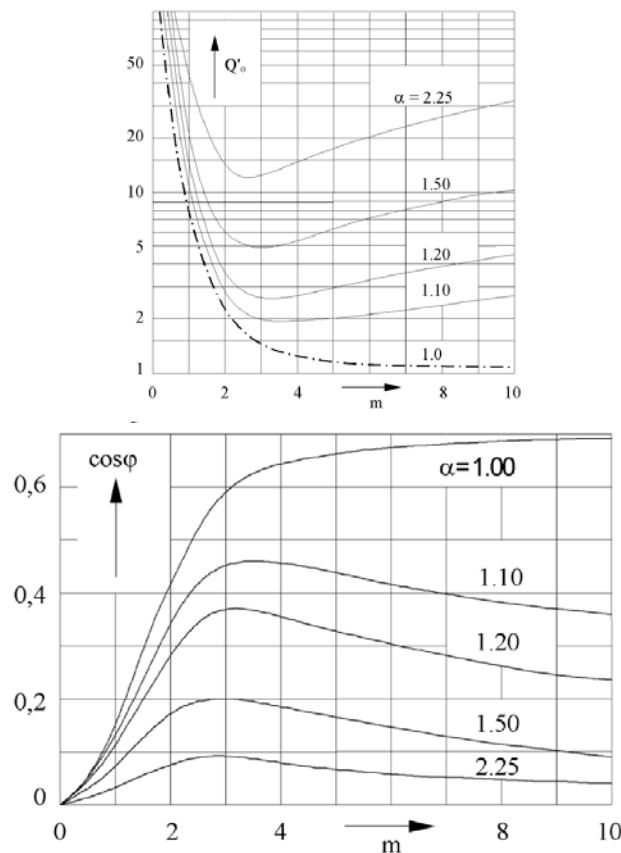


Figure 2.20 Merit and power factor with different values of 'm'

2.2.8 Thermal transient in a cylindrical body

Induction heating processes are widespread in the industrial manufacturing and processing and two main types can be recognized:

- **Differentiated heating**, like that used in hardening processes, where there are different temperatures along the section;
- **Uniform heating**, with temperatures as similar as possible along the radius. Often it precedes hot working processes of the material.

In both cases, from what we have seen in the previous paragraphs, induction heating is such that heating is non uniform in the section. As usual, the cylinder's length is much higher compared to the diameter, and for this the heat's transmission occurs only in the radial direction. At last, thermal parameters that define the cylinder are considered constant.

Starting from Fourier's equation:

$$\frac{\partial \vartheta}{\partial t} = \frac{\lambda}{c \gamma} \nabla^2 \vartheta + \frac{w}{c \gamma} \quad (2.47)$$

With:

| | |
|-----------|--|
| θ | Temperature [$^{\circ}\text{C}$] in an generic radius at a certain instant of time |
| λ | Thermal conductivity [W/m K] |
| c | Specific heat [J/kg K] |
| γ | Density [kg/m^3] |
| w | Specific power [W/m^3] turned into heat in the workpiece |

Recalling the expression of the laplacian in cylindrical coordinates:

$$\nabla^2 \vartheta = \frac{1}{r} \frac{\partial}{\partial r} \left(r \frac{\partial \vartheta}{\partial r} \right) + \frac{1}{r^2} \frac{\partial^2 \vartheta}{\partial \varphi^2} + \frac{\partial^2 \vartheta}{\partial z^2} \quad (2.48)$$

From the hypothesis mentioned before, the last two terms are null. Applying besides the product rule we obtain:

$$\nabla^2 \vartheta = \frac{\partial^2 \vartheta}{\partial r^2} + \frac{1}{r} \frac{\partial \vartheta}{\partial r} \quad (2.48')$$

Defining, as last, thermal diffusivity of the material $k = \lambda / c \gamma$ [m^2/s], (2.47) becomes:

$$\frac{\partial \vartheta}{\partial t} = k \left(\frac{\partial^2 \vartheta}{\partial r^2} + \frac{1}{r} \frac{\partial \vartheta}{\partial r} \right) + \frac{w(r)}{c \gamma} \quad (2.47')$$

With the hypothesis that the initial temperature of the cylinder is zero (assumption that simplifies the solution) and the heating occurs in adiabatic conditions (no thermal losses):

$$\vartheta(r) = 0, \text{ if } t = 0$$

$$\frac{\partial \vartheta}{\partial r} = 0, \text{ if } t > 0 \text{ and } r = R$$

In order to generalize the result some non dimensional parameters are defined:

| | |
|-------------------------------------|--------------------------|
| $\xi = r / R$ | Adimensional radius |
| $\tau = k t / R^2$ | Adimensional time |
| $\Theta = 2\pi\lambda \theta / P_u$ | Adimensional temperature |

When P_u is the power transformed in heat per unit of axial length [W/m]:

$$P_u = \int_0^R 2\pi r w(r) dr = 2\pi R^2 \int_0^1 \xi w(\xi) d\xi$$

Rewriting Fourier's equation and initial conditions with new variables:

$$\frac{\partial \Theta}{\partial \tau} = \frac{\partial^2 \Theta}{\partial \xi^2} + \frac{1}{\xi} \frac{\partial \Theta}{\partial \xi} + \Psi(\xi) \quad (2.47'')$$

$$\Theta(\xi) = 0, \text{ if } \tau = 0$$

$$\frac{\partial \Theta}{\partial \xi} = 0, \text{ if } \tau > 0 \text{ and } \xi = 1$$

Having defined $\Psi(\xi)$ as: $\Psi(\xi) = \frac{2\pi R^2}{P_u} w(r) = \frac{w(\xi)}{\int_0^1 \xi w(\xi) d\xi}$

Remembering (2.25), as shown before:

$$\left| \frac{w}{w_0} \right| = \left| \frac{J_1(\sqrt{-jm\xi})}{J_1(\sqrt{-jm})} \right|^2 = \frac{\text{ber}^2(m\xi) + \text{bei}^2(m\xi)}{\text{ber}^2(m) + \text{bei}^2(m)}$$

Therefore:

$$\Psi(\xi) = m \frac{\text{ber}^2(m\xi) + \text{bei}^2(m\xi)}{\text{ber}(m)\text{ber}'(m) + \text{bei}(m)\text{bei}'(m)} \quad (2.48)$$

The solution of the equation (2.47'') is known with these boundary conditions, and is defined by an infinite series of terms, calculated from Laplace's transformation. Keeping into account the complexity that arises due to the parameters' variation during the heating, the hypothesis of constant $\Psi(\xi)$ is coarse. It is better, for different kinds of heating, refer to simpler solutions.

A qualitative trend can be obtain through simplify expressions of the ratio $\frac{w}{w_0}$. For heating processes with a final distribution relatively uniform of the temperature along the radius, this occurs in the "linear" growth of temperature (for different "r"), after a first exponential rise. A temperature's linear increase in every point of the cylinder happens when the power necessary to increase the temperature of a generic cylinder with radius r and unitary length with constant speed ($\frac{\partial \theta}{\partial t}$) is equal to the power transmitted through the lateral surface and that turned into heat inside the cylinder. Analytically:

$$\pi r^2 c \gamma \frac{\partial \theta}{\partial t} = 2\pi r \lambda \frac{\partial \theta}{\partial r} + \int_0^r 2\pi r w(r) dr \quad (2.49)$$

Introducing the no-dimensional parameters:

$$\frac{\partial \Theta}{\partial \tau} = \frac{4\pi R^2}{P_u \xi^2} \int_0^\xi \xi w(\xi) d\xi + \frac{2}{\xi} \frac{\partial \Theta}{\partial \xi} \quad (2.49')$$

The constant speed of the increase of the temperature can be computed considering the total power P_u turned into heat in a cylinder with radius R and unitary length:

$$P_u = \pi r^2 c \gamma \frac{\partial \theta}{\partial t} \quad (2.50)$$

Introducing the no-dimensional parameters in (2.50):

$$\frac{\partial \Theta}{\partial \tau} = 2$$

From the equality of (2.48) and (2.49):

$$\frac{\partial \Theta}{\partial \xi} = \xi \frac{1}{\xi} \frac{\int_0^\xi \xi w(\xi) d\xi}{\int_0^1 \xi w(\xi) d\xi} \quad (2.51)$$

This relation does not depend on τ , and permits to know the distribution of Θ as a function of ξ in every part of the linear increase of temperature.

Substituting (2.48) in (2.51) and calculating integrals, we get:

$$\frac{\partial \Theta}{\partial \xi} = \xi - \frac{\text{ber}(m\xi)\text{ber}'(m\xi) + \text{bei}(m\xi)\text{bei}'(m\xi)}{\text{ber}(m)\text{ber}'(m) + \text{bei}(m)\text{bei}'(m)}$$

Integrating once again:

$$\Theta = \frac{1}{2} \xi^2 - \frac{\text{ber}^2(m\xi) + \text{bei}^2(m\xi)}{2m[\text{ber}(m)\text{ber}'(m) + \text{bei}(m)\text{bei}'(m)]} + C$$

If we call Θ_a the value of Θ at the axis of the cylinder, we know how much is it the integration constant:

$$\Theta = \Theta_a \text{ if } \xi = 0$$

$$\Theta = \Theta_a + \frac{1}{2} \left\{ \xi^2 - \frac{\text{ber}^2(m\xi) + \text{bei}^2(m\xi) - 1}{m[\text{ber}(m)\text{ber}'(m) + \text{bei}(m)\text{bei}'(m)]} \right\} \quad (2.52)$$

With $m \rightarrow \infty$, the distribution is parabolic:

$$\Theta - \Theta_a = \frac{1}{2} \xi^2$$

In particular, the difference of temperature between edge and centre is $\Theta_s - \Theta_a = \frac{1}{2}$.

In Fig. 2.21 the distribution of the temperature, varying the radius, with different “m” is shown.

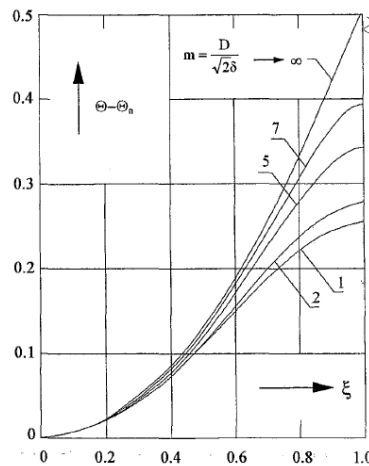


Figure 2.21 Difference of temperature with the axis, changing ‘m’

For lower values of “m” that difference, considering the same power transformed into heat inside the cylinder, values always than what was calculated before (with $\xi=1$).

$$\text{So that } \Theta_s - \Theta_a = \frac{1}{2} F(m)$$

$$\text{With } F(m) = 1 - \frac{\text{ber}^2(m) + \text{bei}^2(m) - 1}{m(\text{ber}(m)\text{ber}'(m) + \text{bei}(m)\text{bei}'(m))} \quad (2.53)$$

$F(m)$ could be considered as a correction factor to the superficial heating, that keeps into account that in an induction heating process the power is transformed into heat inside the cylinder.

For the purposes of the heating times it is better to refer to the average temperature in the workpiece.

$$\Theta_m = \frac{2\pi\lambda}{P_u} \theta_m = 2 \int_0^1 \Theta \xi d\xi$$

$$\Theta_m = \Theta_a + F'(m)$$

$$\text{Where } F'(m) = \frac{1}{4} - \frac{\text{ber}(m) \text{bei}'(m) + \text{bei}(m) \text{ber}'(m) - m/2}{m^2 (\text{ber}(m) \text{ber}'(m) + \text{bei}(m) \text{bei}'(m))}$$

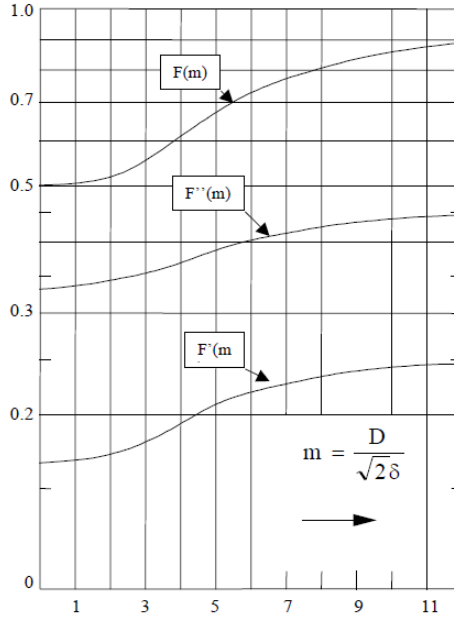


Figure 2.22 Values of a) $F(m)$ b) $F'(m)$ c) $F''(m)$

From (2.50) we get $\Theta_m = 2\tau$, and (2.52) becomes:

$$\Theta = 2\tau - F'(m) + \frac{1}{2} \left[\xi^2 - \frac{\text{ber}^2(m\xi) + \text{bei}^2(m\xi) - 1}{m (\text{ber}(m\xi) \text{ber}'(m\xi) + \text{bei}(m\xi) \text{bei}'(m\xi))} \right] \quad (2.54)$$

$$\Theta_s = 2\tau - F'(m) + \frac{1}{2} F(m)$$

This relation is used in the case of uniform heating for the calculus of the heating time and of the power, which is necessary to bring the cylinder at a certain final temperature with a predetermined difference between the latter and that on the axis.

Indicated with $\varepsilon = \frac{\theta_s - \theta_a}{\theta_s}$ the relative difference of temperature:

$$\tau = \frac{F(m)}{4\varepsilon} [1 - \varepsilon F''(m)] \quad \text{with } F''(m) = 1 - 2 \frac{F'(m)}{F(m)} \quad (2.55)$$

As last:

$$\left. \begin{aligned} t &= R^2 \frac{F(m)}{4k\varepsilon} [1 - \varepsilon F''(m)] = R^2 \frac{\pi c \gamma}{P_u} \theta_s [1 - \varepsilon F''(m)] \\ P_u &= \frac{4\pi\lambda}{F(m)} (\theta_s - \theta_a) = 4\pi\lambda \frac{\varepsilon}{F(m)} \theta_s \end{aligned} \right\} \quad (2.56)$$

The previous relations and $F''(m)$ show that when ε is quite small (0.05 – 0.10), the term $\varepsilon F''(m)$ is negligible. It takes into account that the evaluation of the temperature is made on the surface and not to the average of the cylinder.

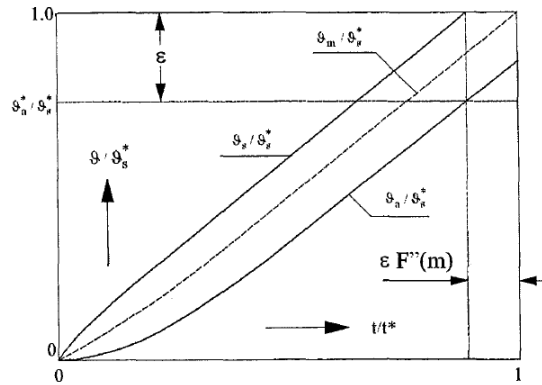


Figure 2.23 Thermal transient in a uniform heating of no magnetic load, without superficial losses

From the (2.56) relations we can deduce that:

- Increasing the frequency means to increase $F(m)$ and, as a consequence, to parity with other conditions, to reduce the specific power P_u and increase the heating time;
- Imposing low values of ϵ means, with fixed frequency, to reduce P_u and to reach the same final temperature in a longer time;
- Assigned θ_s and the heating time (dependent on the hourly production), is fixed the specific power. In this case the only element in which it is possible to act for reducing ϵ is the frequency whereby changes “m” and $F(m)$;
- Alternatively, given values of ϵ and θ_s , it is possible to increase P_u and decrease the heating time only by reducing $F(m)$, changing the frequency.

The superficial losses have been neglected. From one side they reduce the heating - power and thus increase the heating time. In these conditions an accurate heating time calculation could be done referring to the “useful power” P_u^* .

$$t = R^2 \frac{\pi c \gamma}{P_u^*} \theta_s [1 - \epsilon F''(m)] \quad (2.57)$$

$$\theta_s - \theta_a = \frac{P_u^*}{4\pi\lambda} F^*(m) \quad \text{Where } P_u^* = P_u - 2\pi R p_i$$

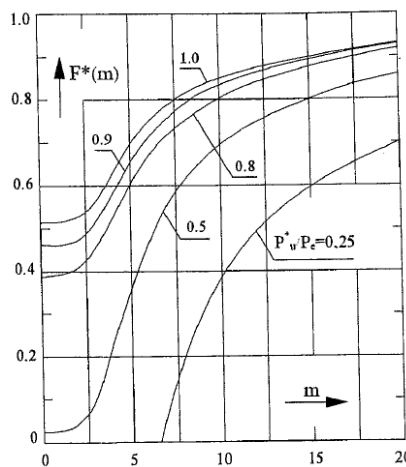


Figure 2.24 Correction factor for the surface's losses

2.2.9 Variations in the characteristics of the material

All the relations analysed in the previous paragraphs are developed with the simplifying hypothesis that the characteristic parameters (like electrical resistivity, heat capacity...) and the heat exchange conditions remain constant during the heating. In reality, it is always remarkable that the influence of the properties is changing. In particular in magnetic steels, in additions to the variations above, plays an important role also those of magnetic permeability with temperature and magnetic field.

It is acceptable the hypothesis of constant material properties only for relatively limited temperature ranges, inside of which it is usually taken as a constant quantity, an appropriate weighted average value of the selected variable.

Let us examine, with a qualitative approach, some consequences of the variations mentioned before in a thermal transitory in which an increase of temperature from θ' to θ'' occurs. We neglect also the non-uniformity of the temperature in the piece. We denote with (') and ('') the corresponding parameter values.

From the equations introduced before:

- The penetration depth is modified in the ratio $\frac{\delta''}{\delta'} = \sqrt{\frac{\rho'' \mu'}{\rho' \mu''}}$
- The value "m" changes $\frac{m''}{m'} = \frac{\delta'}{\delta''} = \sqrt{\frac{\rho' \mu''}{\rho'' \mu'}}$
- The eddy currents modify their distribution as shown in Fig. 2.11
- The current density G_0 changes, with constant field, in the ratio

$$\frac{G_0''}{G_0'} = \frac{m''}{m'} \sqrt{\frac{(P^2+Q^2)''}{(P^2+Q^2)'}}$$

- The specific power per unit volume is so modified

$$\frac{w_0''}{w_0'} = \frac{\rho''}{\rho'} \left(\frac{G_0''}{G_0'} \right)^2 = \frac{\rho''}{\rho'} \left(\frac{m''}{m'} \right)^2 \frac{(P^2+Q^2)''}{(P^2+Q^2)'}$$

- The active power in the cylinder P_c , with constant field, changes with a ratio

$$\frac{P_c''}{P_c'} = \frac{A(m'')}{A(m')} = \frac{\rho'' m' P(m'')}{\rho' m'' P(m')}$$

Non magnetic materials

Typically the variation of the resistivity with the temperature is $\rho(\theta) = \rho_0(1 + \alpha_0\theta)$. During the heating time:

- The penetration depth increases;
- "m" diminishes;
- The eddy currents and the sources of heat penetrate deeper during the heating;
- G_0 decreases;
- The active power, with fixed magnetic field, changes varying "m" with a consequent increase of P_c with the temperature.

Magnetic materials

In these materials (steel, iron, nickel), in addition to the variations of resistivity with temperature, magnetic permeability values are strongly dependent on magnetic field and temperature.

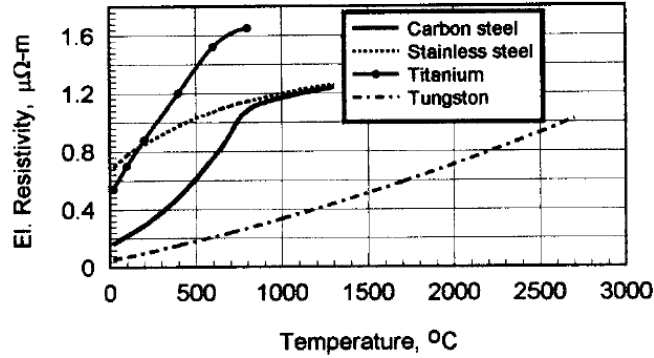


Figure 2.25 How resistivity changes in different materials

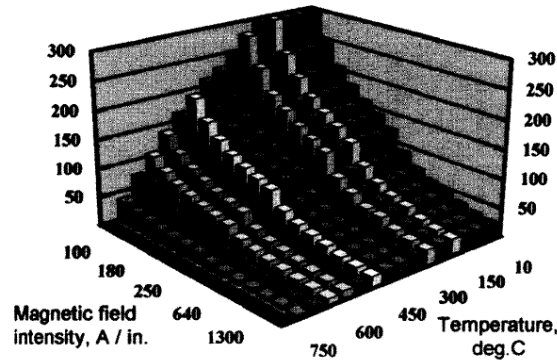


Figure 2.26 Dependency of the relative magnetic permeability on temperature and magnetic field

In carbon steels resistivity changes in a nonlinear way: it grows five times in the range between 0 and 800°C, while at higher temperature the increase is slower, reaching at 1200 – 1300 °C a value seven times bigger than the value at room temperature. Values of permeability at 20 °C change, as well as the magnetic field intensity, with the carbon content inside the steel. If the magnetic field is relatively intense, neglecting the variation of μ along the radius, the relative magnetic permeability is estimable as:

$$\mu = 1 + \frac{B_s}{H_0} \approx 1 + \frac{14000 \div 16000}{H_0} \quad (2.58)$$

Where B_s is the value of induction at saturation [Gauss] and H_0 the superficial magnetic field intensity [A/cm].

As already mentioned, the magnetic permeability does not change so much with temperature until 500 – 600 °C, while decreases rapidly up to reach the unit value at the “Curie point” (at 750 – 780 °C). As a consequence, the heating process above the Curie point can be described very coarsely with two different conditions characterized by constant parameters: one until 750°C with $\rho_A = 50 \div 60 \cdot 10^{-8}$ [ohm cm], another where

$\mu_B=1$ and resistivity $\rho_B=100\div115 \cdot 10^{-8}$ [ohm cm]. With these values, depending on magnetic field H_0 :

$$\frac{m_B}{m_A} = \sqrt{\frac{f_B}{f_A}} \sqrt{\frac{\rho_A}{\rho_B \mu_A}} = \frac{1}{20} \div \frac{1}{10} \quad (2.59)$$

And then: $m_A \geq (10\div20) 2.5 = 25 \div 50$

$$\frac{P_{uB}}{P_{uA}} \cong \left(\frac{H_{0B}}{H_{0A}}\right)^2 \sqrt{\frac{f_B}{f_A}} \sqrt{\frac{\rho_A}{\rho_B \mu_A}} \frac{P_B}{P_A} \frac{1}{1.37}$$

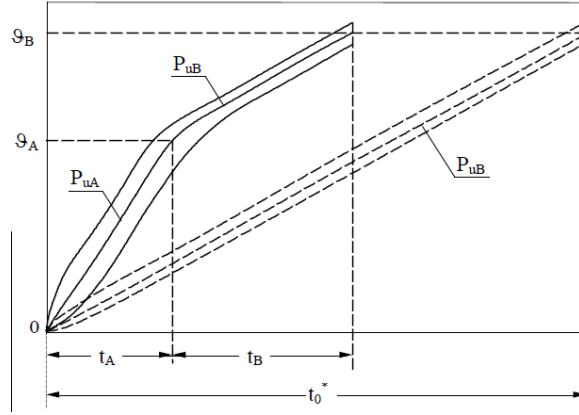


Figure 2.27 How to evaluate the thermal transient for carbon steels

$$t_0 = t_A + t_B \approx \pi R^2 \left[\frac{c_A \theta_A}{P_{uA}} + \frac{c_B (\theta_B - \theta_A)}{P_{uB}} \right] \quad (2.60)$$

Considering the average integrated values of c_A and c_B , the calculation of t_0 can be done considering an ideal heating with constant power P_{uB} and the material properties of the steel above Curie point. Indicated with t_0^* the length of this ideal transient:

$$\frac{t_0}{t_0^*} = \frac{t_A + t_B}{t_0^*} \approx \frac{\left[\frac{c_A \theta_A}{P_{uA}} + \frac{c_B (\theta_B - \theta_A)}{P_{uB}} \right]}{\frac{c_B \theta_B}{P_{uB}}} \approx \frac{\theta_A \frac{P_{uB}}{P_{uA}} + (\theta_B - \theta_A)}{\theta_B}$$

$$\frac{t_A}{t_B} \approx \frac{\theta_A}{\theta_B - \theta_A} \frac{P_{uB}}{P_{uA}}$$

With typical values of μ_A , supposing that m_B reaches $2.2 \div 2.5$ and introducing integrated average values of $\rho_A \rho_B$ we get:

$$\frac{P_{uB}}{P_{uA}} \approx 0.15 \div 0.20; \quad \frac{t_A}{t_B} \approx 0.20 \div 0.36; \quad \frac{t_0}{t_0^*} \approx 0.47 \div 0.53$$

For inductors with uniform distributed Ampere – turns, it follows:

- Under Curie “m” is usually bigger than 25;
- The power over Curie point is much lower than that one induced at the beginning;
- A rough estimate of the heating time can be obtained referring to the 50% of the time of an ideal heating with constant P_{uB} .

In reality “m” is not constant along the radius. It diminishes progressively from an high initial value (with eddy currents and power distributions limited in a very thin superficial

layer) to lower one, in correspondence of which the currents and power distributions penetrate more depth.

The Fig. 2.28 shows the dependency of the active power transferred to the workpiece, with constant magnetic field, function of temperature.

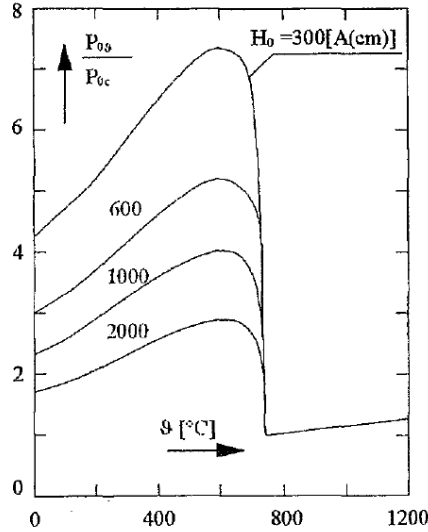


Figure 2.28 Variation of the specific power in the case of carbon steel

In the initial portion the specific power grows because of the increase of the resistivity, instead the permeability remains almost unchanged until 550 – 600 °C. Then it dramatically falls since the diminishing of the permeability prevails on the growth of the resistivity.

As mentioned before, “m” is not uniform along the radius, not only for the dependency with the temperature, but also with magnetic field. Some analytical nonlinear theories lead to the conclusion that with a variable μ , function of the local magnetic field, the active power is approximately 1.37 bigger of that one computable with a constant value of μ calculated at the surface. The reactive power instead, doesn’t change. Also the current density and the power distributions are modified: the electromagnetic wave penetrates to lower depth as effect of the increase of the magnetic permeability.

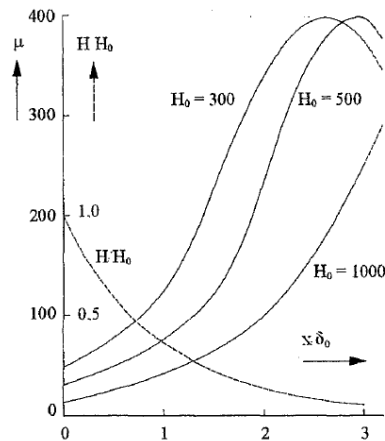


Figure 2.29 Distribution of the permeability in a ferromagnetic piece

A second phenomena that modifies the theoretical distribution of currents and of the power as well, is due to the fact that in correspondence of the Curie point, the superficial layer is hotter and nonmagnetic, but the underlying layers are still magnetic. The eddy currents distribution can be summarized with two exponentials (see Fig. 2.30). It can happen that the maximum value of current density is reached inside the billet and not in the surface.

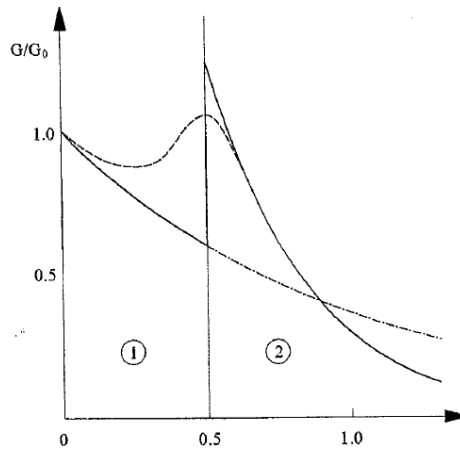


Figure 2.30 Qualitative distribution of the current density in the magnetic [2] and nonmagnetic [1] layer at exceeding of the Curie point.

3. Numerical models

This chapter starts with a short explanation about what a finite element analysis is. It follows the structure model and simulation results.

3.1 Finite Element Analysis

In the solution of complex engineering problems, application of conventional analytical methods maybe impossible or impractical. Analysis and design of electrical equipment is a difficult task due to several aspects like complex geometry, non-linear characteristics of materials, presence of thermal and mechanical aspects, dynamical phenomena. The first step of analysis is the selection of which aspects are considered and which not. This step is named *modelling*. An example can be the choice between static and dynamic analysis. The second step is the selection of a numerical method to solve the problem, i.e. a system of ordinary and partial differential equations (PDE). This problem is called *discretisation*. In this thesis we're referring only to a FEMethod, one of the most common. The third and final step, is computation of additional results and analysis of the *solution*. If the results are not those satisfying, the analysis must be repeated with different parameters.

3.1.1 Electromagnetic and thermal analysis

In general, there are two classes of electromagnetic fields that can be described: time independent static and time varying. Moreover we have to distinguish between slow and fast varying in time of quantities. The purpose of this paragraph is present briefly the typology of PDEs which must be solved in electromagnetic and thermal problems.

Low frequency – quasi stationary fields

Most of electrical engineering issues can be described by quasi static phenomena [10]. Slow varying and periodic fields up to 10 kHz are considered to be quasi stationary. In this hypothesis the displacement current is negligible. Deciding whether the displacement current can be neglected or not, depends of the wavelength on the problem considered in the frequency domain. If it is large compared to the physical dimensions of the problem, the displacement current is negligible.

Recalling Maxwell's equations already introduced in chapter 2 and the constitutional relations:

$$\nabla \times \mathbf{H} = \mathbf{G} + \frac{\partial \mathbf{D}}{\partial t} \quad (3.1)$$

$$\nabla \times \mathbf{E} = - \frac{\partial \mathbf{B}}{\partial t} \quad (3.2)$$

$$\nabla \cdot \mathbf{B} = 0 \quad (3.3)$$

$$\mathbf{B} = \mu \mu_0 \mathbf{H} \quad (3.4)$$

$$\mathbf{D} = \varepsilon \varepsilon_0 \mathbf{E} \quad (3.5)$$

$$\mathbf{G} = \sigma \mathbf{E} \quad (3.6)$$

Where μ is the relative magnetic permeability, ε the relative electrical permeability and σ is the electrical conductivity [S/m]. In Ampere's Law (3.1) is null the displacement current's term ($\partial \mathbf{D} / \partial t$).

From the definition of the magnetic vector potential $\mathbf{B} = \nabla \times \mathbf{A}$, Faraday's law (3.2) becomes:

$$\nabla \times \mathbf{E} = - \frac{\partial}{\partial t} \nabla \times \mathbf{A} \quad (3.2')$$

Now employing Ohm's law to calculate the eddy currents \mathbf{G}_e yields:

$$\mathbf{G}_e = \sigma \mathbf{E} = - \sigma \frac{\partial \mathbf{A}}{\partial t} \quad (3.7)$$

Ampere's law can be rewritten, yielding the A formulation, for the quasi stationary magnetic field in time domain.

$$\nabla \times \left(\frac{1}{\mu \mu_0} \nabla \times \mathbf{A} \right) + \sigma \frac{\partial \mathbf{A}}{\partial t} = \mathbf{G} \quad (3.1')$$

$$\frac{1}{\mu \mu_0} (-\nabla^2 \mathbf{A} + \nabla (\nabla \cdot \mathbf{A})) + \sigma \frac{\partial \mathbf{A}}{\partial t} = \mathbf{G} \quad (3.1'')$$

Considering Coulomb gauge condition $\nabla \cdot \mathbf{A} = 0$

$$\nabla^2 \mathbf{A} - \mu \mu_0 \sigma \frac{\partial \mathbf{A}}{\partial t} = - \mu \mu_0 \mathbf{G} \quad (3.1''')$$

Obtaining thus an equation that is only function of the magnetic vector potential. Assuming now a sinusoidal excitation current, with an angular frequency ω [rad/s], Ampere's equations becomes:

$$\frac{\partial \mathbf{A}}{\partial t} = j\omega \mathbf{A}$$

$$\nabla^2 \mathbf{A} - j\omega \mu \mu_0 \sigma \mathbf{A} = - \mu \mu_0 \mathbf{G}$$

Magnetodynamic field (waves)

In the most general case, when the displacement current is not negligible:

$$\nabla \times \mathbf{H} = \mathbf{G} + \frac{\partial \mathbf{D}}{\partial t} \quad (3.1^*)$$

Introducing also Gauss' law:

$$\nabla \cdot \mathbf{D} = \rho \quad (3.8)$$

Where ρ is the volumetric charge density [C/m³].

Substituting the definition of magnetic vector potential, already mentioned above, in (3.1*):

$$\begin{aligned}\nabla \times \nabla \times \mathbf{A} &= \mu \mu_0 \mathbf{G} + \mu \mu_0 \varepsilon \varepsilon_0 \frac{\partial \mathbf{D}}{\partial t} \\ \nabla (\nabla \cdot \mathbf{A}) - \nabla^2 \mathbf{A} &= \mu \mu_0 \mathbf{G} + \mu \mu_0 \varepsilon \varepsilon_0 \frac{\partial \mathbf{D}}{\partial t}\end{aligned}\quad (3.1^{**})$$

From Faraday Lenz's law (3.2), considering $\mathbf{B} = \nabla \times \mathbf{A}$:

$$\begin{aligned}\nabla \times \mathbf{E} &= - \frac{\partial}{\partial t} \nabla \times \mathbf{A} \\ \nabla \times (\mathbf{E} + \frac{\partial \mathbf{A}}{\partial t}) &= 0\end{aligned}$$

Since the expression in parentheses is irrotational, it can be written as the gradient of a scalar function, the scalar potential V .

$$\mathbf{E} + \frac{\partial \mathbf{A}}{\partial t} = - \nabla V \quad (3.9)$$

Using (3.5) and (3.9) inside (3.1**):

$$\nabla (\nabla \cdot \mathbf{A}) - \nabla^2 \mathbf{A} = \mu \mu_0 \mathbf{G} - \mu \mu_0 \varepsilon \varepsilon_0 \nabla \frac{\partial V}{\partial t} - \mu \mu_0 \varepsilon \varepsilon_0 \frac{\partial^2 \mathbf{A}}{\partial t^2} \quad (3.1^{***})$$

Assuming Lorenz condition $\nabla \cdot \mathbf{A} = - \mu \mu_0 \varepsilon \varepsilon_0 \frac{\partial V}{\partial t}$

$$\nabla^2 \mathbf{A} - \mu \mu_0 \varepsilon \varepsilon_0 \frac{\partial^2 \mathbf{A}}{\partial t^2} = - \mu \mu_0 \mathbf{G} \quad (3.10)$$

Considering now Gauss' law (3.8) and substituting (3.5) and (3.9) in it:

$$\nabla^2 V - \mu \mu_0 \varepsilon \varepsilon_0 \frac{\partial^2 V}{\partial t^2} = - \frac{\rho}{\varepsilon \varepsilon_0} \quad (3.11)$$

Equations (3.10) and (3.11) are named non homogeneous wave equations. In addition to Lorenz condition they are equivalent to the four Maxwell equations. They are valid anywhere. On the left side appears one unknown function with μ and ε as known parameters. On the right side the known source.

Thermal problems

There are several sources of heat, such as Joule heat and magnetic hysteresis. The three heat transfer principles are briefly presented as follows.

Conduction is a process where the heat is transmitted inside a body between different bodies having physical contact. Fourier's equation describes this phenomenon:

$$c \frac{\partial T}{\partial t} + \nabla \cdot (-\lambda \nabla T) = Q \quad (3.12)$$

| | |
|-----------|---|
| T | Temperature [K] |
| c | Thermal capability [J/ m ³ K] |
| λ | Thermal conductivity [W/m K] |
| Q | Thermal source volumetric density [W/m ³] |

Since λ is assumed constant, (3.12) can be written as:

$$\nabla^2 T - \frac{c}{\lambda} \frac{\partial T}{\partial t} = - \frac{Q}{\lambda} \quad (3.12')$$

This is very similar to (3.10) and can be solved in a similar way.

For instance, Q can be written as the joule's effect source by: $Q = \frac{J^2}{\sigma}$

Convection occurs when a fluid has a contact with a heated solid body. There will be a constant movement where the hotter particles of the fluid will rise up due to their lower density and will be replaced by the cooler ones due to their higher density. The other convective process is called forced convection. In this case the circulating process is not driven by the difference of density of the particular sections of the fluid, but the convection is driven by e.g. a fan or a pump. Heat is transmitted from the body to the fluid according to:

$$\lambda \frac{dT}{ds} n = -h (T - T_a) \quad (3.13)$$

| | |
|----------------|--|
| h | Coefficient of transfer by convection [W/m ² K] |
| T | Temperature of the heated element [K] |
| T _a | Temperature of the fluid far from the element [K] |

Every element with a temperature higher than zero K emits radiation through electromagnetic waves. This phenomenon is named *radiation*. A body at temperature T radiates energy to another body at temperature T_a, according to the following expression:

$$\lambda \frac{dT}{ds} n = -\varepsilon \gamma (T^4 - T_a^4)$$

| | |
|---|---|
| ε | Emissivity of the body |
| γ | Stefan Boltzmann constant [W/ m ² K ⁴] |

In general these three heat transfer phenomena act combined in a heating setup. Except the situation takes place in vacuum, where just radiation is acting.

3.1.2 PDE's solution

Frequently a direct solution of PDE is possible only for simple cases or under restrictive assumption. For the solution of detailed and realistic models, numerical methods are often the only practicable alternative. The main objective of a numerical model is to solve a PDEs on a discrete set of points of the solution domain. In order to do so, the solution domain is divided into subdomains, having the discretization points as vertices. The distance between two adjacent vertices is the mesh size. Time is also subdivided into discrete intervals, and we call time step the interval between two consecutive times at which the solution is obtained. The PDE is approximated, or discretized, to obtain a system of algebraic equations, where the unknown are the solution values at the discretization points. The system of algebraic equations can be solved with iterative techniques. After the discretization, it is necessary to check if the approximation is appropriate. For a successful solution, the numerical scheme must be stable, convergent and consistent. The scheme is stable if the solution stays bounded during the solution procedure. It's convergent if the numerical solution tends to the real solution as the mesh size and the time – step tends to zero. The scheme is consistent if the truncation error (error introduced by the finite approximation of derivatives) tends to zero as well.

If we indicate with Φ the unknown PDE's function, not only it must fulfil the solution in the region R – the calculation domain, but also it must satisfy certain conditions on S , the boundary on R . The choice of the boundary conditions has an influences in the final solution.

The boundary conditions that can be imposed can be of three kinds:

- *Dirichlet* condition: it's assigned by fixing a determined value of the potential on a given boundary curve. In this way, the curve is characterized by a constant value of potential; thus the equipotential lines result tangential to such a boundary.

$$\Phi(r) = f(r) \quad r \text{ on } S$$

- *Neumann* condition: the condition is assigned by fixing the normal derivative of the potential on a given boundary curve. In other words, the line crosses the boundary in a known way.

$$\frac{\partial \Phi(r)}{\partial n} = g(r) \quad r \text{ on } S$$

- *Mixed* boundary conditions, combining the two previous cases.

The possibility, thanks to the finite element method, to solve PDE can be seen as coming from two different approaches: one is called “Variational approach” and the other “Weighted residual approach”. By applying them to a PDE system, they give the same set of equations to solve. But, in the Variational approach, is required a function to be minimized, typically the energy of the system. The weighted residual approach starts instead from the differential equations of the system, that in a general case we can write as:

$$L(\Phi) - f = 0 \quad (3.14)$$

Where L is a linear operator (for example ∇^2), f is a known function (typically the source, referring to (3.10) and (3.11)), and Φ the unknown function. The exact solution of the problem can be approximated by assuming that it varies according to a set of known functions, each of them multiplied by an unknown coefficient.

$$\Phi_n = \varphi_0 + \sum_{j=1}^n a_j \varphi_j \quad (3.15)$$

These approximate function coefficients, can be determined by solving a system of equations as it will be explained later. Function φ_0 is usually specified in order to satisfy Dirichlet boundary condition.

If we introduce the so called residual R_n :

$$L(\Phi_n) - f = R_n \quad (3.16)$$

The residual function R varies in the domain Ω . The coefficients a_j are evaluated by orthogonalization of residual R_n to a certain set of n weighting functions w_i , i.e., by zeroing the inner product:

$$\langle R_n, w_i \rangle = \int_{\Omega} R_n w_i d\Omega = 0 \quad i = 1, 2, \dots, n \quad (3.17)$$

A possible choice is $w_i = \varphi_i$ i.e. weighting function is the same of approximating function. It is named Galerkin method.

Substituting (3.15) and (3.16) in (3.17), a set of n simultaneous linear algebraic equations that can be solved taking into account boundary conditions is obtained.

3.2 Ansys mechanical Apdl

The software used to carry out the analysis is ANSYS© Mechanical APDL. It permits not only to perform structural analysis or solve mechanical issues in general, but also it allows thermo – structural and electro – thermal tasks.

The highlights of the developed script are shown in Figure 3.1, making use of a flux diagram.

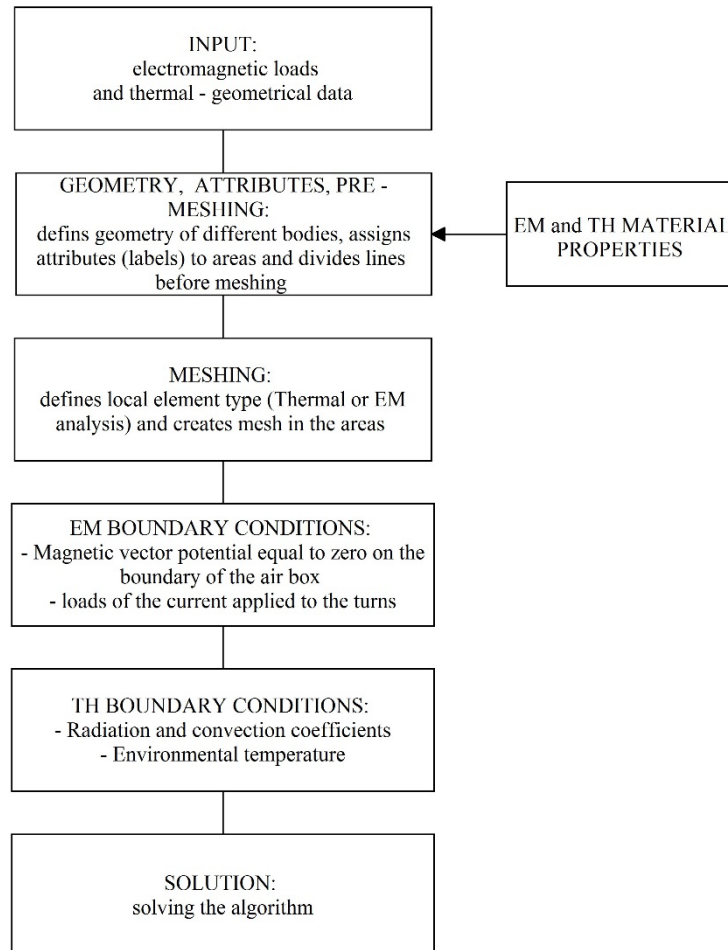


Figure 3.1. Flux diagram of pre-processing

The model in analysis is considered to be axisymmetric, i.e. every phenomenon is supposed to be identical on each semi – plane obtained. The 3D view is obtained by rotation of one semi-plane around symmetry axis(z).

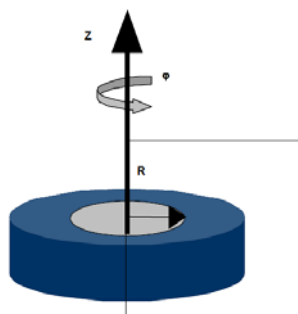


Figure 3.2. Example of an axisymmetric body

Referring to Fig. 3.2, on a magnetostatic problem, adopting a cylindrical coordinate system (r, ϕ, z) , we can obtain the following conditions:

- The current density has only ϕ component: $\mathbf{J} = (0, J_\phi, 0)$. This component is function of \mathbf{r} and \mathbf{z} coordinates;
- The magnetic vector potential \mathbf{A} has component parallel to vector \mathbf{J} only: $\mathbf{A} = (0, A_\phi, 0)$. As \mathbf{J} , A_ϕ varies with \mathbf{r} and \mathbf{z} ;
- The flux density vector \mathbf{B} has the component only on the (r,z) plane, as obtained from $\mathbf{B} = \nabla \times \mathbf{A}$:

$$\mathbf{B} = \left(\frac{\partial A_\phi}{\partial z}, 0, \frac{1}{r} \frac{\partial}{\partial r} (r A_\phi) \right)$$

2D harmonic analysis was adopted. It calculates the effect of an alternating current (AC) or voltage excitation in electromagnetic devices and moving conductors. These effects include:

- Eddy currents;
- Skin effect (eddy currents in current conductors carrying an impressed current);
- Power loss due to eddy currents;
- Forces and torque;
- Impedance and inductance;
- Two contacting bodies with dissimilar mesh;

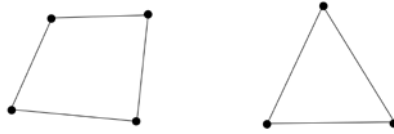
Permanent magnets are not permitted in a harmonic analysis. Material hysteresis effects are neglected.

For low saturation cases a linear time – harmonic analysis can be run with assumed constant permeability properties. In moderate to high saturation cases, an analyst is most interested in obtaining global electromagnetic force, torque and power losses in a magnetic device under sinusoidal steady state excitation, but less concerned with the actual flux density wave form. Under such circumstances, an approximate nonlinear time harmonic procedure may be pursued. This procedure can predict time averaged torque and power losses with good accuracy, and yet at much reduced computational cost compared to the transient time – stepping procedure.

The basic principle of this analysis is to replace the DC $B - H$ curve with a fictitious or effective $B - H$ curve based on energy equivalence method. With the effective $B - H$ curve, a nonlinear transient problem can be effectively reduced to a nonlinear time harmonic one. In this nonlinear analysis, all field quantities are all sinusoidal at a given frequency, similar to the linear harmonic analysis, except that a nonlinear solution is computed. It should be emphasised that in a nonlinear transient analysis, given a sinusoidal power source, the magnetic flux density B has a non-sinusoidal waveform. While in the nonlinear harmonic analysis, B is assumed sinusoidal. Therefore, it is not the true waveform, but rather represents an approximation to the fundamental time harmonic of the true flux density waveform. The time averaged global force, torque and losses, which are determined by the approximated fundamental harmonics of fields, are the subsequent approximations to the true values.

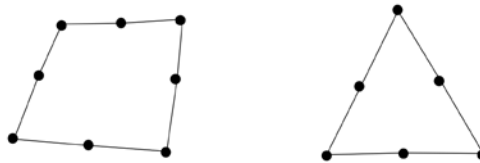
The kind of elements that were used in this analysis:

- PLANE 13: 2D element. Quadrilateral four nodes or, triangular three nodes.



It is defined up to four degrees of freedom per node: magnetic vector potential (AZ), displacements, temperature or time integrated electric potential.

- PLANE 53: 2D element. Quadrilateral eight nodes or, triangular six nodes.



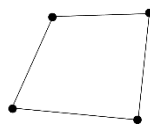
Up to four DOFs at each node: magnetic vector potential (AZ), time – integrated electric potential, current, or electromotive force drop.

Thermal transient analysis. Transient thermal analysis determines temperatures and other thermal quantities that vary over time. To specify time dependent loads, one possible approach is to divide the load versus time curve into load steps. Each step is treated like a steady state regime. It is possible to determine temperatures, thermal gradient, heat flow rates and heat fluxes. Such loads include the following:

- Convections;
- Radiation;
- Heat flow rates;
- Heat fluxes (heat flow per unit area);
- Heat generation rates (heat flow per unit volume).

The element adopted in the thermal analysis:

- PLANE 55: 2D element. Quadrilateral with four nodes.



One degree of freedom at each node: temperature.

A steady state or a transient analysis may be either linear, with constant material properties; or nonlinear, with material properties that depend on temperature, so the analysis is usually nonlinear. Including radiation effects also makes the analysis nonlinear.

To solve electro – thermal problem, the algorithm must be a loop that switches from the electromagnetic solution to the thermal one at every step. After having defined geometry and mesh, the electromagnetic analysis starts reading material properties, loading the current that is applied and fixing boundary conditions. Once that solution is reached the heat generated as joule losses are calculated from eddy currents distribution. Known the thermal boundary conditions, the final temperature profile is computed (since the DOF is unique). The number of steps is function not only of the heating time, but also of the desired level of accuracy.

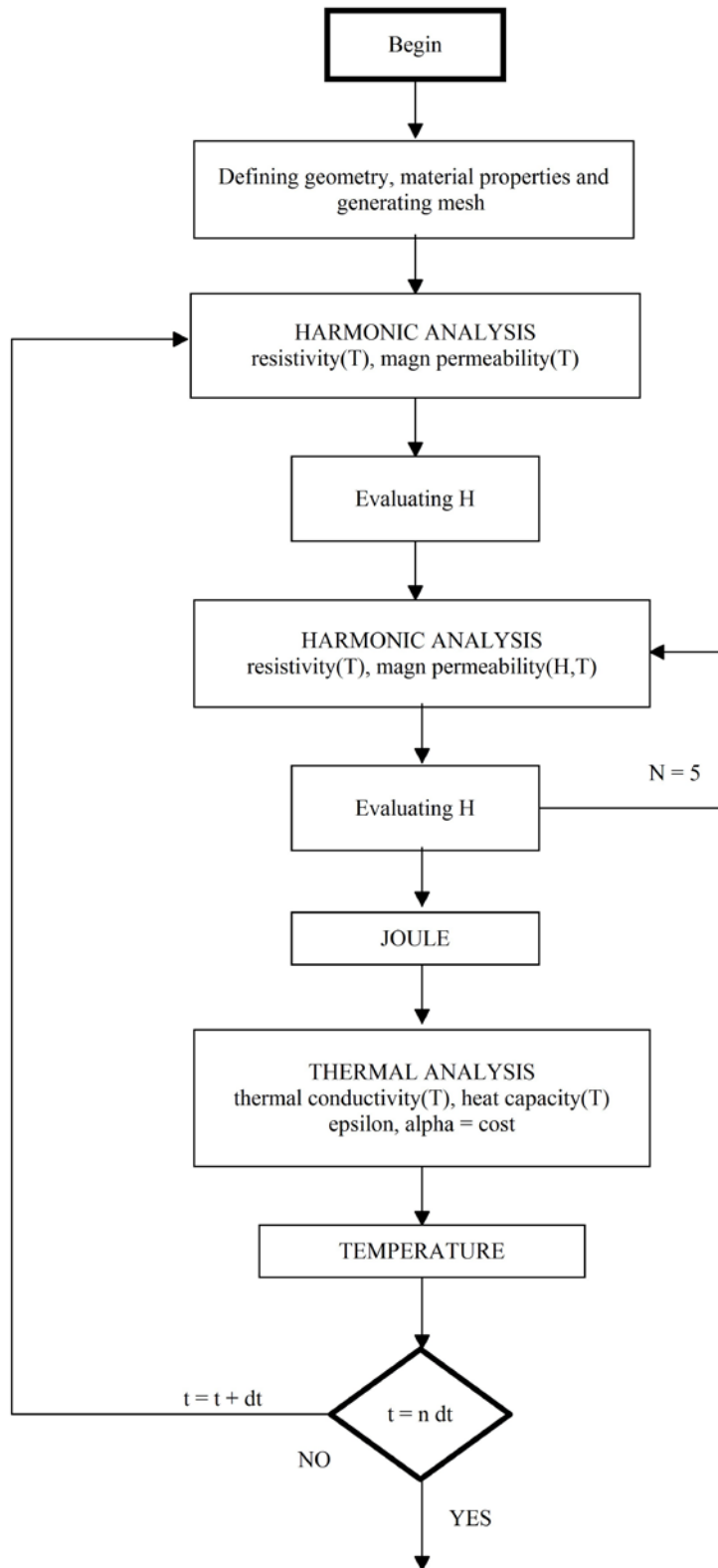


Figure 3.3. Flux diagram of the complete script

3.2.1 Preprocessing: geometry, materials, mesh

Defining geometrical parameters and material properties inside FEM model, gives the possibility to present work-piece characteristics.

The piece to be heated is a cylinder with a length of 474 mm and a diameter of 30 mm. It is made of carbon steel, specifically 42CrMo4. It is a versatile material that is mainly used in automobile and transport equipment. Its high strength and high toughness simultaneously, allow using it for highly stressed components such as steering knuckles, connecting rods, crankshafts, gears and sprockets.

Its chemical composition (values expressed in % of the weight) are the following:

| C | Si | Mn | P | S | Cr | Mo |
|-------------|---------|-------------|-----------|-----------|-------------|-------------|
| 0.38 – 0.45 | Max 0.4 | 0.60 – 0.90 | Max 0.025 | Max 0.035 | 0.90 – 1.20 | 0.15 – 0.30 |

In order to carry out the analysis is necessary to define the trend of four quantities. The first two regarding the electromagnetic analysis, the last two regarding the thermal one:

- Electrical resistivity – ρ

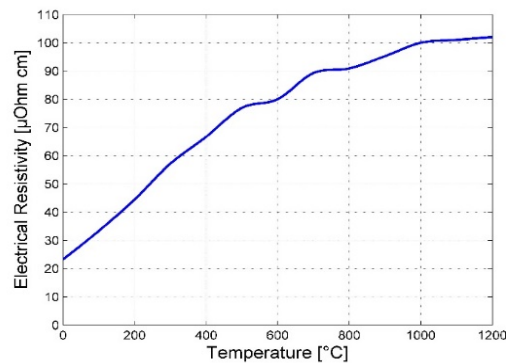
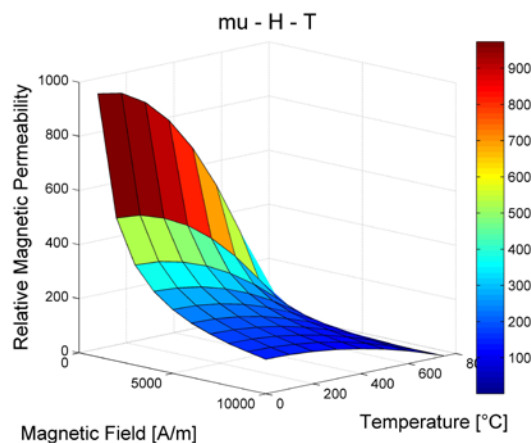


Figure 3.4. Electrical resistivity

The increase is not linear with temperature. As hinted in paragraph 2.2.9, the growth is faster between 0 and 800 °C, compared to that between 800 and 1200 °C. Resistivity at 1200 °C is five times higher the resistivity at room temperature.

- Relative magnetic permeability – μ



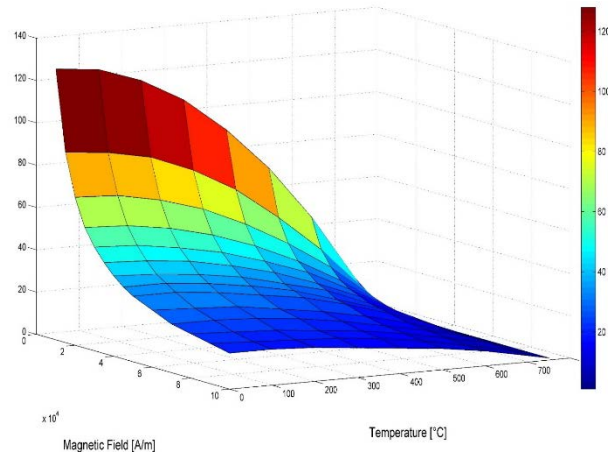


Figure 3.5. $\mu - H - T$ curves. In the first graph $1000 < H < 10\,000$ A/m, in the second $10\,000 < H < 100\,000$ A/m.

The two pictures show the dependency of the relative magnetic permeability (μ) on temperature and magnetic field.

$$\mu = \frac{B}{\mu_0 H} \quad (3.18)$$

The trend has been divided into two parts because of the particular high values of permeability for low magnetic fields. Permeability-surfaces were calculated with a semi-empirical formula (source ETP).

$$\mu = 1 + \left(2.41^{14.73 - \ln H} - 1\right) \left(1 - \frac{T^2}{T_C^2}\right) \quad (3.19)$$

Where H is the magnetic field [A/m], T temperature [°C] and T_C the Curie point [°C]. For this material the Curie temperature is supposed to be at 760 °C. At a given magnetic field, the influence of temperature on permeability is weak until 500 °C. It becomes dominant as temperature gets close to Curie's point.

- Thermal conductivity – λ

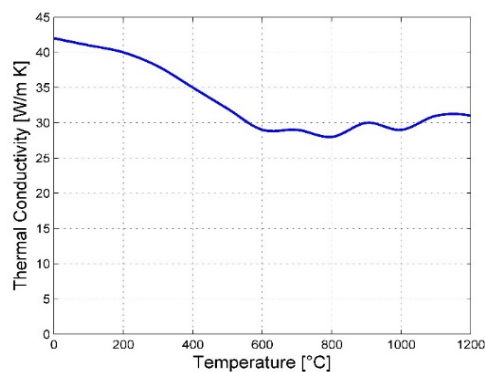


Figure 3.6. 42CrMo4 thermal conductivity function of temperature

In general the heating of the work-piece improves its ability to transmit heat.

- Specific heat capacity – c_p

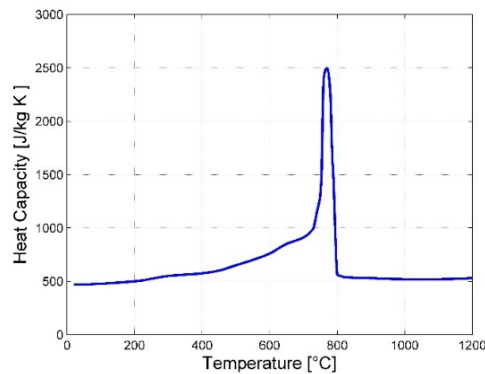


Figure 3.7. How specific heat capacity changes with temperature

The dependence of specific heat capacity is far from linearity. There is a distinct peak around the Curie temperature since energy is absorbed (or released) in destroying (or creating) the magnetic domains on heating (cooling). The spike is five times higher than the specific heat at 20 °C.

There are two other points that will be clarified in this paragraph. First the choice of the mesh, second the air box dimensions.

As explained in detail in the previous chapter, the distribution of the power induced inside the workpiece can be approximated by an exponential trend with a constant decay that values 2δ (δ is the penetration depth). So, it is preferable to adopt a more dense mesh near the surface, in this case for a thickness of 8 mm. Considering the values of penetration depth as a function of temperature shown in Fig. 3.8:

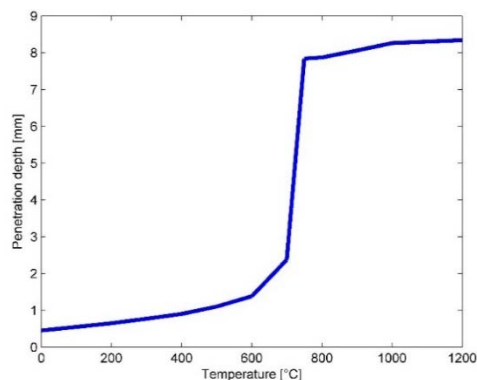


Figure 3.8. Penetration depth [mm] as a function of temperature

8 mm is the penetration depth value at 850 °C. With this choice, almost the overall power is induced inside the thickness with finer mesh during the entire heating process.

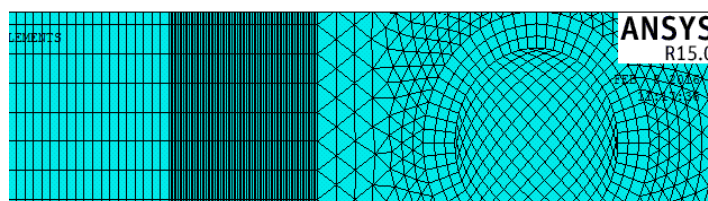


Figure 3.9. Mesh. On the left the workpiece, on the right one turn.

In Figure 3.9, on the left side, the radius of the workpiece 15 mm long is visible. The closer part to the axis of symmetry (7 mm large) has a coarser mesh, in the other (8 mm) is finer. This choice is a compromised between computational cost and precision of results.

Finally, the considerations of the air box's dimensions. For sure the air box must be much larger than the inductor – work-piece system but at the same time, an excessive size leads to unjustified computational cost. Since electromagnetic boundary conditions (null vector potential) are applied to the edge of the box, a too small air box is source of error. The optimal size is the minimum dimension for which, its increase causes a non-significant variation of the equivalent reactance of the load – inductor system. In the case in analysis the air box is 2 m long and 0.5 m large.

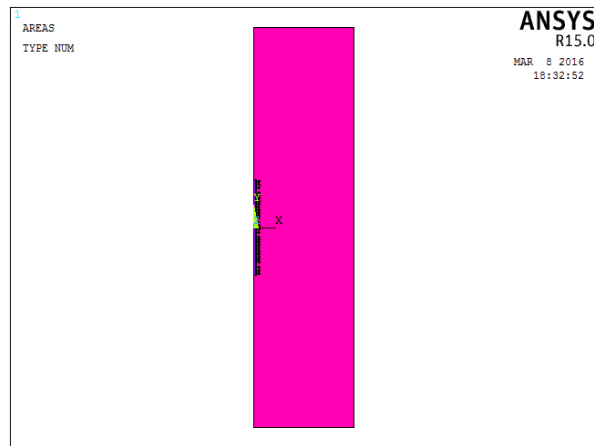


Figure 3.10. Air box dimensions.

3.2.2 Magnetic permeability dependency on H

Magnetic permeability is the only quantity, between those mentioned before, that does not depend only on temperature, but also on magnetic field strength H. A possible approach is to neglect the dependency on magnetic field, calculating different $\mu - T$ curves for different values of H in order to obtain an average trend. Another possibility, adopted in this script,

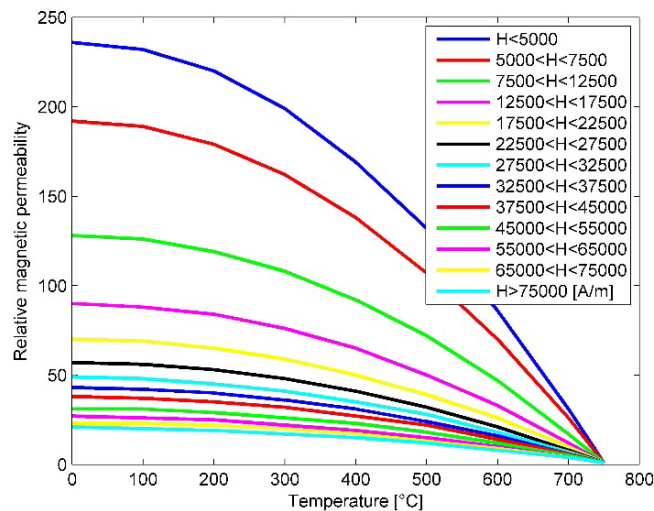


Figure 3.11. $\mu - T$ curves for different magnetic fields.

is to consider a discrete number of $\mu - T$ curves, evaluated at different magnetic field values (see Fig. 3.11).

In Figure 3.3 it is possible to see how this part of the script works. First is calculated an electromagnetic solution where the dependency of magnetic permeability on H is neglected. Then the H module is evaluated, in every element of the workpiece. In case a value is found, a $\mu - T$ curve is assigned to every appropriate element and a new electromagnetic solution is calculated. This procedure has been repeated for five times in order to reach the convergence. In fact, the difference of the magnetic field in each element between the last and the penultimate step is less than 0.05%. This approach, although characterized by increased complexity and computational cost, has the aim to simulate more closely the reality. An example is the greater magnetic saturation that occurs in the superficial layers.

3.3 Goal of investigation

The main goal of investigation is to obtain a final temperature profile that has particular features:

- 2 “hot” and 1 “cold” zones: must be recognizable two “hot” zones separated by one “cold”. The final temperature profile of these three zones must be as ideal rectangular as possible. For sure there are also two other “cold” zones at the edges of the workpiece, but they are not under investigation. We assume that the maximum final temperature at surface is 1100 °C. We define a “hot zone” a portion of the workpiece with a final temperature, in every point, higher than 1050°C. A “cold zone” is recognizable because its temperature is between 800 and 950 °C. These choices come from hot forging and warm forging temperature carbon steel. In an industrial application temperature requirements can be various and different by the number of hot and cold zones to the permitted temperature’s limit. Besides we won’t make restrictive assumptions about the size of these zones.
- *Uniformity along the radius*: the non-homogeneity is referred only to the axial direction. Since these heating are aimed for forging, must be minimum the difference of temperature between surface and centre. Anyway the hottest point along the radius is not at the surface but slightly inside.
- *Squared temperature profile*: it’s inevitable the presence of transitions areas between hot and cold zones where the temperature assumes values between 950 and 1050°C. The dimension of these areas must be minimum, i.e. the temperature gradient maximum.

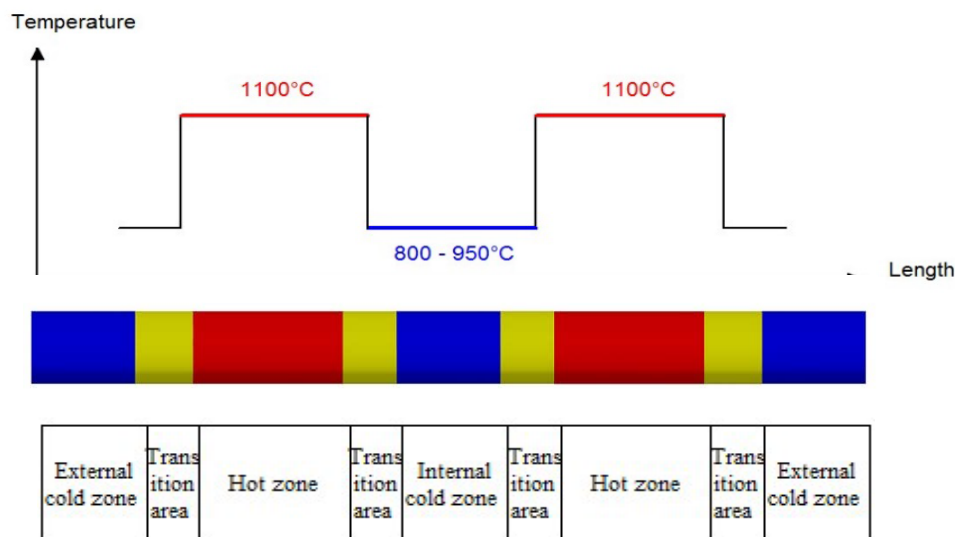


Figure 3.12. Sketch of the goal (a) and possible final temperature distribution (b)

To satisfy these demands there is a great variety of variables on which it is possible to act. First to mention is the inductor’s geometry. To differentiate a hot zone from a cold one, it is possible to increase the number of turns, thus reducing the air gap between turns. We can also modify the radius of the coil, increasing it in an area that needs to be heated less. However, this solution is not adopted here because it would introduce a complexity not justified by the simple geometry of the cylinder and due to reduced electromagnetic coupling it would decrease efficiency. Other alternatives can be the use of several

inductors, with the consequent use of more than one generator. This allows using, not only different powers, but also different frequencies. However, the lack of scientific material on this innovative method of heating and the will to carry out the experimental part, have preferred a solution as simple as possible. This means adopting a single inductor with constant diameter. The degrees of freedom that remain in geometry are related to the choice of: turns' number, diameter and thickness, gap between workpiece and coil, air gaps turn – turn. As regards the electrical quantities, it is possible to decide frequency and – current, power, voltage applied – depending on the type of control.

3.4 Inductor's design

3.4.1 Frequency

The first parameter fixed is the *frequency*. The choice is made in relation to the dimension of the cross section of the body to be heated, taking into account that for reducing the heating time, with the same difference of temperature between surface and axis, it is better to use low values of m . For reason of efficiency they must be higher than $2 \div 2.5$. On the other hand, high values of m , acceptable from the electrical efficiency point of view, give rise to distribution of heating sources mainly in the surface, with consequent increase of heating time and thermal losses. This means that for every diameter exist an interval of frequencies in which the heating is carried out conveniently. It can be defined:

- If $m < 2$ the electrical efficiency is too low;
- If $m = 2.5$ the frequency is optimal;
- If $2 \leq m \leq 5$ the heating is carried out with sufficient efficiency;
- If $m > 7$ thermal efficiency tends to be low.

Keeping also into account the average values of resistivity, relatively to the heating intervals, it is possible to obtain for each frequency, the diameters that can be heated cost effectively. In the case of heating carbon steel from room temperature to $1200\text{ }^\circ\text{C}$ a frequency in the following range:

$$\frac{3}{D^2} < f < \frac{6}{D^2} \quad (D \text{ in } m) \quad (3.20)$$

Permits to minimize the heating time.

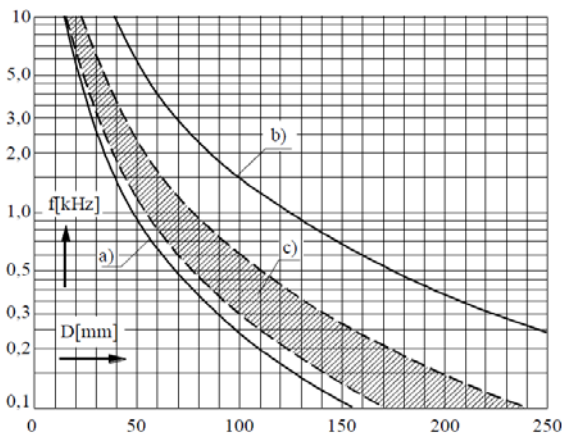


Figure 3.13. Limits of frequency as a function of diameter for heating of carbon steel billets until $1200\text{ }^\circ\text{C}$ a,b) lower and upper limit c) optimal frequencies

In this case we're analysing $D = 30\text{ mm}$, so the optimal frequency range is calculated to:

$$3.33 < f < 6.66\text{ kHz} \quad (3.21)$$

Another approach is to evaluate the best frequency considering $m = 2.5$ at the end of the heating ($1100\text{ }^\circ\text{C}$):

$$m_{\text{hot}} = \frac{\sqrt{2}R}{\delta} = R \sqrt{\frac{\omega \mu_0}{\rho}} = \sqrt{2\pi \frac{\mu_0}{\rho}} \sqrt{f} R = 2.5 \quad (3.22)$$

The result is 3.59 kHz . So it was decided to adopt 4 kHz as optimal frequency.

3.4.2 Inductor – work-piece air gap

The workpiece should be coupled in the best way with the inductor. As already shown in Chapter 2, reducing the air gap means to increase efficiency and power factor. At the same time the gap can't be too small because of the strong radiation which would be subjected to heat the inductor. The following table shows the recommended values:

| Frequency [kHz] | Air gap [mm] |
|-----------------|--------------|
| 1 – 3 | 3 – 6 |
| 10 – 25 | 2 – 3.8 |
| 50 – 450 | 1.5 – 2.25 |

A value of 5 mm has been chosen, i.e., the internal radius of the inductor is 20 mm.

3.4.3 Inductor's thickness

With the intention of maintaining the geometry simple, the section of the inductor is a cylinder with 10 mm external diameter. It's a value relatively small compared to the length of almost half a meter. But first, this permits to have a high number of turns, thus reducing the current necessary to generate the magnetic field. Second, it permits to define more easily cold and hot zones. As demonstrated in Chapter 2, there is a minimum value of thickness under that inductor losses tend to increase dramatically. This equation must be verified in order to avoid this phenomenon:

$$s \geq \frac{\pi}{2} \delta_i$$

$$s \geq \frac{\pi}{2} \sqrt{\frac{2 \rho_i}{\omega \mu_0}} \quad (3.23)$$

| | |
|----------|---|
| s | Thickness of the inductor [m] |
| ρ_i | Resistivity of copper ($1.9 \cdot 10^{-8}$ [$\Omega \text{ m}$]) |
| ω | Angular pulsation [s^{-1}] |

The inductor's resistivity is assumed constant since coils are water cooled. With a frequency of 4 kHz we obtain $s \geq 1.7$ mm. Thus we decided to adopt a thickness of 2 mm.

3.5 Cases of study

In this section four cases of study, which differ from each other mainly by the geometry (number of turns and gap turn – turn) will be presented. In paragraph 3.4 were already listed the characteristics that the final temperature profile has to satisfied. Besides, we would obtain a hot zone about 7 cm long. However, having this analysis the purpose of research, we are more interested in following and idealized profile (i.e. flat temperature profile in each zone) than in obtaining an area with a certain length (more typical in the case of an industrial process). To define the “quality” of the final temperature profile, some parameters are defined.

1. The *slope* of the temperature profile at the centre of the workpiece [°C/cm], in the transition zone (950 -1050°C). It is good that it is as steep as possible.
2. The ratio, named *h*, between the length of the hot zone obtained and the length of the coil that heats that zone. It's a way to express the capability to exploit the coil. It can't be higher than 1 (ideal case).

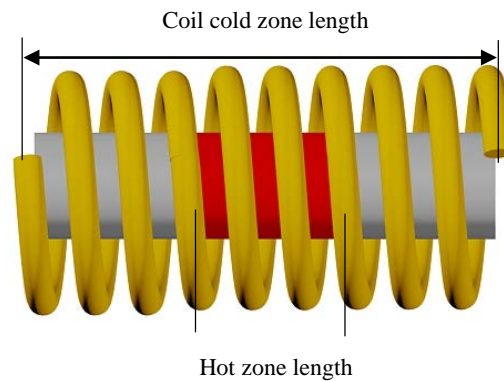


Figure 3.14. Sketch of which lengths are considered

$$h = \frac{\text{Hot zone length}}{\text{Coil cold zone length}} \quad (3.24)$$

3. The parameter *R* is a measure of how squared is the temperature profile. It values 1 in the case of a rectangular profile. For a hot zone, it's the ratio between the area under the temperature profile above 1050 °C, and the zone length and maximum temperature difference product.

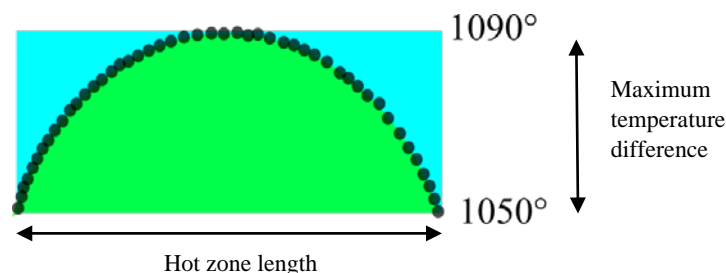


Figure 3.15. Given a final temperature profile (dots), how to evaluate *R*

$$R = \frac{\text{Green area}}{\text{Hot zone length} * \text{Maximum temperature difference}} \quad (3.25)$$

3.5.1 First model

Several tests have been done to reach the goal. Four models will presented, whose results can be considered satisfactory.

Referring to the definitions given in Fig. 3.12, inputs given in the first model are:

| | |
|--------------------------------------|------|
| Number of turns external cold zone | 3 |
| Number of turns hot zone | 9 |
| Number of turns internal cold zone | 3 |
| Air gap turn – turn hot zone [mm] | 4 |
| Air gap turn – turn cold zone [mm] | 12 |
| Air gap between different zones [mm] | 17 |
| Frequency [kHz] | 4 |
| Current [A] | 1000 |



Figure 3.16. Geometry of the model

In Fig. 3.16 we can see the geometry of the cylinder and the inductor. Because the model is axisymmetric, a single plane is shown. 3D configuration is obtained with the 360° rotation of the plane around y axis. The turns thus, do not constitute a single inductor, but they are independent, and in each the same current is applied. The work-piece is divided into two parts because different meshes are adopted.

These simulations were carried out keeping the current always fixed. It was chosen a value relatively high, 1000 A, in order to limit the heating time and typically the energy consumption, too.

Heating is considered finished when the superficial temperature reaches 1100 °C.

Electrical results:

| | |
|---|-------|
| Heating time [s] | 96 |
| Energy (work-piece + inductor losses) [kWh] | 0.675 |
| Maximum voltage [V] | 133.4 |

Thermal results:

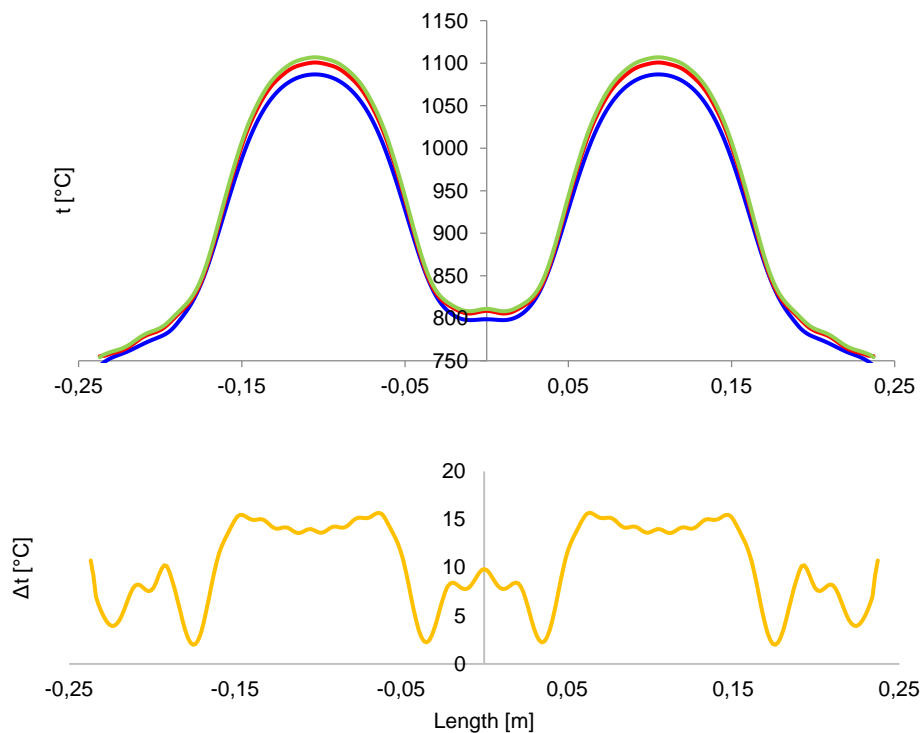
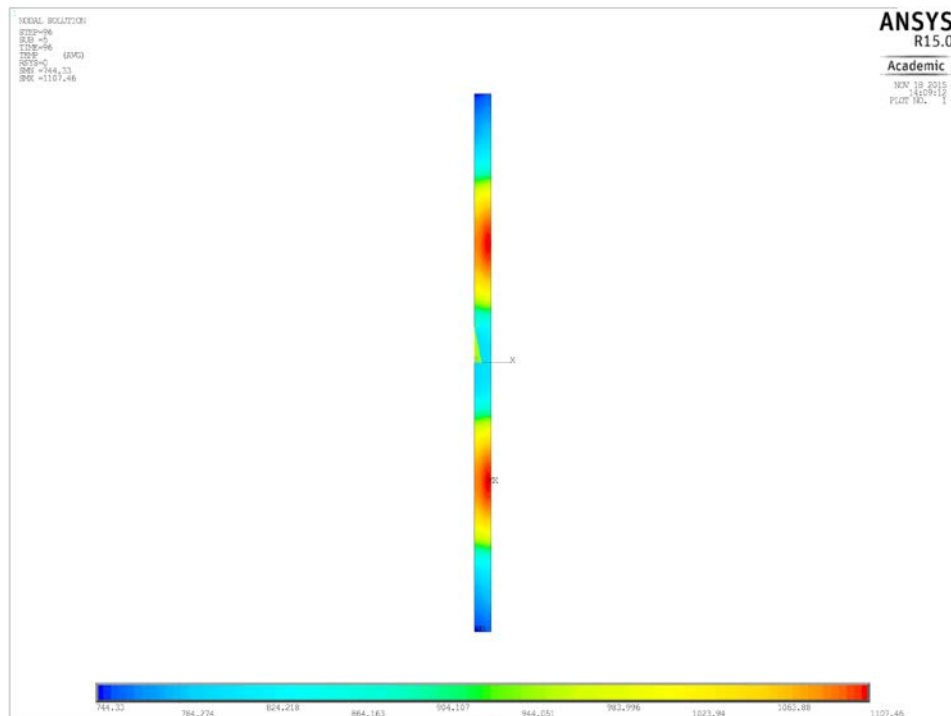


Figure 3.17. Thermal results with 96 s heating time a) final temperature b) thermal profile in indifferent depths c) surface – core temperature difference

The first picture shows the final temperature distribution. It is easy to distinguish two hot zones separated by a cold area. In the second image is shown the temperature trend, along the length, evaluated at different radius: core (null radius), surface (15 mm) and at 13 mm

from the centre. The core temperature is shown in blue, the surface in red and the third profile is green. In the last picture we can see the difference between surface and core temperature, once again along the length. Roughly, it tends to follow the intensity of magnetic field, since it reaches its maximum in the hot zones, instead its minimum in correspondence of the air spaces that separate different zones. In any case the difference of surface and core is always quite small and never higher than 16 °C.

Calculating the parameters defined in 3.5 paragraph introduction:

| | |
|--------------------|-------|
| Slope UP [°C/cm] | 51.3 |
| Slope DOWN [°C/cm] | -50.0 |
| h | 0.49 |
| R - surface | 0.776 |
| R - centre | 0.689 |

The slope “up” is referred to the transition zone temperature profile from the cold external zone to the hot zone (from 950 to 1050 °C). Instead the slope “down” is relative to the decrease of temperature from the hot zone to the internal cold zone. “h” is here 0.49. In fact, the hot zone is 6 cm long, where as the coil which heats up the hot zone has a length of 12.2 cm. “R”, calculated as indicated using the surface temperature, is not particularly high, since the temperature profile is not so smooth.

3.5.2 Second model

The geometrical and electrical variables in this second model can be summarized as:

| | |
|--------------------------------------|------|
| Number of turns external cold zone | 3 |
| Number of turns hot zone | 10 |
| Number of turns internal cold zone | 3 |
| Air gap turn – turn hot zone [mm] | 4 |
| Air gap turn – turn cold zone [mm] | 11 |
| Air gap between different zones [mm] | 12 |
| Frequency [kHz] | 4 |
| Current [A] | 1000 |



Figure 3.18. Second model geometry

Compared to the first model the number of turns in the hot zone has been increased by one. Since it has been not modified the turn-turn gap in the hot zone, we expect a larger hot zone compared to model 1. Because the total inductor length is unchanged, the dimensions of the cold areas are reduced.

Electrical results

| | |
|---|-------|
| Heating time [s] | 94.5 |
| Energy (work-piece + inductor losses) [kWh] | 0.718 |
| Maximum voltage [V] | 150.0 |

Thermal results:

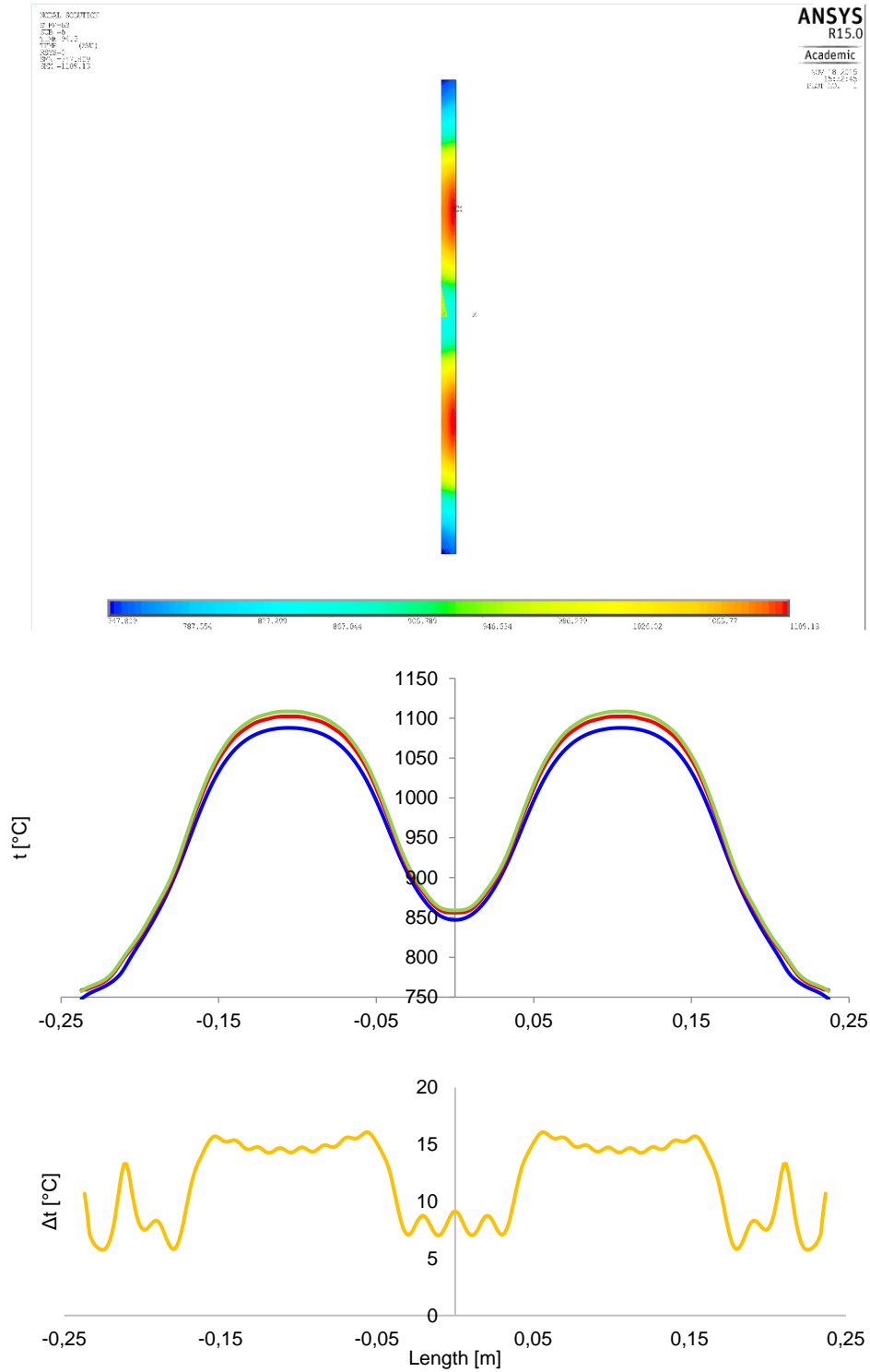


Figure 3.19. Thermal results relative to the second model

The heating time, between the first and the second model, remains almost unchanged. The consumption energy is higher (+6.4%), due to the fact that the work-piece is heated up more intensively, reaching 850 °C as a minimum temperature in central cold zone (instead of 800°) and extending the hot zones, now 7.9 cm long (instead of 6 cm). Adding two more turns has increased the maximum voltage.

The parameters defined here value:

| | |
|--------------------|-------|
| Slope UP [°C/cm] | 46.3 |
| Slope DOWN [°C/cm] | -41.3 |
| h | 0.58 |
| R - surface | 0.800 |
| R - centre | 0.713 |

The slope is lower with respect to the first model, because the temperature difference between the zones is reduced. The profile temperature in the hot zones can be considered satisfactory, since it is quite flat. This is confirmed by the R-values, which are definitely higher in this second model. However, the profile in the central cold area is for sure improvable in order to get a more flat trend.

3.5.3 Third model

The input parameters in this new model are:

| | |
|--------------------------------------|------|
| Number of turns external cold zone | 3 |
| Number of turns hot zone | 10 |
| Number of turns internal cold zone | 3 |
| Air gap turn – turn hot zone [mm] | 3 |
| Air gap turn – turn cold zone [mm] | 14 |
| Air gap between different zones [mm] | 14 |
| Frequency [kHz] | 4 |
| Current [A] | 1000 |



Figure 3.20. Geometry of the third model

The number of turns is unchanged with respect to the second model, but the distribution is different: turns are closer in the hot zones and they are more distant in the cold one.

Electrical results:

| | |
|---|-------|
| Heating time [s] | 78 |
| Energy (work-piece + inductor losses) [kWh] | 0.644 |
| Maximum voltage [V] | 150.5 |

Thermal results:

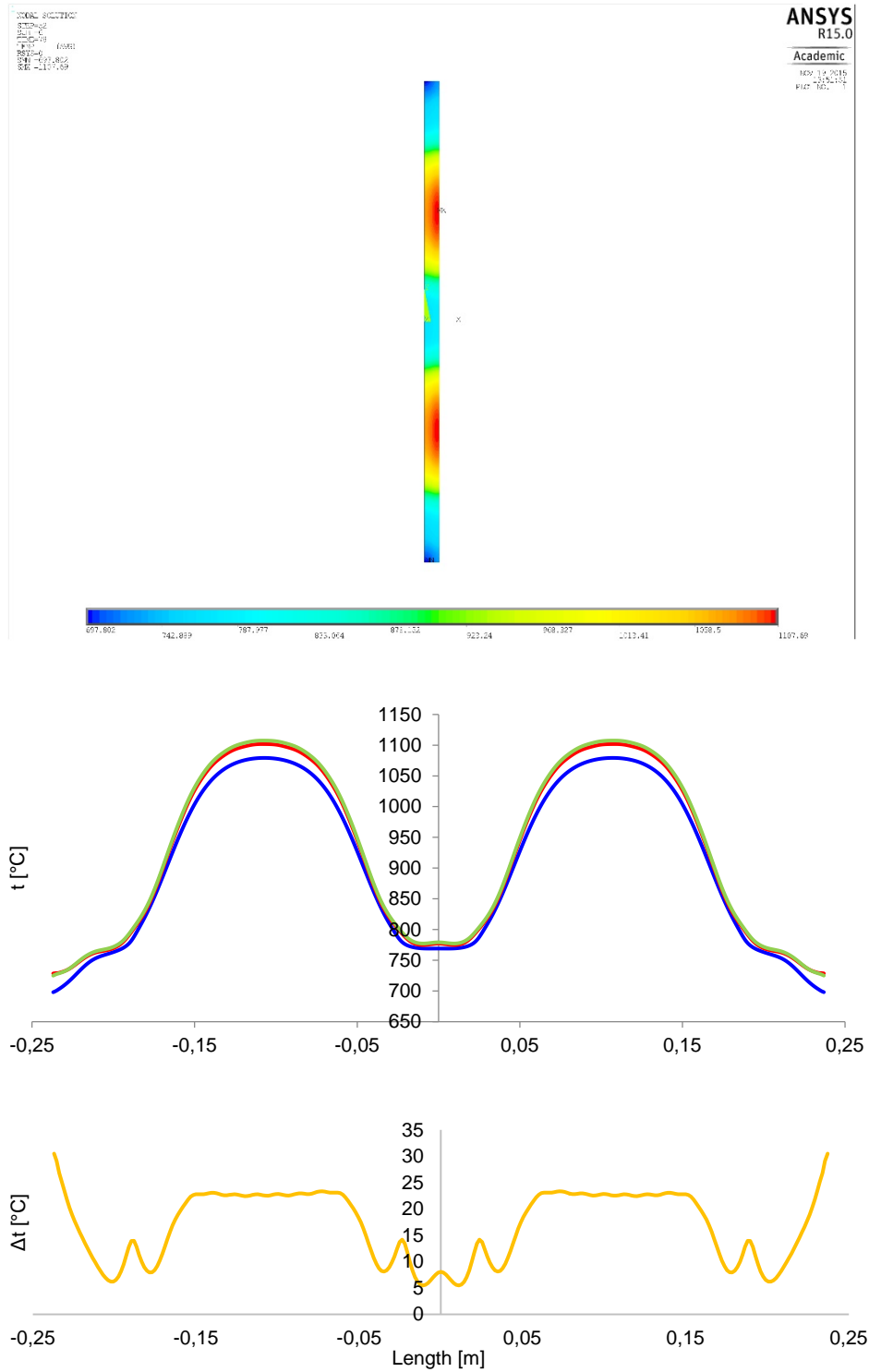


Figure 3.21. Thermal results with 78 s heating time

The parameters defined:

| | |
|---|-------|
| Slope UP [$^{\circ}\text{C}/\text{cm}$] | 48.7 |
| Slope DOWN [$^{\circ}\text{C}/\text{cm}$] | -50.0 |
| h | 0.47 |
| R - surface | 0.836 |
| R - centre | 0.704 |

The strong heating time reduction leads to save energy, and to increase not only the temperature difference between zones but also between surface and core. The temperature profile is quite smooth. There is one improvable issue related to the cold zone, where the temperature is lower than $800\text{ }^{\circ}\text{C}$.

3.5.4 Fourth model

In the last model was decided to increase by one the turns in the cold zones, in order to increase the temperature.

| | |
|--------------------------------------|------|
| Number of turns external cold zone | 4 |
| Number of turns hot zone | 10 |
| Number of turns internal cold zone | 4 |
| Air gap turn – turn hot zone [mm] | 3 |
| Air gap turn – turn cold zone [mm] | 6 |
| Air gap between different zones [mm] | 11 |
| Frequency [kHz] | 4 |
| Current [A] | 1000 |



Figure 3.22. Projection of geometry of fourth model

Electrical results:

| | |
|---|-------|
| Heating time [s] | 78 |
| Energy (work-piece + inductor losses) [kWh] | 0.707 |
| Maximum voltage [V] | 176.7 |

In this model the coil has 32 turns, instead of 30 in the model two and three, and 28 in the first model. Since the cold zones are heated up more, the energy consumption increases.

Thermal results:

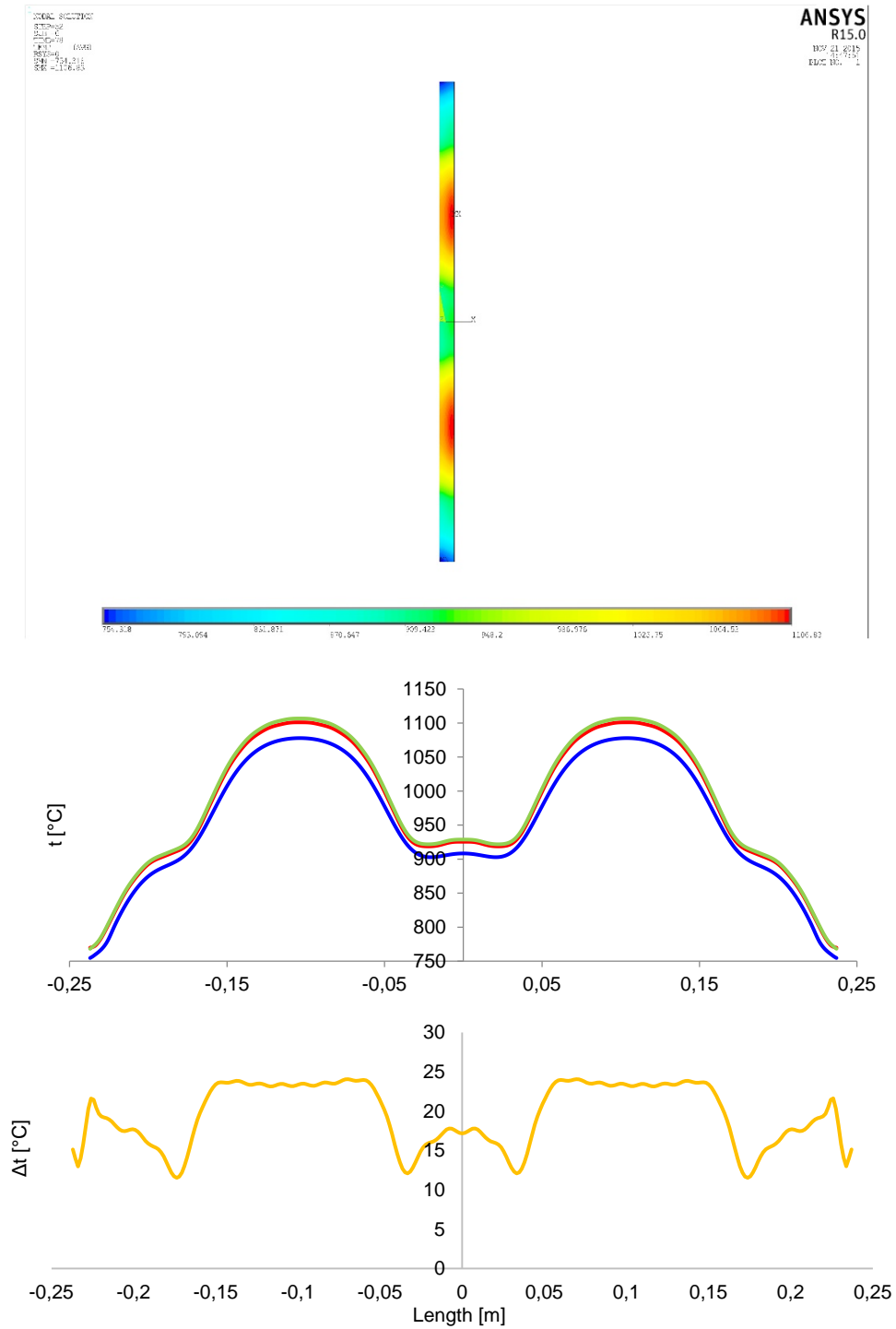


Figure 3.23. Thermal results with 78 s heating time in the case of the fourth model

The parameters value:

| | |
|--------------------|-------|
| Slope UP [°C/cm] | 35.8 |
| Slope DOWN [°C/cm] | -36.3 |
| h | 0.51 |
| R - surface | 0.844 |
| R - centre | 0.701 |

The maximum voltage reached in this model is higher than all the other models. The temperature distribution is quite smooth in the interested areas. A fact confirmed by the high values that assumes R. The main defect of this model is the temperature difference between core and surface, which varies between 12 and 24 degrees. This problem can be easily solved with equalization. The temperature gradient between zones is not that high, as a consequence of the small gap between turns of different zones.

3.6 Final model

Even if the models presented have achieved satisfactory results, none is able to provide a truly squared temperature profile. All the profiles have a maximum at the centre of each zone. This is a consequence of the magnetic field distribution. In the cases of study, in each zone, the magnetic field is not uniform along the axis but tends to be higher in the middle. This comes from the choice of using constant air gap between turn and turn. A way to obtain a more flat temperature distribution is to have a magnetic field as uniform as possible. An easy solution to this problem is to increase the turn-turn air gap at the centre, and to decrease it at the edges.

An example now is showed. Let's consider an inductor, without work-piece inside, 128 mm long with 10 turns, each with 10 mm diameter. In the case A, a fixed air gap of 3.1 mm between turn and turn was chosen. In the case B, gaps value 2 mm at the edges and 4 mm in the central part. All the other parameters are equal.



Figure 3.24. Inductor (axisymmetric model) with fixed (A) and changing (B) air gap

Applying a current of 1000 A, the magnetic field module changes, in cases A and B, as shown in Fig. 3.25.

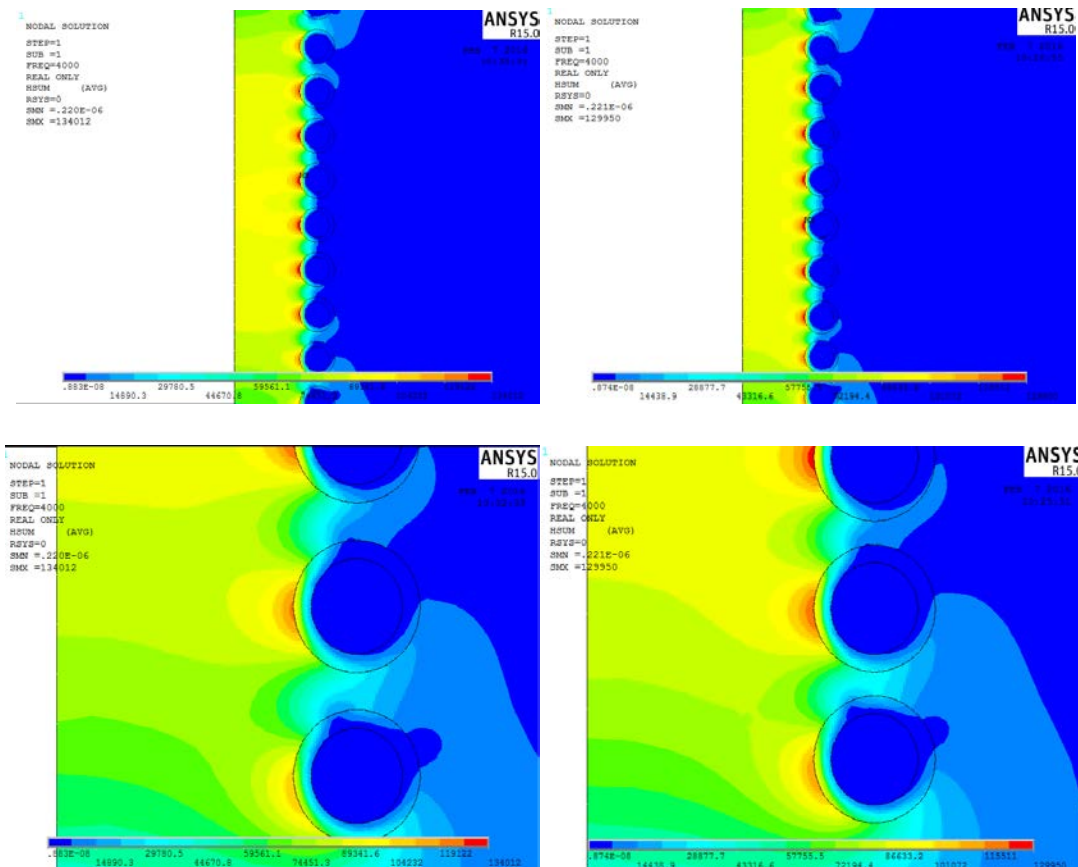


Figure 3.25. Magnetic field module distribution in cases (A) and (B)

The distribution is more uniform in case B, both at the edges than in the central part. This good result has convinced us to adopt this arrangement in the next model.

3.6.1 Input

It has not been changed the number of turns used, respect to the fourth case of study. The difference is their distribution.



Figure 3.26. Geometry of the last model

| | |
|--------------------------------------|-------------|
| Number of turns external cold zone | 4 |
| Number of turns hot zone | 10 |
| Number of turns internal cold zone | 4 |
| Air gap turn – turn hot zone [mm] | 2 or 4 |
| Air gap turn – turn cold zone [mm] | 2 or 4 or 6 |
| Air gap between different zones [mm] | 16 or 12 |
| Frequency [kHz] | 4 |
| Current [A] | 1000 |

3.6.2 Results

The heating time values 80 seconds. Now are presented how some electrical parameters change during the heating.

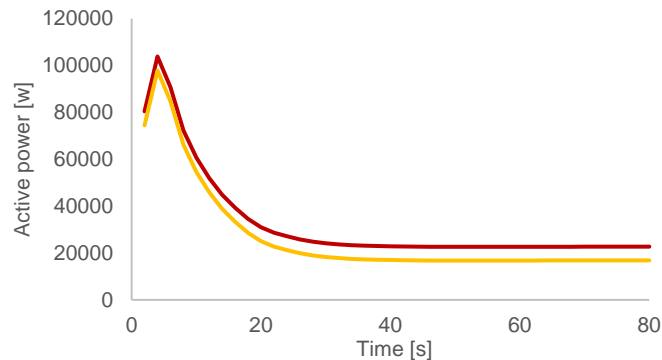


Figure 3.27. Active power trend. Orange – power induced in the work-piece. Red – power induced plus power lost in the copper

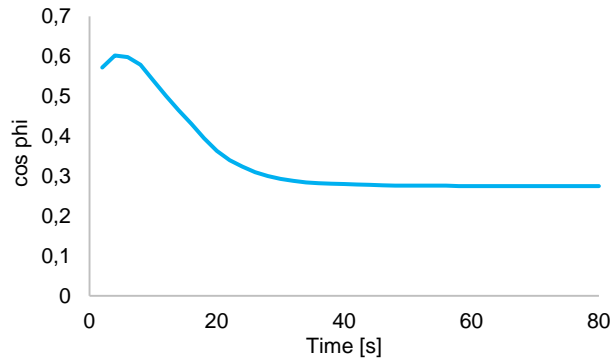


Figure 3.28. cos phi trend in time

The simulation is carried out, as always until now, considering the current and the frequency fixed. Because of the changing of material properties, the power induced in the work-piece is not all that constant. The power lost in the copper instead doesn't change so much in time. The power factor at the end of the heating is halved compared to the initial one. This comes from the fact that, during heating with constant current, power induced falls.

| | |
|---|-------|
| Heating time [s] | 80 |
| Energy (work-piece + inductor losses) [kWh] | 0.721 |
| Maximum voltage [V] | 172.5 |

Heating time is longer than in the fourth model, and in fact the energy consumption is higher. In Fig. 3.29 is shown magnetic field module distribution at the beginning and at the end of the process. Magnetic field penetrates inside much more with hot work-piece.

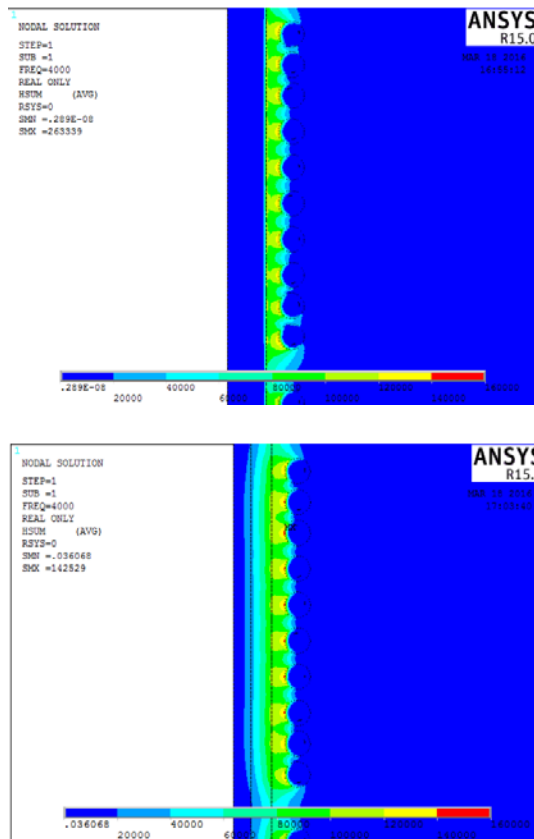


Figure 3.29. Magnetic field module distribution in the hot zone after 2 and 80 seconds

The final temperature distribution is the following.

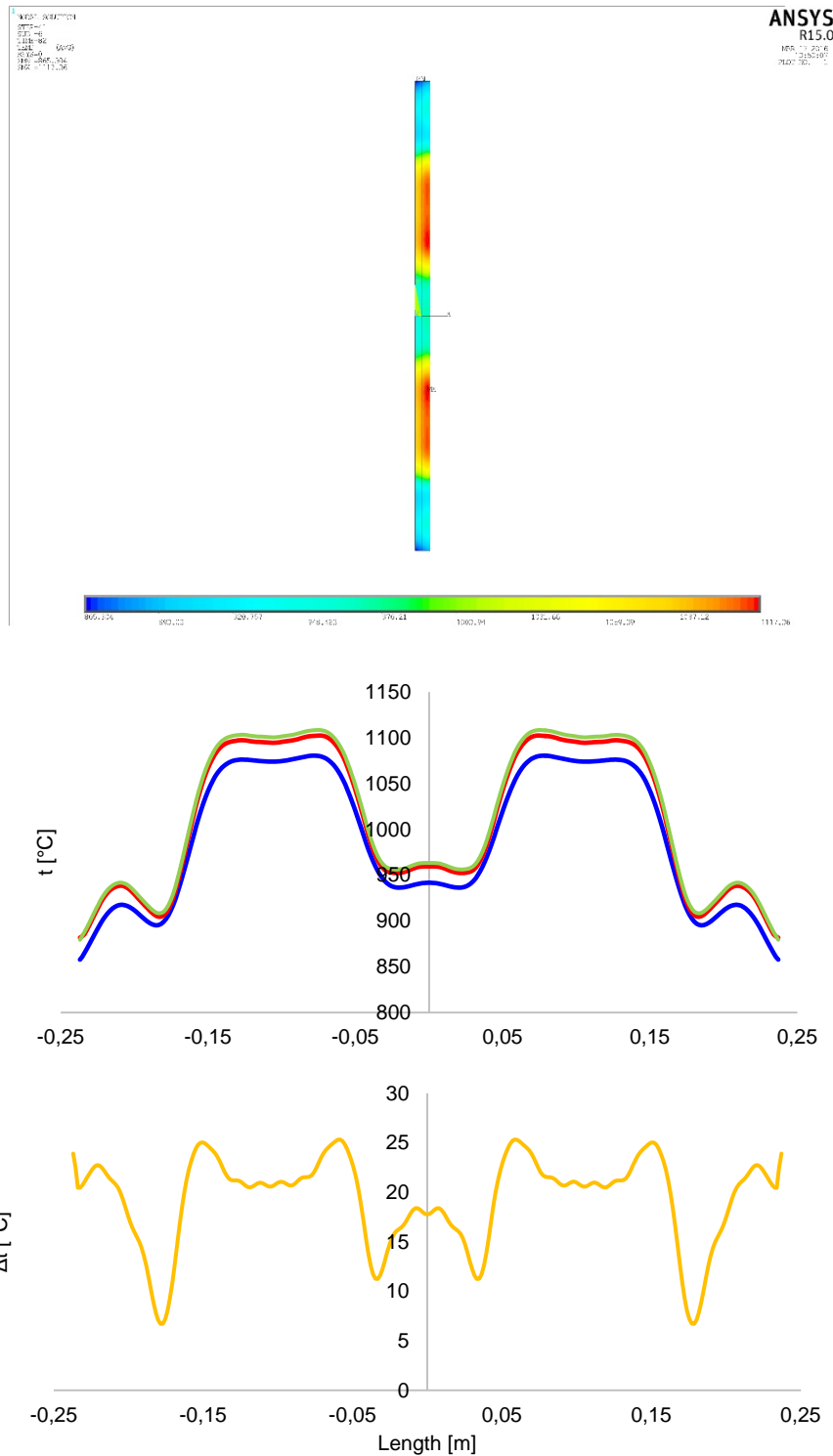


Figure 3.30. Thermal results with 80 s heating time a) final temperature distribution b) thermal profile in indifferent depths c) surface – core temperature difference

The surface-core temperature different doesn't overcome 25°C. The temperature profile is really squared, fact also emphasized by the parameters calculated below. "R" assumes values never reached in the models before. This convinced us to realize the model with this geometry.

| | |
|---|-------|
| Slope UP [$^{\circ}\text{C}/\text{cm}$] | 52.7 |
| Slope DOWN [$^{\circ}\text{C}/\text{cm}$] | -39.6 |
| h | 0.70 |
| R - surface | 0.867 |
| R - centre | 0.769 |

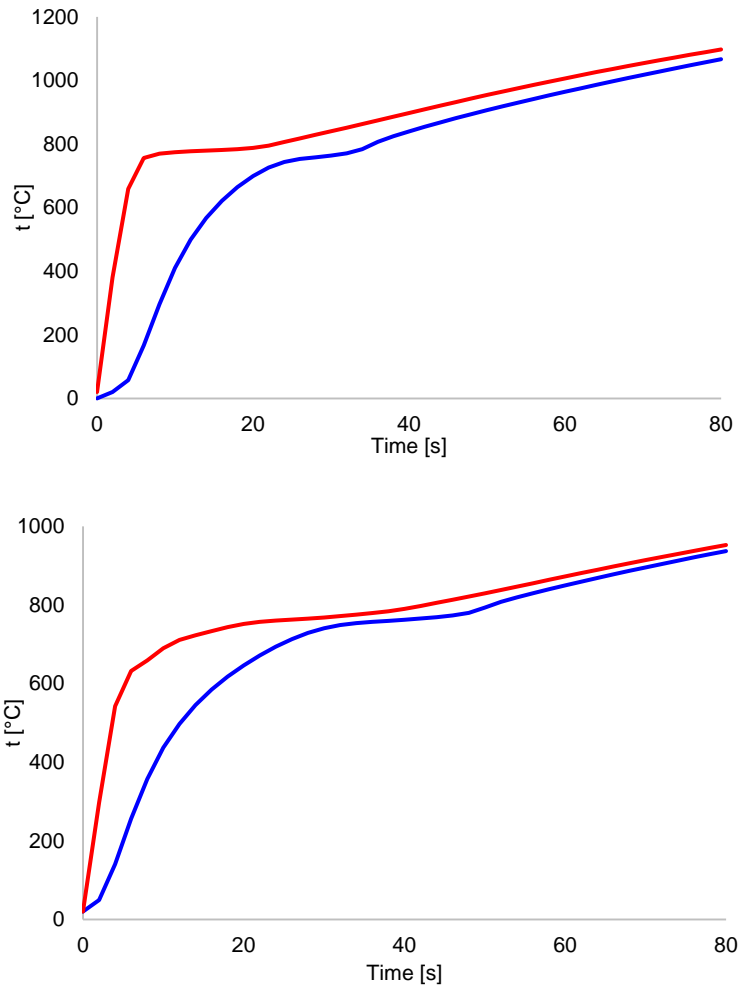


Figure 3.31. Temperature at surface (red) and core (blue) in time, evaluated in the hot zone (A) and in the cold zone (B).

It is evident the different temperature growth during the process, both at surface than at core. At the beginning of the heating, especially due to the high magnetic permeability, temperature increases very fast. Then is recognizable a plateau in correspondence to the Curie temperature. This comes from the high heat capacity and, at the same time, from the demagnetization of the material that happens around 760 $^{\circ}\text{C}$. In the last part of the heating, the temperature growth occurs with a linear dependency since the material has lost its magnetic properties.

3.7 Homogeneous vs Inhomogeneous

One of inhomogeneous heating benefits is the possibility to save energy. Now we compare results obtained in the last model and the heating carried out with an inductor that has a constant air gap between turn and turn. Length, diameter, thickness, number of turns and current are the same.

| | Inductor with constant gap | Final model |
|----------------------|----------------------------|-------------|
| Number of turns | 32 | 32 |
| Inductor length [mm] | 474 | 474 |
| Current [A] | 1000 | 1000 |
| Frequency [kHz] | 4 | 4 |

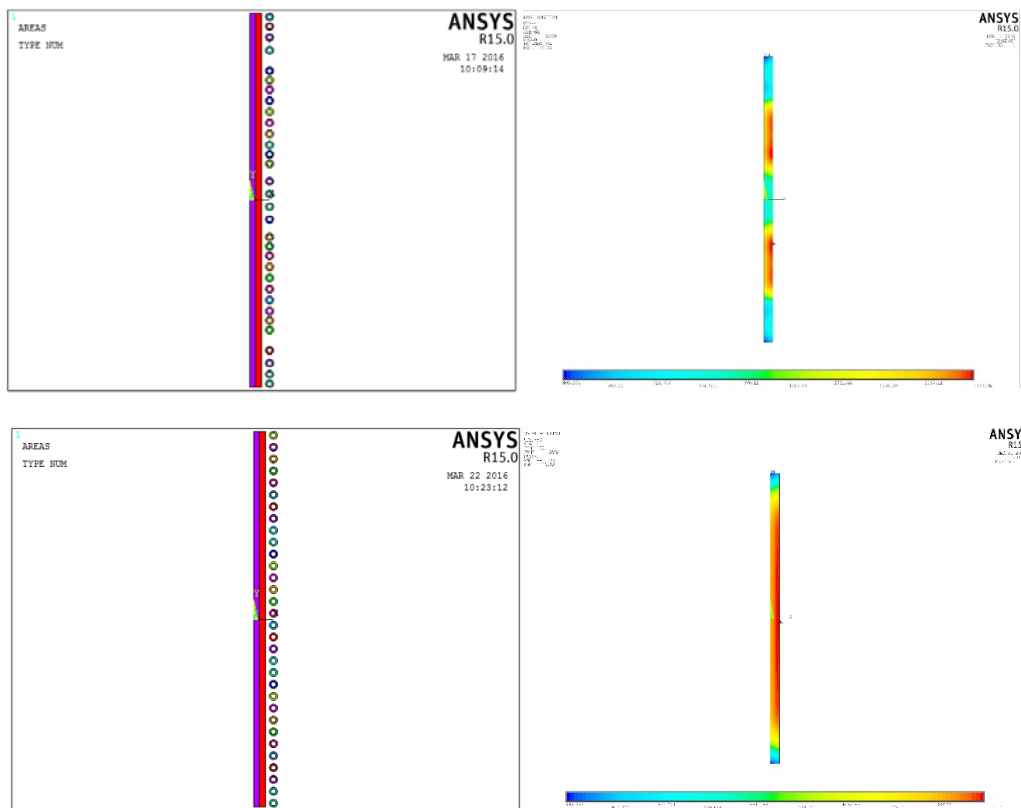


Figure 3.32. Geometry and final temperature profile in case of inhomogeneous and homogeneous heating

The goal is always the same, i.e., to reach a final surface temperature of 1100 °C. The energy consumption in the case with constant air-gap is inevitably higher, first because the work-piece is heated up more, and second because of the increase duration of the heating.

| | Inductor with constant gap | Final model |
|--------------------------------|----------------------------|-------------|
| Time [s] | 100 | 80 |
| Total electrical energy [kWh] | 0.831 | 0.721 |
| Energy induced in the wp [kWh] | 0.677 | 0.591 |
| Losses in the copper [kWh] | 0.154 | 0.129 |
| Thermal energy [kWh] | 0.512 | 0.485 |
| Thermal losses [kWh] | 0.165 | 0.107 |

Total electric energy is obtained as the integration in time of the power absorbed at the inductor terminals. It is the sum between the energy lost in the copper and the induced one in the body to heat. If, at the end of the heating, we evaluate thermal energy in each element using:

$$dQ = c_S \gamma \Delta T dV \quad (3.26)$$

| | |
|----------------|------------------------------------|
| dQ | Thermal energy [J] |
| c _S | Equivalent specific heat [J/kg °C] |
| γ | Density [kg/m ³] |
| ΔT | Final – Initial temperature [°C] |
| dV | Element volume [m ³] |

Where c_S is an equivalent specific heat, function of the final temperature, assumed constant during the heating. It is calculated as:

$$c_S = \frac{\int_{20}^T c_P dT}{T-20} \quad (3.27)$$

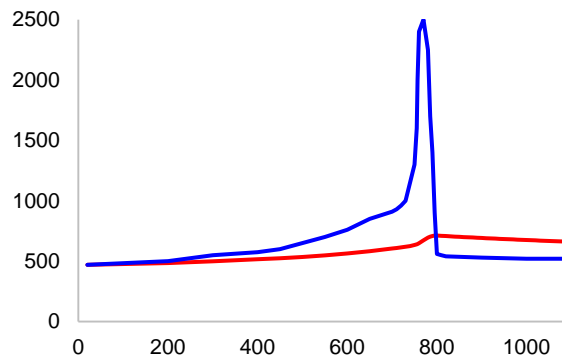


Figure 3.33 Specific heat c_P (blue) and equivalent specific heat c_S (red).

Integrating dQ in the all work-piece, it is possible to know thermal energy stored inside the body. The value obtained is lower than the power induced by a quantity equal to the heat losses towards the environment. Electrical and thermal efficiency are instead defined as:

$$\eta_{\text{electrical}} = \frac{\text{Energy induced in the wp}}{\text{Total electrical energy}} \quad (3.28)$$

$$\eta_{\text{thermal}} = \frac{\text{Thermal energy}}{\text{Energy induced in the wp}} \quad (3.29)$$

$$\eta = \eta_{\text{electrical}} \eta_{\text{thermal}} = \frac{\text{Thermal energy}}{\text{Total electrical energy}} = 1 - \frac{\text{Losses}}{\text{Total electrical energy}} \quad (3.30)$$

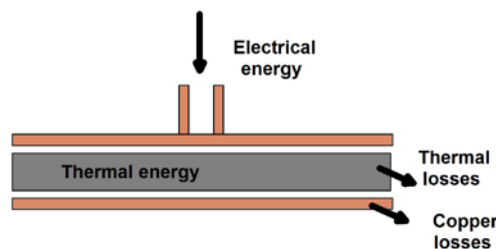


Figure 3.34 Sketch of the powers involved in an induction heating process

Using definitions introduced in (3.28), (3.29) and (3.30), we get:

| | Inductor with constant gap | Final model |
|-----------------------|----------------------------|-------------|
| Electrical efficiency | 0.814 | 0.820 |
| Thermal efficiency | 0.756 | 0.819 |
| Overall efficiency | 0.625 | 0.673 |

In this example, the saving-energy margin is really interesting adopting a non-homogenous heating instead of a traditional homogeneous one. Since the current imposed is the same in the two cases, the induced power trend does not vary much. Higher time (100 instead of 80 seconds) means not only higher energy consumption, but also more losses in the inductor and towards the environment. In particular, in the final part of the heating – with hot work-piece, the ratio between losses and induced power is maximum. In the inhomogeneous case, heating time is smaller because in the hot areas turns are very close each other (until 2 mm), developing in this way high magnetic fields with consequent strong local heating. The same phenomena responsible of a higher energy consumption, are also the reasons that reduce efficiency, in particular that thermal.

4. Practical activities

This chapter can be subdivided into two main parts. In the first, object of investigation are choices about how to manufacture the inductor. The second is relative to laboratorial activities and data elaboration.

4.1 Power supply

It is theoretically possible to connect the inductor with the work-piece directly to an AC power supply. This can be done provided the frequency of the voltage source can be adjusted to the requirements of the process. For the most practical requirements it can be seen that the inductor's reactive current will be several times greater than the active current. Only the active current causes the work-piece to heat up, but however high current is necessary to create an alternating field. Since the power source and the transmission paths are subject to extreme loads due to its intensity, they would have to be multiply over dimensioned to cover the reactive current requirements. For this reason it is better that reactive power of the inductor is generated within the load. This can be done with an oscillating circuit, connecting a capacitor in parallel or in series to the inductor.

Induction heating converters belong to the so called load-resonant converters family. Commutating at resonant frequency allows having more efficient equipment, which may be essential in some high frequency applications. One common criteria is classifying converters according to the type of resonant tank, where the most basic typologies are those based on series and parallel tanks. The converters associated to these tanks are the voltage-fed series resonant inverters (VFSRI) and the current-fed parallel resonant inverters (CFPRI) respectively.

4.1.1 Converter topologies

Voltage-fed series resonant inverters (VFSRI)

In series resonant tanks, the inductor is connected in series with the capacitor. The inverter used is a voltage-fed inverter. This implies that the inverter is fed by capacitor with a high capacitance value that maintains the voltage constant. In most applications above 5 kW, the inverter used is the H-bridge, as shown in Figure 4.1. In these inverters, two switches of the same inverter cannot be turned-on at the same time, otherwise short circuit occurs. Antiparallel diodes are necessary to allow inductor's current conduction when opposite switches are turned-off.

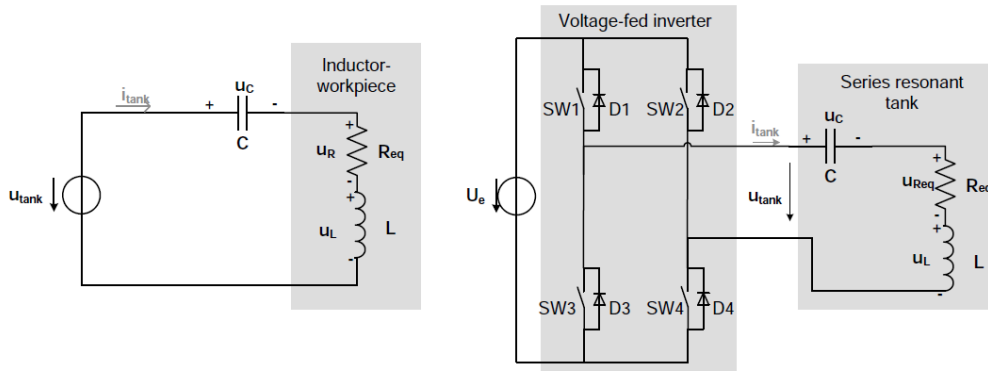


Figure 4.1. Series tank and a VFSRI

The current in the tank is the same than in the inverter. Considering that the equivalent impedance of the oscillating system is usually lower than one ohm, voltages in the inverter are low and the current high. From the inverter's point of view, this is source of high losses and voltage drops. Using matching transformers between inverter and load, it is possible to reduce the current that flows in the power supply semiconductors. A transformer makes the final product more expensive and reduces the efficiency of the system. Nevertheless, it is worth pointing out that transformers efficiency is usually higher than 95%.

Since the power is absorbed by the grid, it is also necessary an AC/DC conversion, through a rectifier. In the case of series resonant inverters, in the input section can be used a non-controlled diodes rectifier. The power is controlled only through the inverter.

Current-fed parallel resonant inverters (CFPRI)

Current-fed inverters are more complex than its counterpart the voltage-fed one, as the power regulation is performed with controllable input section normally built with a fully controlled rectifier in the case of high power inverters or a diodes rectifier and a chopper in the case of low power. The inclusion of a DC/DC intermediate stage decreases efficiency.

The inverter is fed with a high inductance that maintains the current and behaves as a constant current source. A parallel tank and an ideal CFPRI are shown in Figure 4.2. In case of current-fed inverters, the current path cannot be opened. If diodes, in series with switches, are not added the capacitor would discharge.

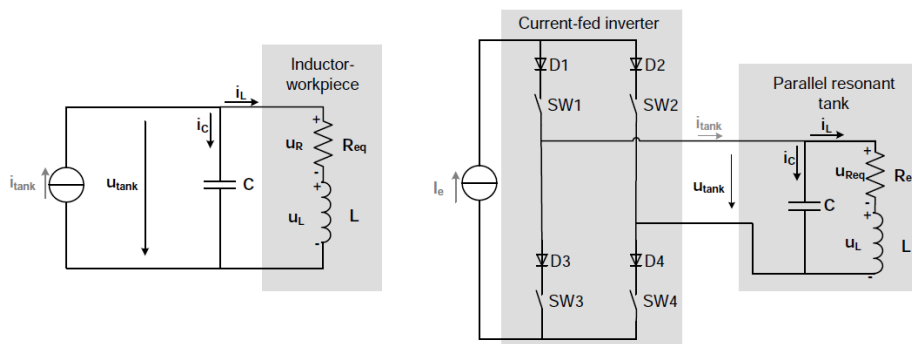


Figure 4.2. Parallel tank and a CFPRI

Inverter with three element tanks

Series and parallel tanks and their associated inverters have some drawbacks that have led to the investigation of other topologies. In case of VFSRI, the current in semiconductors is the same than in the load, which implies the need of a matching transformer between inverter and load, increasing the cost of the system and decreasing the efficiency. In case of CFPRI, the current in the inverter is lower than in the inductor, but the inverter is current-fed. This makes difficult the use of commercial equipments due to the overvoltage protection system needed. Moreover, the cable between converter and tank is critical due to the parasitic inductance that limits between them. In order to overcome these limitations, systems with three element tanks have been developed.

There are several possibilities concerning tanks with three elements, but most popular is LCL (also called LLC). An LCL tank is a parallel tank with an inductance L_s in series as shown in Fig. 4.3. They use voltage-fed inverters, providing the benefits of commercial devices and protection systems, and the current in semiconductors is lower than in the inductor, like in CFPRI.

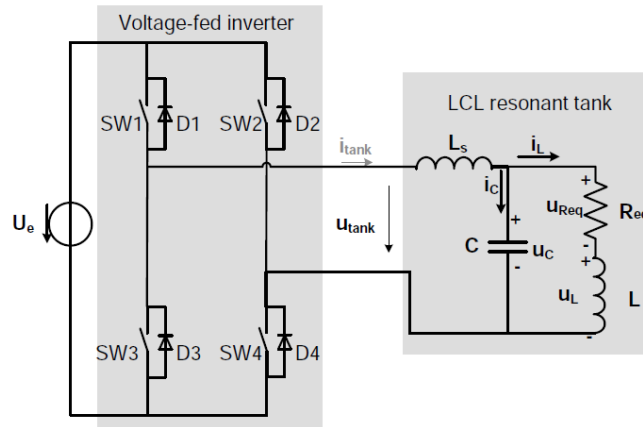


Figure 4.3. Voltage-fed inverter with a LCL tank

The value of the complex input impedance of the resonant tank defines two resonant angular frequencies. They can be found by calculating those frequencies which result in either infinite or zero input impedance. The results, neglecting R_{eq} :

$$\begin{aligned} \dot{z} \rightarrow 0 & \quad \omega_{rs} = \frac{1}{\sqrt{C L L_s / (L L_s)}} \\ \dot{z} \rightarrow \infty & \quad \omega_{rp} = \frac{1}{\sqrt{L C}} \end{aligned}$$

The frequency f_{rp} is equal to the resonant frequency of the parallel circuit, and f_{rs} is the resonant frequency of the union with L_s . Usually the resonant frequencies are quite close because $L_s \gg L$ as shown:

$$R = 0.1 \, \Omega \quad L = 9.78 \, \mu\text{H} \quad L_s = 95.37 \, \mu\text{H} \quad C = 6 \, \mu\text{F}$$

$$f_{rp} = 20.78 \, \text{kHz} \quad f_{rs} = 21.82 \, \text{kHz}$$

The LCL resonant tank is supplied by a voltage source inverter. It operates at the resonant frequency defined by the complex input impedance $\dot{z} \rightarrow 0$, which is the resonance point of a series resonant circuit. The current in the heating inductor is approximately L_s/L time the current in the inverter.

4.1.2 Converter choice

At ETP, where this work was carried out, there is a wide range of power supplies that differ in power and frequency range in which they can operate. Below the list:

| Power supply | Active or apparent power | Min Frequency [kHz] | Max Frequency [kHz] |
|--------------------|--------------------------|---------------------|---------------------|
| Elotherm | 120 kW | 0 | 0.5 |
| AEG | 100 kVA | 0.3 | 1.5 |
| EMA-TEC Multi | 138 kVA | 0.4 | 40 |
| BBC | 200 kVA | 1.5 | 2 |
| EMA-TEC | 20 – 30 kW | 3 | 30 |
| HWG | ca. 50 kW | 5 | 15 |
| EMA (KIT) | 300 kW | 8 | 11 |
| Hüttinger | 20 kW | 30 | 300 |
| Himmelwerk HU | 100 kW | 40 | 200 |
| Elotherm (Skull) | 440 kW | 10 | 350 |
| Himmelwerk Exponat | 2 kW | 100 | 500 |
| Himmelwerk Sinus | 25 kW | 500 | 1200 |

In induction heating process, since material parameters change with temperature and field intensity, the inductance of the inductor – work-piece arrangement and, therefore also the resonant frequency change. This change needs to be picked up and evaluated, in order that the operating frequency of the power source must continuously track the resonant frequency of the resonant load.

Another aspect regards the generator control model. To ensure greater safety we'll always maintain constant the active power we're providing. The last model was again simulated, assuming now constant the active power and not the current. For this reason we expect a change in time of the current applied. We'll refer to an equivalent series circuit for representing the inductor – work-piece system. Equivalent circuit parameters are calculated from current, frequency, active and reactive power knowledge. Contrary to simulations shown in Chapter 3, now at each step a new resonance frequency is calculated. We refer to a parallel oscillating circuit (see Figure 4.4), in which resonance frequency values:

$$f_{rp} = \frac{1}{2\pi\sqrt{LC}}$$

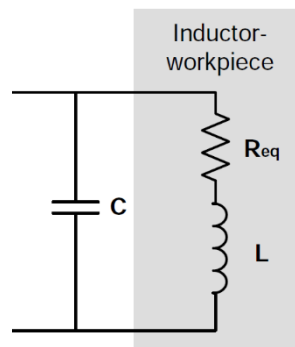


Figure 4.4. Parallel oscillating circuit

Considering a constant active power that feeds the system of 45kW and a capacitor bank of 250 μ F, in Figure 4.5 is possible to see how current and frequency vary.

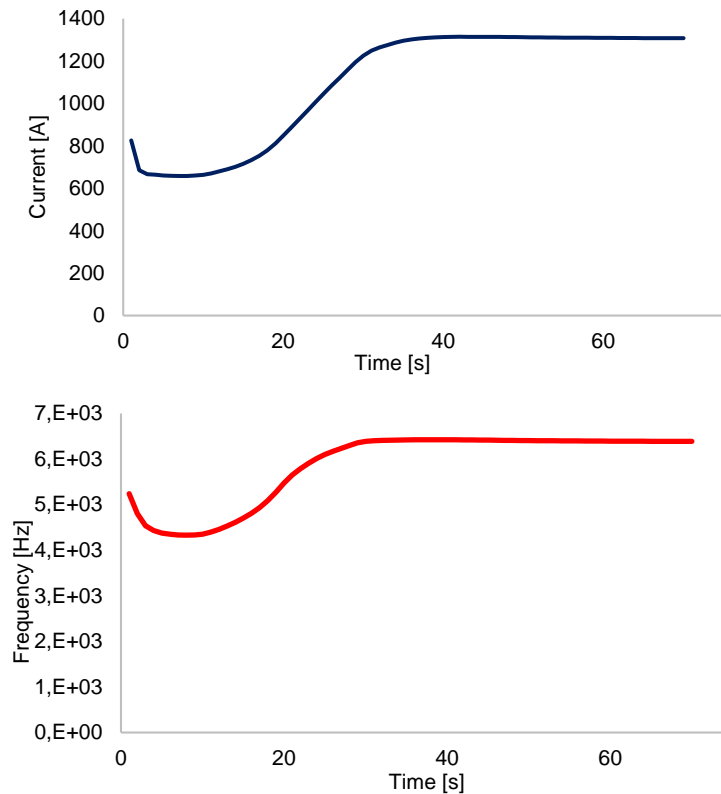


Figure 4.5. Current and resonance frequency in time with $P = 45$ kW

There are two converters that can satisfy our requirements in term of frequency: EMA – TEC Multi and EMA TEC. EMA TEC Multi was chosen because it allows to operate in a wider power field. It should also be pointed out that this power supply cannot operate continuously from 0.4 to 40 kHz. Not only there are some frequency ranges that are not permitted but also each configuration has an upper and lower limit. Configuration 5 best meets our requirements, which allows to operate between 3.49 and 8.49 kHz. EMA TEC Multi consists of a diodes rectifier, a voltage fed inverter, a transformer and a LCL tank. Other considerations regarding the structure and the functioning of EMA TEC Multi will be done in paragraph 4.4.



Figure 4.6. EMA TEC Multi

4.2 Inductor manufacturing

In the practical realization of the inductor appear new topics that are source of analysis. An example regards inductor ends shape and dimensions.

4.2.1 Diameter and thickness

At first it was calculated the tube length necessary to manufacture the inductor. Its length values round 5 meters. Since we are not taking into account inductor ends, we need to increase the length of one meter. Diameter and thickness in simulations value respectively 10 and 2 mm. Unfortunately there are not copper tubes available on the market with this shape, and a customised piece would be too expensive (8 times the normal cost). Since we didn't want to modify the external diameter, we decided to reduce the thickness to 1.5 mm. This is lower than the optimal value, and as a consequence joule losses will be higher than expected. With a current of 1000 A and a frequency of 4 kHz the increase in the losses is estimated around 10%.

When the copper tube was delivered, the diameter was larger than expected. It valued 10.7 mm instead of 10 mm. Two solutions were considered in order to obtain the same inductor length. The first idea was to reduce the air gap between turn and turn. Since in the hot areas gap between turns values up to 2 mm, it is not possible a further reduction. This means that the gaps reduction must be done in the cold areas, with the negative effect of reducing temperature differences between zones. This approach was abandoned. Since cold zones at the edges are not part of the investigation we preferred to remove the first and the last turn, keeping so the air gaps of the last model. The temperature profile in the hot zones is partially affected by this choice. In fact, although weakly, the temperature along the axis tends to be lower in the outer sides.

Thus, the inductor has 30 turns: 10 in each hot zones, 4 in the central cold zone and 3 at each edge. A sketch is represented in Figure 4.7.



Figure 4.7. 3D sketch of inductor and work-piece

4.2.2 Inductor ends

In a 2D axisymmetric numerical model there is no possibility of taking into account of inductor ends, i.e. the connection between coil and capacitor bank. Inductor ends are inductor 's parts highlighted in Figure 4.8.

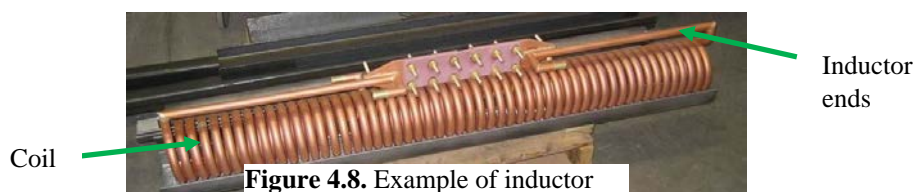


Figure 4.8. Example of inductor

Typically, in order to minimize the parasitic inductance due to the connections themselves, is minimum the area between coil and ends. In other words connections should be as close as possible to the coil, making sure they are not source of short circuits. In this case, for mechanical reason, the minimum distance between coil and ends is 30 mm. To be connected to the capacitor bank, connections were prolonged, keeping them as close as possible to each other, reducing so parasitic capacities. A minimum distance of 2 mm was kept and a layer of Teflon, one millimetre thick, was put in order to avoid short circuit. This final part of the inductor was 150 mm long.

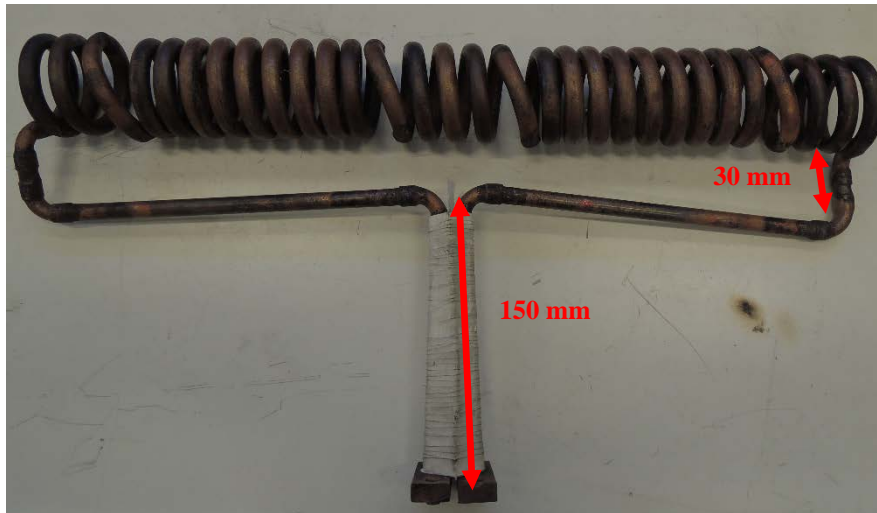


Figure 4.9. The inductor manufactured

It is, at the same time, interesting to know how inductor ends influence the magnetic field inside the coil. Some hypothesis are made:

1. The inductor is assumed empty, i.e. without work-piece.
2. The inductor has an infinitesimal thickness, i.e. it's modelled as a line.
3. The coil is a helix with constant pitch.

Recalling Biot-Savart law:
$$d\vec{B} = \frac{\mu_0}{4\pi} I \frac{d\vec{l} \times \vec{r}}{r^2}$$

Which permits to calculate the magnetic flux density dB generated by a conductor with infinitesimal length dl , supplied with a current I , at a distance r . Dividing the inductor in elements 0.4 mm long, it is possible to calculate the contribute of each element in a certain point. Referring to Figure 4.10, it is shown the magnetic flux density in P, due to an element in Q. In red we can see the current vector, and in yellow and green respectively, distance and magnetic flux density vector. It is worth noting that the flux density is perpendicular to the plane in which the distance and current vectors stay. From the all contributes sum it is possible to know the magnetic flux density in the desired point.

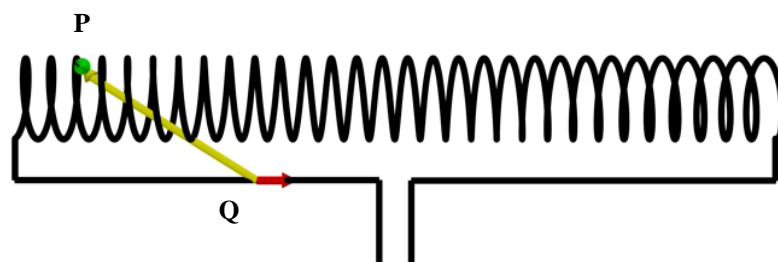


Figure 4.10. Explanation of Biot-Savart law application

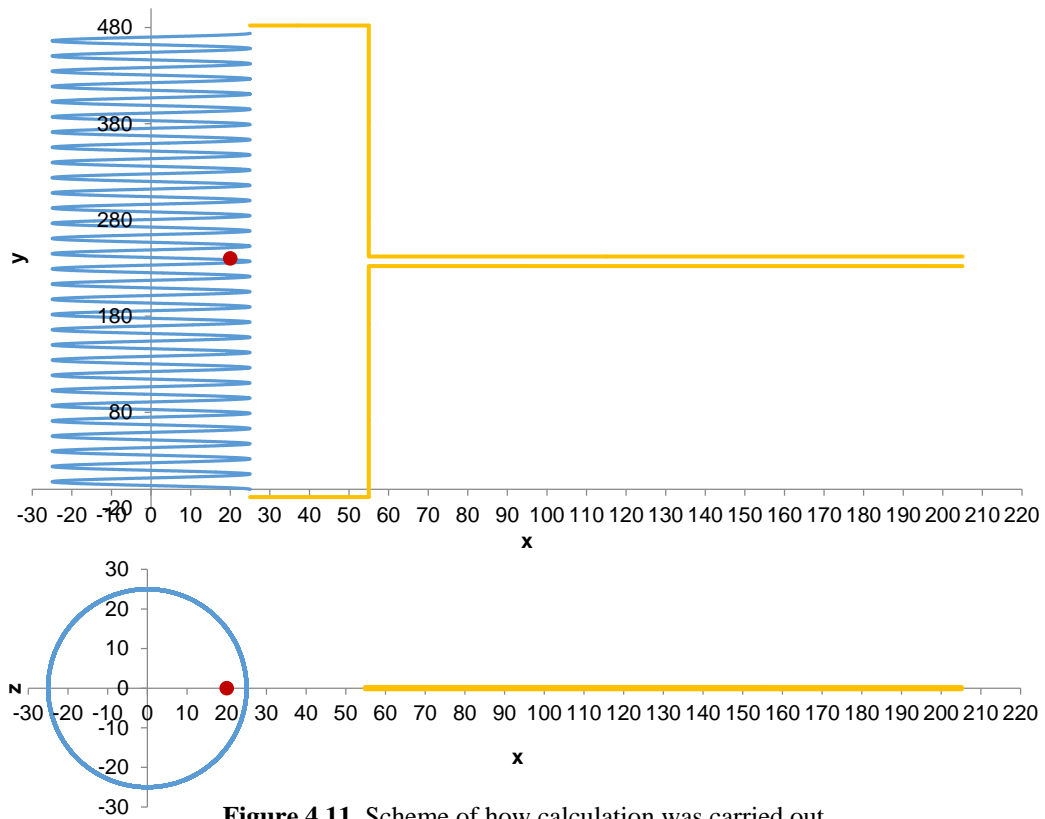


Figure 4.11. Scheme of how calculation was carried out

In Figure 4.11 is visible a graph that shows how the analysis was carried out. The first is referred to x-y plane, the second to x-z plane. The red dot indicates the point where magnetic flux density is calculated.

Results of this calculation are used to evaluate how magnetic flux density changes with and without inductor ends. In particular magnetic flux density was calculated inside the coil, in the plane where lay on feedings (x-y plane). We define the quantity:

$$\frac{dB}{B} = \frac{|B_{tot}| - |B_{coil}|}{|B_{coil}|}$$

$|B_{coil}|$ is the magnetic flux density module due to only to the coil (in blue in Fig. 4.11)

$|B_{tot}|$ is the magnetic flux density module that considers also inductor ends' contribute

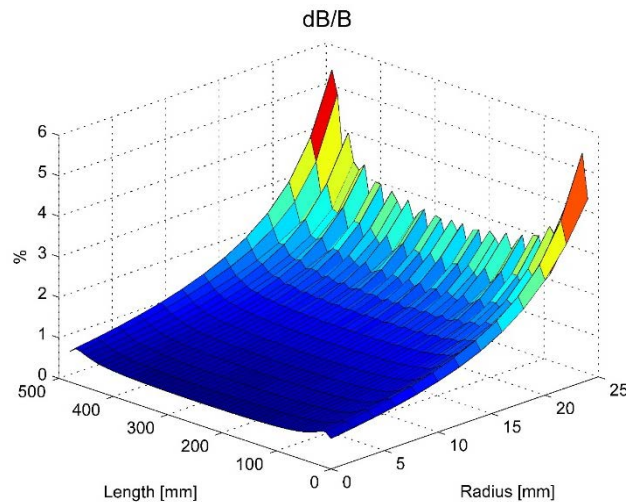


Figure 4.12. dB/B calculated inside the coil in x-y plane

The radius mentioned in Figure 4.12 is x axis of Figure 4.11. The length instead is y axis. Results show a weak influence of the connections inside the inductor, with dB/B bigger than 2% only at the edges. Despite the simplifying hypothesis adopted, this simple approach based only on Biot-Savart law, shows that the influence of inductor ends is negligible. It is also interesting to note that dB/B does not depend on the current apply and, it tends to increase when the number of turns is reduced. In other words more turns has the inductor, the less inductor ends modify the internal magnetic field distribution.

4.2.3 Insulation and support

In experiments, the aim is to heat up the work-piece until 1100 °C. Copper instead is water cooled and kept at a temperature round 25 °C. It is necessary a material, place between work-piece and inductor, that is able to reach high temperature, but at the same time it is a good electrical insulator. A ceramic material responds to these requests. The market offer is very wide in terms of type of ceramic material. A good compromise between cost and quality is offered by Alumina 94 (composed by 94% of Al₂O₃). It can reach a maximum temperature of 1750 °C and it has got a high electrical resistivity even if it is hot.

| | 25° | 500° | 1000° |
|-----------------------------------|-------------|----------------|----------------|
| Volume resistivity [Ω cm] | $> 10^{14}$ | $4 \cdot 10^9$ | $5 \cdot 10^5$ |

To allow temperature measurements with infrared camera and thermocouples, the work-piece cannot be all covered by ceramic. The solution adopted uses ceramic tubes, with 4 and 5 mm millimetre diameter positioned in the lower part of the body, in the space that separates it from the inductor (see Figure 4.13).



Figure 4.13. Ceramic tubes keep the work-piece at the centre of the inductor

The huge dimension of the inductor makes it flexible. Therefore it is necessary to support it along the length. As visible in Figure 4.13, the inductor with ceramic tubes and work-piece inside, it is placed on a table of refractory material.

4.2.4 Inductor cooling

As explained in the next paragraph experiments will be carried out with different power: 20, 30 and 40 kW. This is relative to the DC side of the power supply, in which are included inverter, cables and capacitor bank losses. Assuming zero these losses, and simulating the heating process with constant active power applied, power lost in the copper is maximum at the end of the heating, as it is understandable from current trend of Figure 4.5. Assuming

that active power is equal to 40 kW, inductor losses value not more than 8 kW. The purpose of this paragraph is to investigate if the cooling system is able to carry away the heat produced. We make the hypothesis to be in adiabatic conditions, i.e. all the heat is absorbed by the water.

In order to make the analysis simpler, we'll consider the inductor as a straight pipe. Assuming the water flow known, these are the input data:

| | |
|---|-----------------------|
| Heat produced (P) [kW] | 8 |
| Water flow (Q) [l/min] | 10 |
| Tube length (L) [mm] | 5000 |
| Tube diameter (D)[mm] | 7.7 |
| Specific heat (c_s) [J/kg °C] | 4180 |
| Density (γ) [kg/m ³] | 998 |
| Cinematic viscosity (ν) [m ² /s] | $1.004 \cdot 10^{-6}$ |
| Thermal conductivity (λ) [W/m °C] | 0.6 |

Parameters are evaluated at a temperature of 25 °C. The aim is to calculate the temperature difference between output and input, and the pressure drop due to the tube.

We start from the calculation of the average velocity.

$$v = \frac{4Q}{\pi d^2} = \frac{4 \cdot 10 \cdot 10^{-3}}{\pi (7.7 \cdot 10^{-3})^2} = 3.58 \text{ m/s}$$

Then are calculated three non-dimensional numbers. Reynolds number expresses the ratio between inertial and viscous forces. Prandtl number represents the ratio between cinematic diffusivity and thermal diffusivity. As last, Nusselt number indicates the proportion between the heat flow exchanged by convection and the heat flow exchanged by conduction.

$$Re = \frac{v D}{\nu} = \frac{3.58 \cdot 7.7 \cdot 10^{-3}}{1.004 \cdot 10^{-6}} = 27456$$

The high value found means that a fully turbulent flow is developed.

$$Pr = \frac{v \gamma c_s}{\lambda} = \frac{1.004 \cdot 10^{-6} \cdot 998 \cdot 4180}{0.6} = 6.98$$

In general $Nu = f(Re, Pr)$. In the case of a tube with fully turbulent conditions, Dittus-Boelter equation is used.

$$Nu = 0.023 Re^{0.8} Pr^{0.4} = 177.9$$

h - Heat exchange coefficient is thus calculable as:

$$h = \frac{Nu \lambda}{D} = \frac{177.9 \cdot 0.6}{7.7 \cdot 10^{-3}} = 13861 \frac{\text{W}}{\text{m}^2\text{K}}$$

It is possible to obtain the temperature difference between output and input:

$$\Delta T = \frac{P}{h S} = \frac{P}{h \cdot \pi D \cdot L} = \frac{8000}{13861 \cdot \pi \cdot 7.7 \cdot 10^{-3} \cdot 5} = 4.8 \text{ °C}$$

That is an acceptable value. Now is calculated the pressure drop due to the inductor. We start from Colebrook's formula, which permits to obtain Darcy coefficient of friction.

| | |
|-----------------------------------|------------------|
| Absolute roughness (ϵ) | 0.0015 10^{-3} |
| Darcy coefficient of friction (f) | |

$$\frac{1}{\sqrt{f}} = -2 \log \left(\frac{\epsilon/D}{3.71} + \frac{2.51}{\text{Re} \sqrt{f}} \right)$$

By iteration it possible to calculate f, that here is 0.02448.

$$\Delta p = f \frac{L v^2}{D 2} \gamma = 0.02448 \frac{5}{7.7 \cdot 10^{-3}} \frac{3.58^2}{2} 998 = 1.017 \cdot 10^5 = 1.01 \text{ atm}$$

Even if we are neglecting that the tube is a helix and we haven't taken into account that the system cools down generator and capacitor bank too, since it is able to provide a pressure up to 10 atm, it is adapt for experiment that will be carried out.

4.3 Laboratorial activities

4.3.1 Experimental setup

Experiments were carried out with three constant DC power fixed in the power supply: 20, 30 and 40 kW. The configuration chosen in the power supply permits to operate at a frequency between 3.49 and 8.49 kHz. Capacitors are adopted so that the system has a resonance frequency in the range allowed for each power. Four capacitors were used, for a total capacity of 160 μF .

Measurements made, concern thermal and electrical quantities. In particular will be discussed in detail active power measurement.



Figure 4.14. Experimental setup

Thermal quantities

Temperature knowledge plays a fundamental role in a heating process. The first idea was to measure the superficial temperature of the work-piece using an infrared camera. After several attempts this approach was abandoned. The difficulties were due to the lack of knowledge of the emissivity coefficient and the limited air space between turns. Then insulated thermo couples (K type) were used, which at first were just leaning on the piece. It was not a good solution because thermo couples tended too easily to move away from the work-piece, providing so a wrong measurement. Available thermocouples diameter varied between 0.5 and 2 mm. Since the cylinder heated is quite small, and a thermocouple is a cold body, it was better to use thermo elements with the minimum size. Only four insulated thermocouples with 0.5 mm diameter were available. In order to have a relative high number of measurement points, “self-made” thermocouples were manufactured. They were obtained using one cable made of Nickel and one of Nickel-Chromium. Wires were welded to one end, after that insulation was removed. Some drills (0.5 mm diameter - 2 mm deep) in the work-piece were made in which thermocouples can be put inside. In this way superficial temperature was known. A critical point of this measuring method is the fact that thermocouples are not isolated in the final part. If two “nude” wires come in contact, the measurement is wrong, and if they touch the coil, they get damaged. This was avoided using Teflon tape, which was frequently replaced because it tended to burn.



Figure 4.15. Thermocouples and Teflon tape insulation

Because the piece has been subjected to numerous heating and cooling processes, the surfaces released material flakes obstructing the holes for the thermal measurements. The piece has been subjected to periodic cleaning using a sandblaster. In Figure 4.16 is shown the cylinder before and after sandblasting.

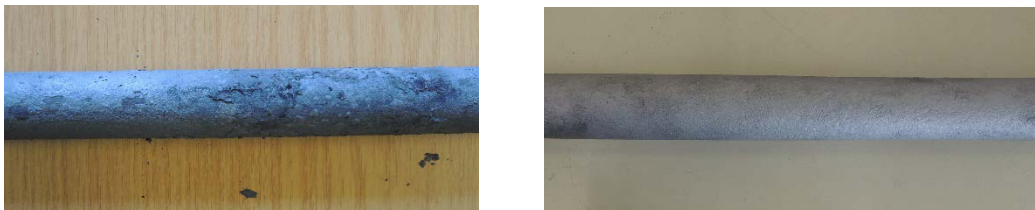


Figure 4.16 Work-piece before and after sandblasting

Electrical quantities

In the power supply there was the possibility to fix the active power in the DC side and, at the same time, to know voltage and current. But this did not give any information about the current and the voltage applied to the resonant circuit. Voltage difference along the inductor and frequency were measured by a multimeter able to sample every second. Current flowing in the inductor is known through the use of a Rogowski coil connected to another multimeter. Even in this case the sample rate is one second. Both tools work with true RMS.

For active power knowledge, current and voltage probes were connected to an oscilloscope in order to know their waveforms. Current probes were connected in such a way that the conductor is as close as possible to the coil centre (Figure 4.17). Since the inductor is potential free and the oscilloscope needs to be grounded, galvanic insulation is required in the voltage measurement. In order do that, a particular voltage probe was used.

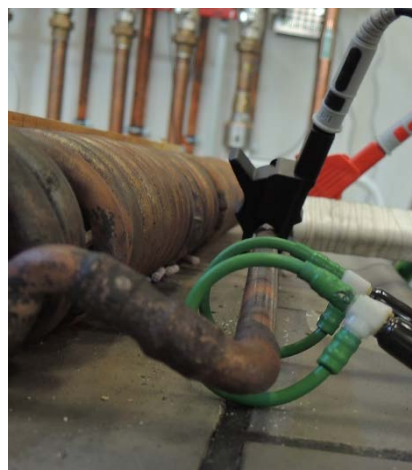


Figure 4.17. Voltage and current probes

4.3.2 Electrical results

As already anticipated, we consider three different heating processes. In each, a different constant active power is considered in the inverter DC side: 20, 30 and 40 kW.

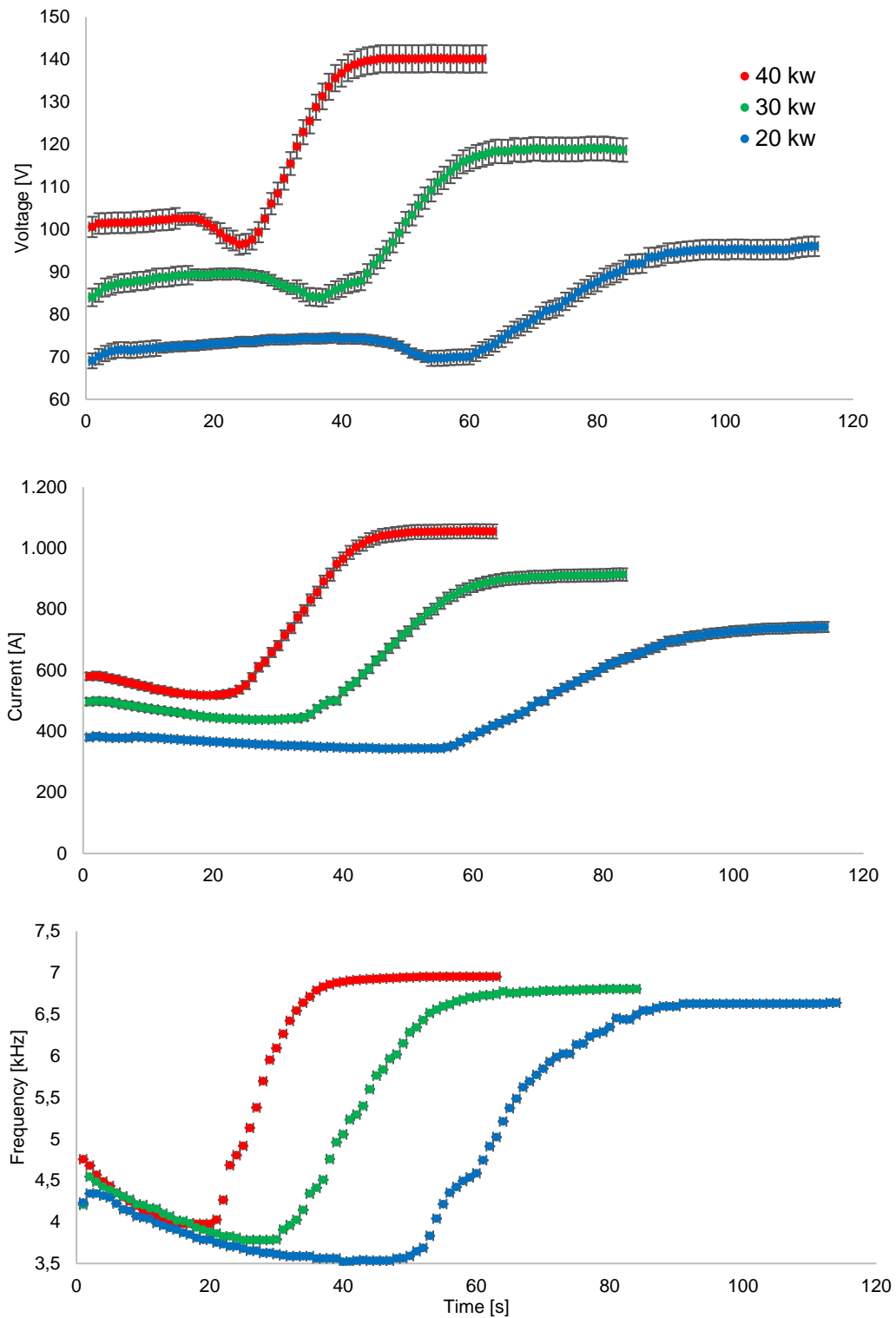


Figure 4.18. Voltage, current and frequency in time with 40, 30 and 20 kW

At the beginning of the process up to Curie point, current tends to decrease instead the voltage is quite constant. This means that for providing the same power, less apparent

power is necessary. In other words power factor, weakly increases. Because of the change of material properties, after Curie point, the power factor falls. Final current and voltage are much higher than their initial values.

There is a lower frequency limit of 3.49 kHz, below which the transmitted power cannot be higher than 10 kW. Adopting a total capacity of 160 μ F, the resonance is maintained in the range permitted in every configuration. The dependence of the resonance frequency with the applied power means that the equivalent inductance of the load-cylinder system depends on the current. It is the confirmation that the magnetic permeability is function of the magnetic field.

As expectable if we increase the power, it is necessary less time to heat up the work-piece. It should be noted that the final temperatures reached are not the same. They are almost equal in the first and second heating: 1150 °C and 1115 °C with 40 kW and 30 kW respectively. In the third case instead the body reaches only 957 °C. With 20 kW the heating time is less than twice the time with 40 kW.

| P_{DC} | Maximum temperature [°C] | Heating time [s] | DC energy [kWh] |
|----------|--------------------------|------------------|-----------------|
| 40 kW | 1150 | 62 | 0.689 |
| 30 kW | 1115 | 84 | 0.700 |
| 20 kW | 957 | 115 | 0.639 |

The energy consumption calculated as “DC energy” is the power and heating time product. This value is the sum of three quantities: electrical energy provided to the work-piece, energy lost in the copper and energy lost between inverter and inductor (in the cables, capacities and transformer).

4.3.3 Electrical power measurement

The aim of this paragraph is to calculate the electrical energy absorbed by the inductor-work-piece system. Three different approaches are presented, showing pros and cons.

First approach

The idea is to use an oscilloscope that measures current and voltage waveforms. From what is visible it is possible to know the interval of time that separates voltage and current consecutive zero-crossing. The phase shift between voltage and current is calculable as:

$$\varphi = 2\pi \frac{\Delta t}{T}$$

where Δt is the time length between voltage and current consecutive zero-crossing [s] and T is a period time length [s].

The active power is calculable as:

$$P = V_0 I \cos \varphi$$

With V_0 inductor voltage rms [V], I inductor current rms [A]. These quantities are measurable with an oscilloscope or with a multimeter. In the first case this is possible, for example, from the peak to peak distance wave knowledge.

This approach works only with sinusoidal conditions, as implied in the two formulas above. Power factor is equal to $\cos \varphi$ only in this case. Moreover, rms quantity from the oscilloscope is obtained dividing by $\sqrt{2}$ the wave peak value. This operation is feasible only in the case of a sinus.

Analysing, in this experiments, the inductor current and voltage wave-forms, it is visible that they are not sinusoidal at the beginning of the heating. Voltage in particular. The assumption of being in sinusoidal conditions is too strong. Besides, this method is not compatible with fast changing of the power factor, as occurs in an induction heating process around the Curie temperature. This method was so abandoned.

Second approach

This second measurement approach is so called “three ampere-meters method”. It permits to know how much active power is absorbed by the system, starting from three current measures. One of the advantages is the non-necessity of an oscilloscope, and the fact that the measure is based on the knowledge of three effective values. All this is verified in sinusoidal conditions. Even if this hypothesis is not completely verified, it is worth to explain this method in more detail.

Three currents are measured: the current in the load, the current absorbed by a capacitor in parallel and the sum of this two (see Figure 4.19). This third measure is not overabundant because rms is not known.

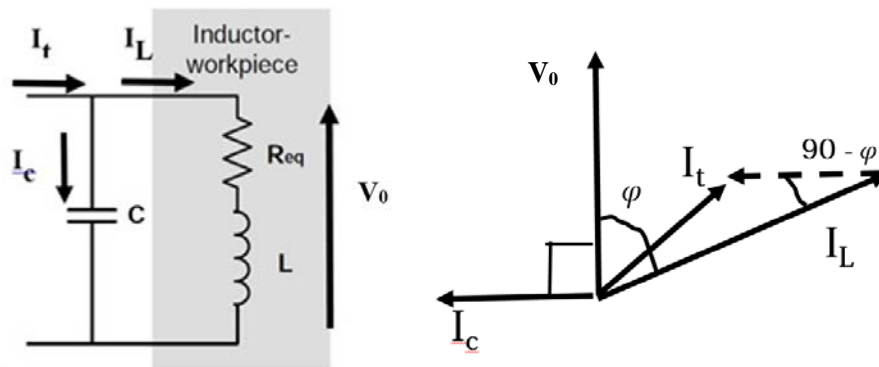


Figure 4.19. Three ampere-meters method

Voltage and current are represented as phasors. In a capacitor current leads the voltage by 90° . In an ohmic-inductive circuit current leads the voltage by an angle φ . From Kirchhoff law:

$$i_t(t) = i_L(t) + i_c(t)$$

i.e. three currents form a triangle. When all three sides of a triangle are known, it is possible to calculate its angles by using the theorem of Carnot.

$$I_t = I_c + I_L - 2 I_c I_L \cos (90-\varphi)$$

Where I_t , I_c and I_L are the effective values. Thus active power is calculable as:

$$P = V_0 I \cos \varphi$$

Even if sinusoidal conditions are verified, this approach is very sensitive to the capacitor current value. To show this fact, an example is purposed. We consider typical values met in our experiments.

| | |
|------------------------------|-------|
| Frequency [kHz] | 5 |
| C [μ F] | 21 |
| R _{eq} [Ω] | 0.1 |
| L [μ H] | 6 |
| cos φ | 0.470 |
| V ₀ [V] | 120 |

If we assume to know exactly I_t and I_L and we commit a mistake of 5 A in the knowledge of the current that flows in the capacitor, cos φ is 0.542. An extremely different value compared to the real one. This also occurs because the power factor, in this type of processes, is always rather low.

In our setup, different Rogowski coils were used, compatible with dimensions and shape of the elements where the current flows.



Figure 4.20. I_t measure

I_t and I_c measures were carried out with big Rogowski coils, different to that one used in the inductor. In Figure 4.20 is visible how I_t was measured. Two capacitor banks were connected in parallel and in the second one there was only one capacitor (21 μ F). In this way the current that flows in the bridge that connects the two banks is I_t . The current instead that circulates in the capacitor was measured closing the probe around the capacitor itself.

Despite several attempts this method has not been successful. The reason is to be found in the diversity of the probes, in addition to the weaknesses of the method presented before. For example measuring the same current with these three probes, gave very different results (up to 7%). It was also introduced a corrective proportional factor, so that the same current was measured in the same way. Unfortunately, even in this case, results were not reliable.

Third approach

This third approach is, from the theoretical point of view, similar to the first. But it has the great advantage that it can be applied for each waveform of voltage and current. The idea is to record inductor voltage and current waveforms and to integrate their product in order to obtain the active power. In other words it is simulated what happens in a wattmeter.

This procedure is possible using an oscilloscope that can save voltage and current tracks. This is not possible in a continuous way. With the oscilloscope used, a Key Sight® DSO-X 2004A, current and voltage shapes were recorded every three seconds, the time necessary

for saving data. Each curve has 2000 points, which means, in our case, a time distance between two points of 0.125 μ s. The number of points can be increased or decreased, depending on whether it is preferable higher resolution or more frequent sampling.

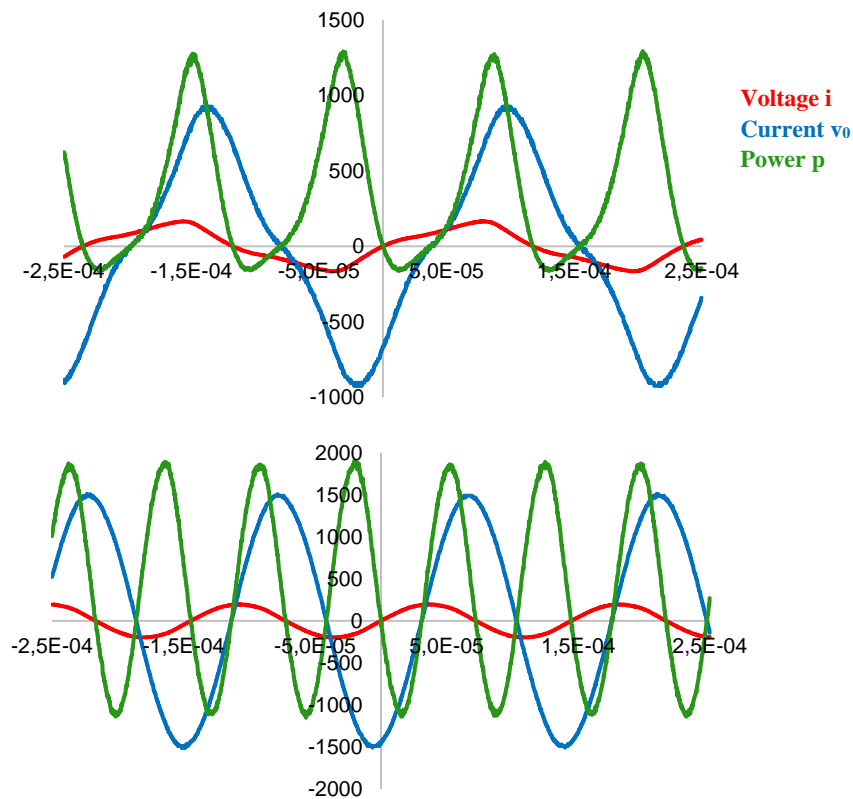


Figure 4.21. Current, voltage and instant power after 9 and 52 seconds ($P_{DC} = 40$ kW)

In Figure 4.21 is possible to see voltage, current and power at different instants of the process. The power, obtained as product between current and voltage, is not scaled. The first and second graph are relative to quantities evaluated after 9 and 52 seconds respectively. At the beginning of the heating (after 9 seconds) here is shown what already anticipated before, i.e. sinusoidal conditions are not respected. With the hot work-piece (after 52 seconds) current and voltage are both sinusoidal. From the two pictures is also visible that the frequency grows, because in the second image, with the same time scale, there are more periods. Last consideration is relative to the power factor. It is lower at the end of the heating because, if the instant power is integrated, the area below time axis is much higher in the second graph of Figure 4.21. In other words, voltage-current phase shift is bigger.

The active power is obtained by the integration of the instantaneous power in a finite number of periods.

$$P = \frac{1}{NT} \int_{NT} v_0(t)i(t)dt$$

Where N is a natural number, and T the period [s].

In Figure 4.22 are visible active power and power factor trend. “P” is the sum of the power induced in the work-piece and the inductor losses. It tends weakly to decrease because of the current growth. Power factor is by definition:

$$\text{Power factor} = \frac{P}{V_0 I}$$

At the end of the heating it is three times lower than the initial value.

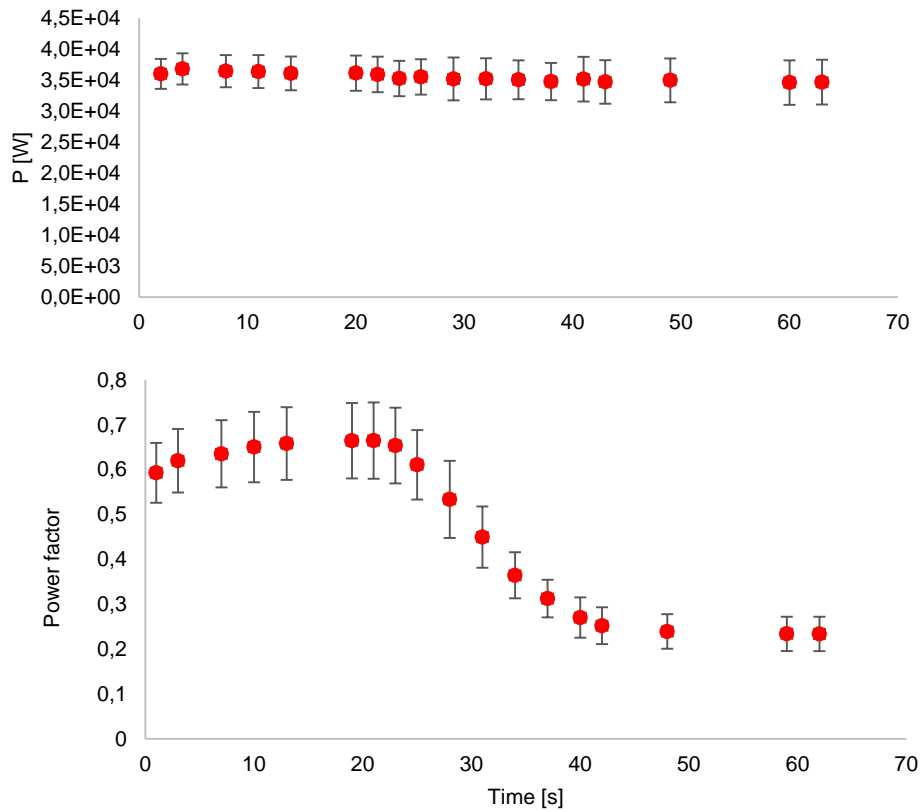


Figure 4.22. Active power and power factor of the inductor-workpiece system ($P_{dc} = 40$ kW)

Measurement uncertainty is calculated in the “worst case”. We assume that voltage and current uncertainty measured with the oscilloscope is equal to $1/20^{\text{th}}$ of division. The power factor relative uncertainty is calculated as:

$$\frac{u(\text{PF})}{\text{PF}} = \frac{u(P)}{P} + \frac{u(V_0)}{V_0} + \frac{u(I)}{I}$$

In $u(P)/P$ not only is considered uncertainty on the voltage and current measured but also in the time scale. This is estimated to be equal to the distance of time that separates two sampled points.

This analysis has the aim to calculate the electrical energy absorbed during the all process. Two approaches are considered. The first idea (*) is to integrate in time the active power results obtained with the oscilloscope. Since active power is known every three seconds typically, a linear interpolation between points is assumed. The second method (**) instead, uses voltage and current data recorded with multimeter, which are sampled every second. In this case a linear interpolation is hypothesized between power factor known points. As shown in the table, the difference between the results is quite small. It should be noted that this is the sum of the energy induced in the piece and that lost in the copper.

| P_{DC} [kW] | 40 | 30 | 20 |
|--------------------------|-------------|-------------|-------------|
| Maximum temperature [°C] | 1150 | 1115 | 957 |
| Energy DC [kWh] | 0.689 | 0.700 | 0.639 |
| Energy* [kWh] | 0.611±0.064 | 0.615±0.068 | 0.542±0.067 |
| Energy** [kWh] | 0.614±0.120 | 0.614±0.122 | 0.540±0.118 |

It's hard to evaluate the measurement uncertainty relative to the DC energy, because the value is a power supply control output.

Our purpose now is to calculate the electrical efficiency as:

$$\eta_e = \frac{\text{Electrical energy in the work-piece}}{\text{Energy DC}}$$

In order to know the power lost in the copper, three measurements were made without the work-piece. Changing the capacities connected and recording current and voltage waveforms with the oscilloscope it possible to estimate copper losses at different frequencies. In this way we assume that the current distribution in the inductor does not change with or without the work-piece. It is a strong hypothesis, but it permits to carry out the analysis. Follow measurements and results.

| | | | |
|-----------------------------------|-----------------|-----------------|-----------------|
| Capacitors [μF] | 174 | 259 | 344 |
| Resonance frequency [kHz] | 6.07 | 4.90 | 4.23 |
| I [A] | 1045 \pm 25 | 1082 \pm 25 | 1125 \pm 25 |
| P [kW] | 5.87 \pm 0.59 | 5.47 \pm 0.57 | 5.71 \pm 0.59 |
| R _{copper} [m Ω] | 5.37 \pm 0.80 | 4.67 \pm 0.70 | 4.51 \pm 0.67 |

To simplify the analysis we assume that the equivalent resistance that describes the inductor is constant with frequency. Its value is the average of the three calculated above.

$$R_{\text{copper}} = (4.85 \pm 0.80) \text{ m}\Omega$$

The energy lost in the inductor is calculable as:

$$E_{\text{copper}} = \int_{\Delta t} R_{\text{coil}} I^2 dt$$

Finally we are able to calculate electrical efficiency:

$$\eta_e = \frac{(\text{Energy}^* + \text{Energy}^{**})/2 - E_{\text{copper}}}{\text{Energy DC}}$$

| | | | |
|----------------------|-------|-------|-------|
| P _{DC} [kW] | 40 | 30 | 20 |
| η_e | 80.7% | 79.3% | 78.9% |

It tends to be higher with faster heating processes, as occurs when the power applied is bigger. This result only partly reflects the power supply effect, since we are referring to the DC power in the inverter. A more rigorous review should start from the power absorbed from the grid.

Last consideration of this paragraph pertains to the possibility of using this approach for measuring active power in high frequency applications. If the idea of integrating current and voltage product could work, there is one point that can be critical. It is relative to the use of Rogowski coil for measuring current. A Rogowski belt in fact behaves like the secondary of a transformer and it has its own inductance. In our experiments, with frequency between 4 and 6 kHz, the phase shift introduced was below the oscilloscope sensitivity, but with high frequency this could not happen.

4.3.4 Thermal results and comparison

In this paragraph are shown temperature measurements that were carried out. A total number of fourteen thermocouples were used, distributed along the work-piece length for measuring the surface temperature. Wrong results, caused by reverse polarity or shortcuts in thermocouples, are deleted. For this reason, sometimes, the number of measurements is lower than fourteen.

In graphs of Figure 4.23 is shown the comparison between thermal measurements and numerical simulations. Three images are relative to different power applied.

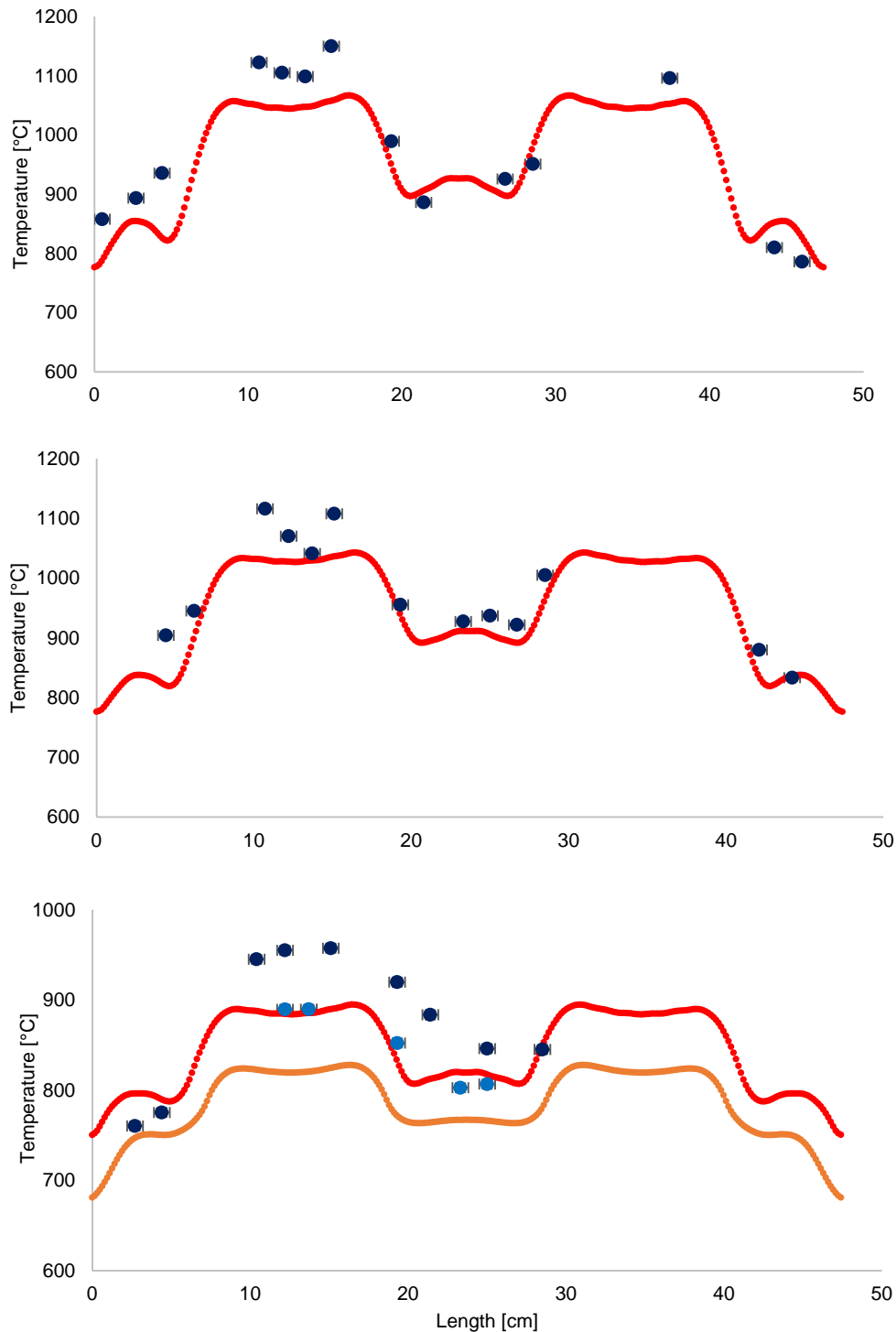


Figure 4.23. Final temperature profile in the case of P_{DC} equal to 40, 30 and 20 kW

Observing final temperature profiles we can say that the goal has been reached. There are two evident hot zones, with in the middle a cold zone (see also Figure 4.24).



Figure 4.24. Work-piece between 700 and 1000 °C

Temperature difference between zones tends to decrease if lower power is applied. With 40 kW it values 200 °C, which well satisfies our initial purpose. With P_{DC} equal to 20 kW instead, the heating time is so high that equalization effect is strong. Here the difference between hot and cold area is not more than 100 °C.

It also visible a certain asymmetry in the temperature profile, because the “left” side is hotter than the “right” side of the cylinder. The cause of this is the non-symmetry of the inductor, which creates a force that moves the piece horizontally during the process. To limit this effect some ceramic tubes were wedged between cylinder and inductor. Their deterioration and consequent breakup, due to frequent heating and fast cooling, made them less effective. The translational forces were not so completely balanced.

Only in the last experiment was measured core temperature in five points. This has been possible only using insulated thermocouples. Surface-centre temperature difference oscillates between 30 and 60 °C. Values for sure higher to those seen in Chapter 3. The cause is the too high frequency at which the heating takes place. A possible solution is the use of another generator, more suitable to the optimal frequency range. Another provides to resort to soaking after the heating.

Numerical simulations here presented were calculated after experiments. It was assumed constant the active power but unlike what was done in paragraph 4.1.2, the applied value is net of losses between inverter and inductor. The mistake that commits the model is in the range of 10 – 80 °C in the final temperature. If we compare in one point of the hot zone the temperature measured and simulated:

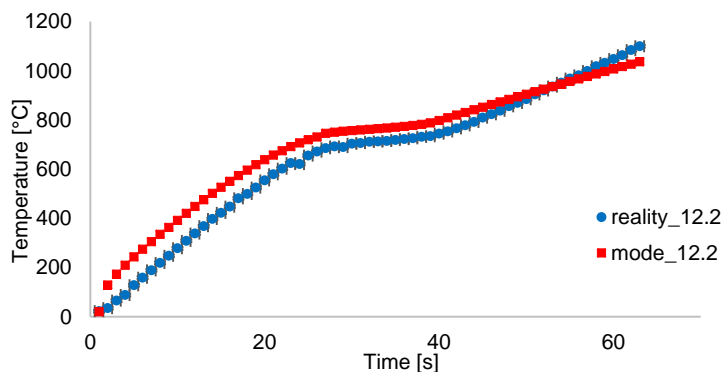


Figure 4.25. Measurement (○) – numerical result (□) comparison

In the hot zone the model (red) is “faster” than reality (blue) below Curie point, and it is “slower” above. This is due to not exact knowledge of material properties and other parameters, like the emissivity which is difficult to evaluate because it depends also on the surface roughness and temperature. It should be also noted that the numerical model used is two dimensional. Moreover, the resonance frequency calculated in numerical solution does not keep into account of capacities and inductances in cables, bars and feeding that there are in real application. For this reason it is always higher than the real one. In the case of cold zones instead, numerical results approximate quite well temperatures measured.

4.4 Simulating EMA TEC

Starting from active power measurements it is possible to obtain a series equivalent circuit able to describe the inductor – work-piece system. With these informations we can simulate the entire system from the electrical point of view. It is good a tool to estimate, for example, which current flows inside a semiconductor. The software used is PSPICE®.

In Figure 4.27 is visible the complete equivalent circuit. Power is absorbed by the grid through bars, here represented with an equivalent series resistance – inductance circuit. Then there is a non-controlled diodes rectifier. Follows a series inductance that acts as filter, and many capacitors in parallel for providing a constant voltage. There are also some resistors to allow capacitors discharge. The DC side feeds a voltage fed inverter that uses IGBT. Switches' frequency is equal to the resonance one. In particular, this power supply can operate with an output frequency that goes between 0.4 and 40 kHz. After the inverter there is a LCL tank. In the configuration used, series inductance values 40 μ H. There are also a capacitor and a small resistor that act as a snubber. A further inductance is due a transformer between capacitor bank and inverter.

In order to simplify the analysis the scheme was separated into two parts. The first is relative to AC/DC conversion. It goes from the grid, to the capacitors filter. The DC output voltage is really flat and has no ripples. The second circuit describes the DC/AC side and goes from the inverter, supplied with a DC voltage source, to the load.

Each diode is supposed to have an own resistance of 0.1 m Ω . Every switch is so designed:

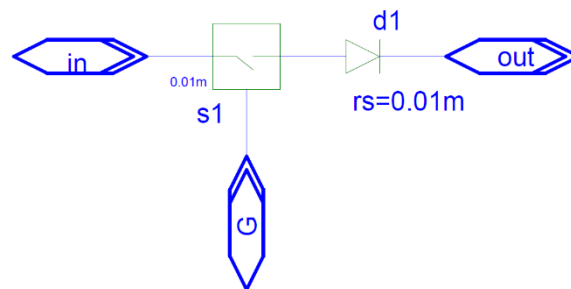


Figure 4.26. Switch (IGBT) internal design

It is possible to control the time that it closed and opened acting on the gate. The addition of a diode, not present in reality, is a way to guarantee that current flows only in one direction. The matching transformer in this circuit is supposed ideal.

The control system must never allow that two switches in the same leg are closed. With reference to the names used in Figure 4.28, are alternately closed A1 – A4 or A2 – A3 to avoid this situation. The control of the power is obtained modifying the duty cycle, i.e., the period of time in which switches are closed.

The circuit simulated refers to a real situation, relative to the heating with P_{DC} equal to 40kW. Here input data.

| | |
|---------------------------|-------|
| Resonance frequency [kHz] | 6.91 |
| R_{eq} [m Ω] | 31.78 |
| L [μ H] | 2.969 |
| V_{DC} [V] | 538 |

Applying to the inverter V_{DC} , known the switching frequency and the equivalent parameters of the load, duty cycle was modified in order to obtain electrical results that best fit measurements.

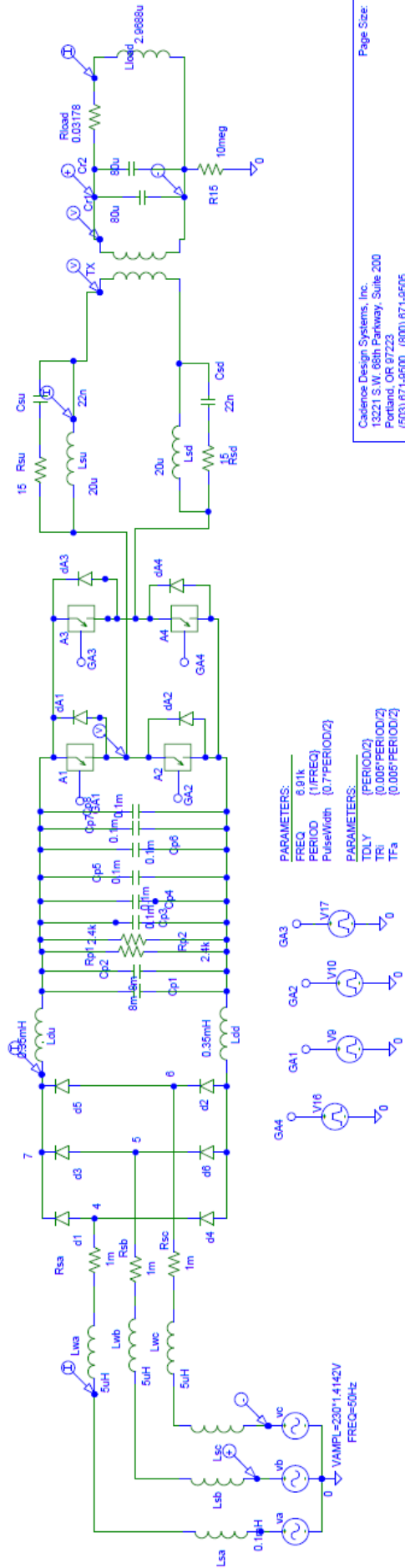


Figure 4.27. Complete equivalent circuit

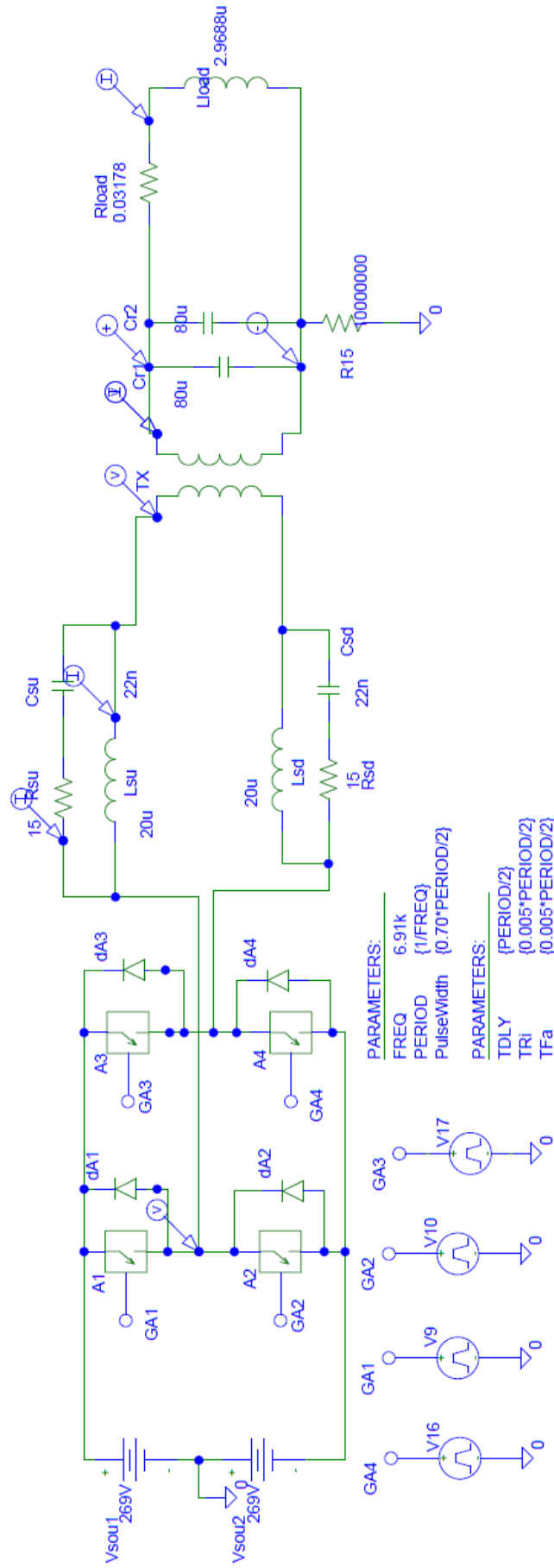


Figure 4.28. DC/AC conversion. Constant voltage is provided with a DC source

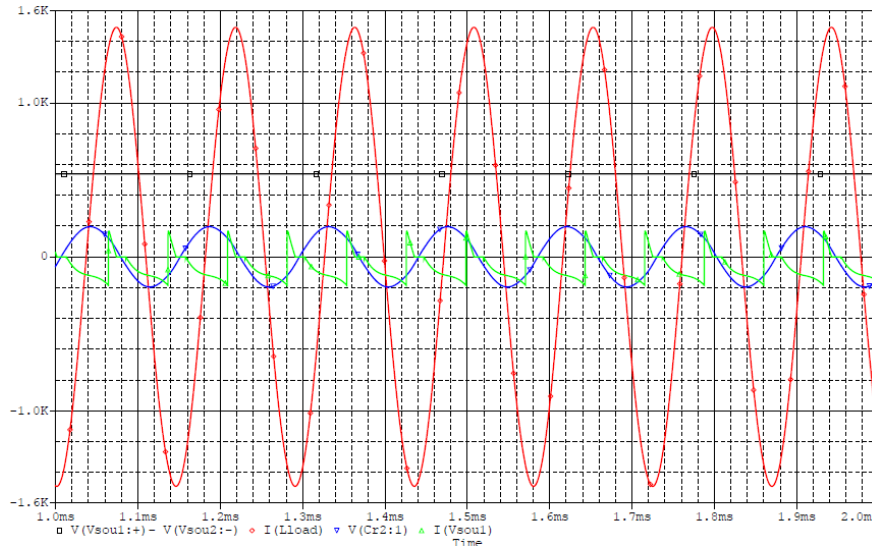


Figure 4.29. PSPICE® simulation waveform results

Trying several times it was found that numerical results approximate quite well what was measured with a duty cycle of 0.70. With input showed in the table above, here the comparison between current and voltage in the load.

| | Measured | Simulated |
|--------------------|----------|-----------|
| I [A] | 1049 | 1042 |
| V ₀ [V] | 139.4 | 138.7 |

This confirms that the model is a good approximation of reality. Also the current in the inverter DC side, measured and simulated, shows a great similarity.

5. Summary

This project carried out at ETP, Hannover Institute of Electroheating, has the main aim to show the possibility of providing a non-homogeneous heating with a technology relatively simple. In fact, even using one inductor it is possible to concentrate heat sources in desired zones. This permits not only to avoid expensive machines required in pre-forming processes, but also to save energy. Moreover, localized heat sources improve the efficiency, electrical and thermal, because the heating time is generally lower. In this model the increase of efficiency is equal to 4.8% respect to a traditional homogeneous heating.

The topic is still at an earlier stage of research also because the industry has not expressed interest yet. The use of only one inductor is easy, inexpensive, and permits to reduce the current necessary. But it is also a limit. First because the coil is designed for a single work-piece, it would be difficult to use with other bodies to be heated. Second because using several inductors it is easier to concentrate power if it is possible to control them during the heating. An evolution of this project could also involve the analysis of more complex geometry as that shown in Figure 5.1.

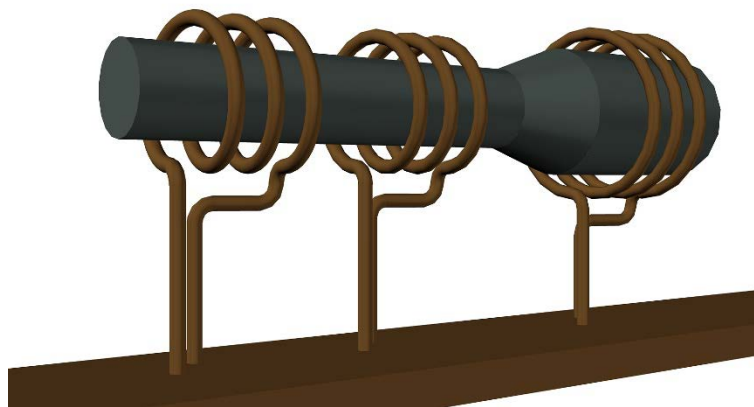


Figure 5.1. Inhomogeneous heating using three inductors with more complex work-piece geometry

A challenging aspect is related to the desire of finding relations which permit to design coarsely the inductor shape starting from the work-piece geometry and the desired number of hot and cold zones. In any case this will hardly replace the use of numerical simulations.

Bibliography

- [1] S. Lupi, “Appunti di Elettrotermia”, A.A 2005 – 2006
- [2] V. Rudnev, D. Loveless, R. Cook, “Handbook of induction heating”, Dekker, 2003
- [3] Schuler, “Metal Forming Handbook”, Springer – Verlag Berlin Heidelberg 1998
- [4] E. Baake, M. Mach, “Increasing the variability of warm forging processes by implementation of intermediate induction heating”, Proceedings of the XII International Conference on Complex Systems: Control and Modelling Problems, Samara (Russia) June 2011,
- [5] O. Okman, “Free forming of locally induction heated specimens”, March 2005
- [6] M. Schwenk, “Numerische modellierung der induktiven ein- und zwei-frequenzrandschichthärtung”, Scientific Publishing, July 2012
- [7] Ansys, “Low-frequency electromagnetic analysis guide”, April 2009
- [8] Ansys, “Thermal analysis guide”, April 2009
- [9] M. Fiorindo, N. Sempreboni, M. Tollardo, “Computational Electrical Engineering”, August 2014
- [10] R. Bargallo, “Finite elements for electrical engineering”, Universitat Politcnica de Catalunya, 2006
- [11] D. Meelab, O. Longeot, L. Krähenbühl, L. Nicolas, P. Wendling, “Control of an induction heat treatment by the measure of the power”, IEEE Transaction on Magnetics, Institute of Electrical and Electronics Engineers, 1993
- [12] E. Zok, D. Schinisch, “Energy-efficient power supply for induction hardening and heating process”, 2013
- [13] G. Segura, “Induction heating converter’s design, control and modelling applied to continuous wire heating”, Universitat Politcnica de Catalunya, 2012
- [14] S. Dieckerhoff, M. Ryan, R. De Doncker, “Design of an IGBT-based-LCL-Resonant Inverter for High-Frequency Induction Heating”
- [15] “International induction heating seminar”, Padova 1998

List of figures

| | |
|---|----|
| 1.1 Open die forging a) Start of the process b) partial deformation c) final shape | 13 |
| 1.2 Open die forging in the case of “inhomogeneous” heating | 14 |
| 1.3 Explanatory sketch of how to get a differentiated heating in the axial direction | 15 |
| 1.4 Macro scheme that shows how the investigation has been carried out | 15 |
| 2.1 Typical layout with inductor, workpiece and trend of magnetic field lines | 18 |
| 2.2 Skin effect in a conductor | 18 |
| 2.3 The proximity effect | 19 |
| 2.4 Magnetic flux lines with the same or opposed currents direction | 19 |
| 2.5 Examples of configuration inductor-load | 20 |
| 2.6 Solid state components as a function of frequency [Hz] and capacity [VA] | 21 |
| 2.7 Principal component of an induction heating installation | 21 |
| 2.8 Sketch of inductor and cylindrical work-piece | 22 |
| 2.9 First and second type Bessel functions | 24 |
| 2.10 Magnetic field module trend inside the work-piece | 25 |
| 2.11 Current density function of ξ and m | 26 |
| 2.12 Values of P and Q , as a function of m | 26 |
| 2.13 How current density changes with $f = 400$ Hz or $f = 3600$ Hz | 27 |
| 2.14 Power induced inside the work-piece | 27 |
| 2.15 Current density and induced power inside an infinite semi plane | 30 |
| 2.16 Configuration of an hollow cylinder with a longitudinal magnetic field | 32 |
| 2.17 Coefficients for the calculation of the active and reactive power in a tube heated from the inside | 34 |
| 2.18 Parameters that represent active and reactive power in the coil | 35 |
| 2.19 Electrical efficiency | 36 |
| 2.20 Merit and power factor with different values of “ m ” | 37 |
| 2.21 Difference of temperature with the axis, changing “ m ” | 40 |
| 2.22 Values of $F(m)$, $F'(m)$ and $F''(m)$ | 41 |
| 2.23 Thermal transient in a uniform heating of no magnetic load, without superficial losses | 42 |
| 2.24 Correction factor for the surface’s losses | 42 |
| 2.25 How resistivity changes in different materials | 44 |
| 2.26 Dependency of the relative magnetic permeability on temperature and H | 44 |
| 2.27 How to evaluate the thermal transient for carbon steels | 45 |
| 2.28 Variation of the specific power in the case of carbon steel | 46 |
| 2.29 Permeability distribution in a ferromagnetic field | 46 |
| 2.30 Qualitative distribution of the current density in the magnetic [2] and non-magnetic [1] layer at the exceeding of the Curie point | 47 |
| 3.1 Flux diagram of pre-processing | 54 |
| 3.2 Example of an axisymmetric body | 54 |
| 3.3 Flux diagram of the complete script | 57 |

| | | |
|------|--|-----|
| 3.4 | Electrical resistivity | 58 |
| 3.5 | $\mu - H - T$ curves | 59 |
| 3.6 | 42CrMo4 thermal conductivity function of temperature | 59 |
| 3.7 | How specific heat capacity changes with temperature | 60 |
| 3.8 | Penetration depth [mm] as a function of temperature | 60 |
| 3.9 | Mesh. On the left the work-piece, on the right one turn | 60 |
| 3.10 | Air box dimensions | 61 |
| 3.11 | $\mu - T$ curves for different magnetic fields | 61 |
| 3.12 | Sketch of the goal (a) and possible final temperature distribution (b) | 63 |
| 3.13 | Limits of frequency as a function of diameter for heating of carbon steel billets until 1200°C | 65 |
| 3.14 | Sketch of which lengths are considered | 67 |
| 3.15 | Given a final temperature profile (dots), how to evaluate R | 67 |
| 3.16 | Geometry of the first model | 68 |
| 3.17 | Thermal results with 96 s heating time | 69 |
| 3.18 | Second model geometry | 70 |
| 3.19 | Thermal results relative to the second model | 71 |
| 3.20 | Geometry of the third model | 72 |
| 3.21 | Thermal results with 78 s heating time | 73 |
| 3.22 | Projection of geometry of fourth model | 74 |
| 3.23 | Thermal results with 78 s heating time in the case of the fourth model | 75 |
| 3.24 | Inductor (axisymmetric model) with fixed (A) and changing (B) air gap | 77 |
| 3.25 | Magnetic field module distribution in case (A) and (B) | 77 |
| 3.26 | Geometry of the last model | 78 |
| 3.27 | Active power trend | 78 |
| 3.28 | Cos phi trend in time | 79 |
| 3.29 | Magnetic field module distribution in the hot zone after 2 and 80 s | 79 |
| 3.30 | Thermal results with 80 s heating time | 80 |
| 3.31 | Temperature at surface and core in time, evaluated in the hot and cold zone | 81 |
| 3.32 | Geometry and final temperature profile in case of inhomogeneous and homogeneous heating | 82 |
| 3.33 | Specific heat c_p and equivalent specific heat c_s | 83 |
| 3.34 | Sketch of the powers involved in an induction heating process | 83 |
| | | |
| 4.1 | Series tank and a VFSRI | 87 |
| 4.2 | Parallel tank and a CFPRI | 87 |
| 4.3 | Voltage-fed inverter with a LCL tank | 88 |
| 4.4 | Parallel oscillating circuit | 89 |
| 4.5 | Current and resonance frequency with $P = 45$ kW | 90 |
| 4.6 | EMA TEC Multi | 90 |
| 4.7 | 3D sketch of inductor and work-piece | 91 |
| 4.8 | Example of inductor | 91 |
| 4.9 | The inductor manufactured | 92 |
| 4.10 | Explanation of Biot-Savart law application | 92 |
| 4.11 | Scheme of how calculation was carried out | 93 |
| 4.12 | $\frac{dB}{B}$ calculated inside the coil in $x - y$ plane | 93 |
| 4.13 | Ceramic tubes keep the work-piece at the centre of the inductor | 94 |
| 4.14 | Experimental setup | 97 |
| 4.15 | Thermocouples and Teflon tape insulation | 98 |
| 4.16 | Work-piece before and after sandblasting | 98 |
| 4.17 | Voltage and current probes | 98 |
| 4.18 | Voltage, current and frequency in time with 40, 30 and 20 kW | 99 |
| 4.19 | Three ampere-meters method | 101 |
| 4.20 | I_l measure | 102 |
| 4.21 | Current, voltage and instant power after 9 and 52 s ($P_{DC} = 40$ kW) | 103 |
| 4.22 | Active power and power factor of the inductor-workpiece system | 104 |

| | | |
|------|---|-----|
| 4.23 | Final temperature profile in the case of P_{DC} equal to 40, 30 and 20 kW | 106 |
| 4.24 | Work-piece between 700 and 1000 °C | 107 |
| 4.25 | Measurement – numerical result comparison | 107 |
| 4.26 | Switch (IGBT) internal design | 108 |
| 4.27 | Complete equivalent circuit | 109 |
| 4.28 | DC/AC conversion. Constant voltage is provided with a DC source | 110 |
| 4.29 | PSPICE® simulation waveform results | 111 |
| 5.1 | Inhomogeneous heating using three inductors with more complex work-piece geometry | 113 |